Doctor Thesis

学位申請論文

Observational Studies on
Energy Release Mechanism in Solar Flares

太陽フレアにおける
エネルギー解放機構の観測的研究

Ayumi Asai

浅井 歩

Kwasan and Hida observatories, Kyoto University

June, 2004

Abstract

The solar atmosphere is full of dynamic phenomena. Solar flares, which are the most energetic explosive events in the solar system, are especially attractive because of their dynamic and beautiful appearance. They also stimulate our curiosity about the generation mechanism of such explosive events. The magnetic reconnection model has been widely applied to explain solar flares and other active phenomena in recent decades. The recent remarkable progress of ground-based and space-based observations has been providing us with many new pieces of observational evidence of flares with which we have been able to examine the model in detail. However, solar flares have mainly been studied morphologically, so far, and quantitative studies of the magnetic reconnection model by using observational data are not yet sufficient. We should investigate, in more detail, both the physical properties of plasma, which are determined by relatively small scale structures in the corona, and the magnetic field configuration in solar flares which is determined by global structures. Moreover, we should examine whether the physical quantities in the two extremes are consistent with those that the magnetic reconnection model predicts.

In this thesis, we studied observational data of flares obtained in various wavelengths in detail. Since the emission mechanism is different in each wavelength, even for the same flare, we have been able to examine many aspects of flares from a combination of these data. We observed plasma motions such as plasma ejections, formation of post-flare loops, nonthermal emissions from accelerated high-energy particles, magnetic field on the photosphere, and so on. Furthermore, we examined the relationship between the magnetic field structure on macro scales and the plasma physics on micro scales. As a result, we could successfully derived information which is closely related to magnetic reconnection and the energy release mechanism, e.g. the energy release sites, timings, and the amount of released energy. Thus, we were able to test the magnetic reconnection model quantitatively. We confirmed that the changes in the estimated energy release rate are very consistent with those that are predicted by the magnetic reconnection model.

We also obtained several new observational pieces of evidence of non-steady magnetic reconnection and energy release, and therefore made an important contribution to our understanding of the flare mechanism.

This thesis consists of various topics as follows;

In **Chapter 1** we briefly review solar flares and other various active phenomena which appear on the solar surface. Moreover, we discuss the magnetic reconnection model which can explain these active phenomena, at least morphologically.

In **Chapter 2** we report a detailed examination of the fine structures inside flare ribbons and the temporal evolution of such structures. We examined systems of conjugate footpoints, inside flare ribbons by using Hα data with high spatial resolution. We first identified the conjugate footpoints of each Hα kernel, and then demonstrated that the reconnected flare loops really connect the Hα conjugate footpoints. Investigating such fine structures inside the flare ribbons in detail, we can recognize the whole of the flare as an assembly of simple systems, which consist of conjugate footpoints and a post-flare loop connecting those footpoints, even in a large and complex flare. This finding enabled us to follow the history of energy release and acquire further information which is important for the studies of particle acceleration in flares in the following Chapters.

In **Chapter 3** we present the relationship between the spatial distribution of Hα kernels and the distribution of hard X-ray (HXR) sources seen during a solar flare which occurred on 2001 April 10. We compared the spatial distribution of the HXR sources with that of the Hα kernels. While many Hα kernels are found to brighten successively during the evolution of the flare ribbons, only a few radiation sources are seen in the HXR images. We measured the photospheric magnetic field strength at each radiation source in the Hα images and found that the Hα kernels accompanied by HXR radiation have magnetic strengths about 3 times larger than those without HXR radiation. With these findings, we succeeded in quantitatively solving the puzzling problem that the spatial distribution of the HXR sources is very different from that of the Hα kernels. Furthermore, in **Chapter 4** we examined the relation between the evolution of the Hα flare ribbons and the released magnetic energy in a solar flare. Based on the magnetic reconnection model, the released energy was quantitatively calculated by using the photospheric magnetic field strengths and separation speeds of the fronts of the Hα flare ribbons. We compared the variation of the released energy with the temporal and spatial fluctuations in the nonthermal radiation observed in hard X-rays and microwaves, and found a nice correlation between them.

In **Chapter 5** we present a detailed examination of downflow motions

above flare loops observed in the 2002 July 23 flare. The extreme ultraviolet images show dark downflow motions above the post-flare loops, not only in the decay phase but also in the impulsive and main phases. We also found that the times when the downflow motions are initially seen correspond to the times when bursts of nonthermal emission in hard X-rays and microwaves are emitted. This result implies that the downflow motions occurred when strong magnetic energy was released, and that they are, or are correlated with, reconnection outflows.

In **Chapter 6** we present results of the first imaging observations of quasi-periodic pulsations (QPPs) which were observed in the 1998 November 10 flare. The hard X-ray and microwave time profiles clearly showed a QPP. We estimated the Alfvén transit time along the flare loop and found that the transit time was almost equal to the period of the QPP. We therefore suggest, based on a shock acceleration model, that variations of macroscopic magnetic structures, such as oscillations of coronal loops, affect the efficiency of particle injection/acceleration.

Contents

List of Figures

List of Tables

Chapter 1

General Introduction

In the first part of this chapter, we briefly review solar flares and related active phenomena which are observed on the solar surface in various wavelengths. Next, we also review some recent theoretical works of the magnetic reconnection model which is considered to well explain these flares and related phenomena. We describe how the present magnetic reconnection model can explain these observed phenomena at least morphologically. Finally, we specify the questions to be solved in each chapter of this thesis.

1.1 Overview

The solar atmosphere is full of dynamic phenomena. Recent solar observations with satellites such as *Yohkoh*[1], *SOHO*[2], *TRACE*[3], and *RHESSI*[4] have revealed that the solar atmosphere is much more dynamic than had been thought, even the quiet Sun is never quiet. Ground-based observations in the optical and microwave ranges have also been developed in recent decades. With the instrumental progress, our knowledge of active phenomena on the solar surface has greatly increased. This has led to a much more detailed and broader description of the active phenomena. Above all solar flares, which are the most energetic phenomena, have been studied extensively, with wide interest in their explosive and mysterious nature.

It is well known that these dynamic phenomena are caused by the release of magnetic energy. Most solar flares occur in the neighborhood of sunspots, which are called "active regions" where magnetic field strength is strong

---

[1] Ogawara et al. (1991)

[2] *Solar and Heliospheric Observatory* (Scherrer et al. 1995)

[3] *Transition Region and Coronal Explorer* (Handy et al. 1999; Schrijver et al. 1999)

[4] *Reuven Ramaty High Energy Solar Spectroscopic Imager* (Lin et al. 2002)

on the average, and the field is complex. Emergence of twisted magnetic
bundles and shear motion in the photosphere makes the coronal magnetic
field much more complex and stores magnetic energy. Once a flare occurs,
the stored huge energy is released into the solar atmosphere in a short time.
As a result of the energy release, a lot of phenomena are observed in various
wavelengths; ejections of plasma, post-flare loops, nonthermal emission from
energetic particles, and so on.

Magnetic reconnection is widely accepted as the key mechanism which
works during a flare, since it can explain various observed phenomena which
are associated with flares. However, quantitative studies of magnetic recon-
nection are not enough. We have to investigate the physical properties of the
plasma and magnetic field in solar flare regions in more detail, and examine
whether their physical quantities are compatible with the magnetic reconnec-
tion model or not. In this thesis we examined the energy release mechanism
in detail, by using a lot of observational data, and tested quantitatively the
picture of solar flares which is suggested by the magnetic reconnection model.

In this chapter we present a short review of solar flares and other active
phenomena observed on the solar surface. We describe the current view of
solar flares. Moreover, we discuss the magnetic reconnection model, which
can explain solar flares, at least morphologically. In §1.2 a brief review of solar
flares are given. In §1.3 we review the magnetic reconnection model which
we assume in this thesis and discuss the relationship between the model and
observed phenomena. In §1.4 the aim of the thesis and short introductions
on each chapter are described.

1.2   Solar Flares

Solar flares are the largest explosions in the planetary system, and a huge
amount of energy is released. Typically, it is about 10^{32} erg, which is compa-
rable to 100 million times the energy released by a hydrogen bomb. Because
of their conspicuous appearance even among the active phenomena, they
have been extensively studied since they were observed for the first time in
white light (Carrington 1859; Fig. 1.1). Flares are the response of the solar
atmosphere to a sudden, transient release of magnetic energy. The temper-
atures attained in the chromosphere are low ($\approx 10^4$ K), and in the corona
they are much higher ($\approx 10^7$ K). Flares produce transient electromagnetic
radiation over a very wide range of wavelengths extending from hard X-rays
($\lambda \approx 10^{-9}$ cm) - in very rare cases from γ-rays ($\lambda \approx 10^{-11}$ cm) - to km radio
waves (10^6 cm). Figure 1.2 shows example light curves of a flare measured
in various wavelengths.
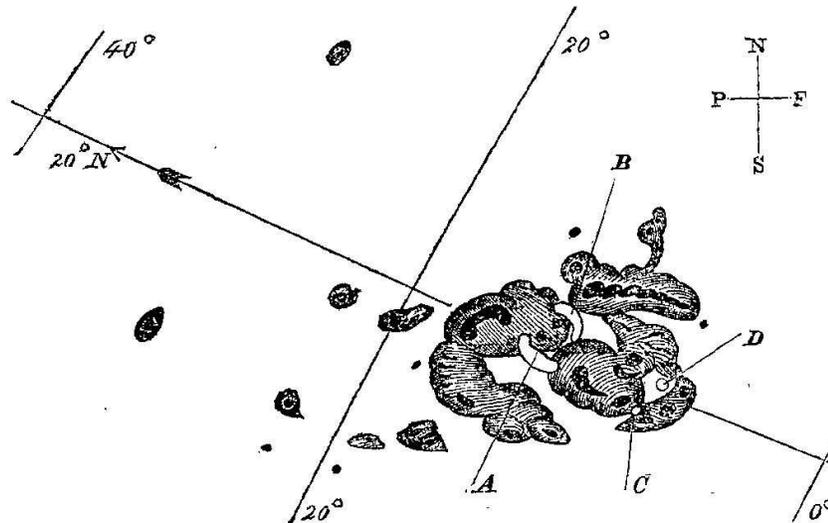
Figure 1.1: Sketch of the first reported solar flare. The flare was observed by Carrington in white light in 1859 on September 1 (Carrington 1859). White regions pointed A, B, C, and D are the flaring regions.

1.2.1 Photospheric and Chromospheric Structure

Most of the optical light which travels from the sun to the earth is emitted from the photosphere. In white light, we can see relatively quiet sun, except for some dark sunspots on it. Huge flares are sometimes observed in the white light, which are called "white light flares", but they are rare. The flare Carrington reported (Fig. 1.1) was one of the white light flares. However, with progress in spectroscopic and monochromatic image observations we have been able to examine the appearance of solar flares in the chromosphere by using chromospheric lines, such as Hα (6563 Å). Many pictures of phenomena which are often observed during flares in the photosphere and the chromosphere are shown in Bruzek & Durrant (1977).

In Hα observation, we can see brilliant flashes associated with flares. Particularly, in large-scale and long duration flares, we see a two-ribbon structure (Fig. 1.3), that is, two narrow and long bright regions (called "flare ribbons") which lie on either side of magnetic neutral line. The flare ribbons, therefore, have opposite magnetic polarities to each other. As a flare progresses, the flare ribbons separate outward with a speed of about 1 to 50 km s^{-1}. Although the two-ribbon structure becomes more ambiguous in smaller flares, flaring regions are located near magnetic neutral lines where the magnetic polarity changes.

Profile of Solar Flare
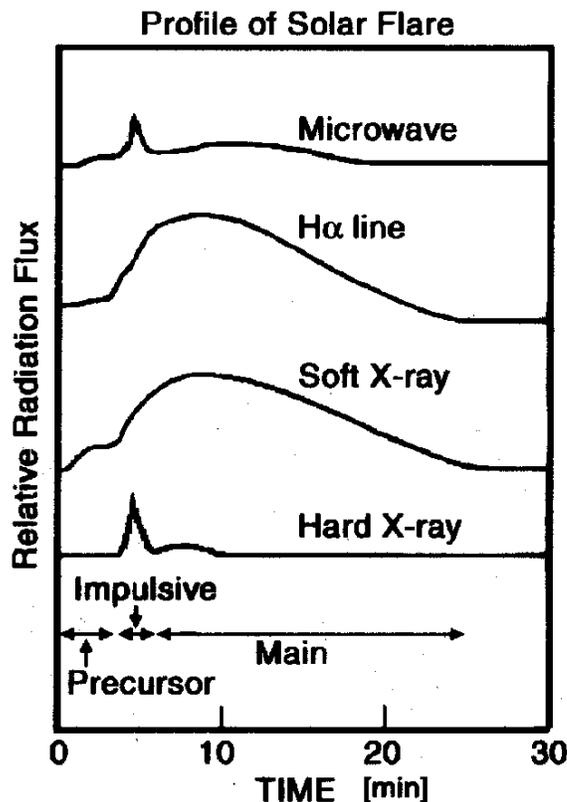
Figure 1.2: Time profiles of solar flares (based on Kane 1974).

Inside the flare ribbons we can see sub-structure which consists of small bright points, called "Hα kernels", with high spatial resolution telescopes. They brighten rapidly, although the light curve of the Hα flux integrated over the flaring region only shows a gradual change as shown in Figure 1.2. This brightening is thought to be caused by precipitation of nonthermal electrons from the corona into the chromosphere, which stimulates the excitation and ionization of hydrogen atoms (Ricchiazzi & Canfield 1983; Canfield, Gunkler, & Ricchiazzi 1984). Since the electron precipitation also produces hard X-ray (HXR) radiation via bremsstrahlung, locations and light curves of the HXR sources show high correlations with those of the Hα kernels (Kurokawa, Takakura, & Ohki 1988; Kurokawa 1989; Kitahara & Kurokawa 1990). Pneuman (1981) gave a review of two-ribbon flares.

Some filamentary structure which is dark on the disk (filament), and bright on the limb (prominence) can be seen in Hα images (Fig. 1.4). We
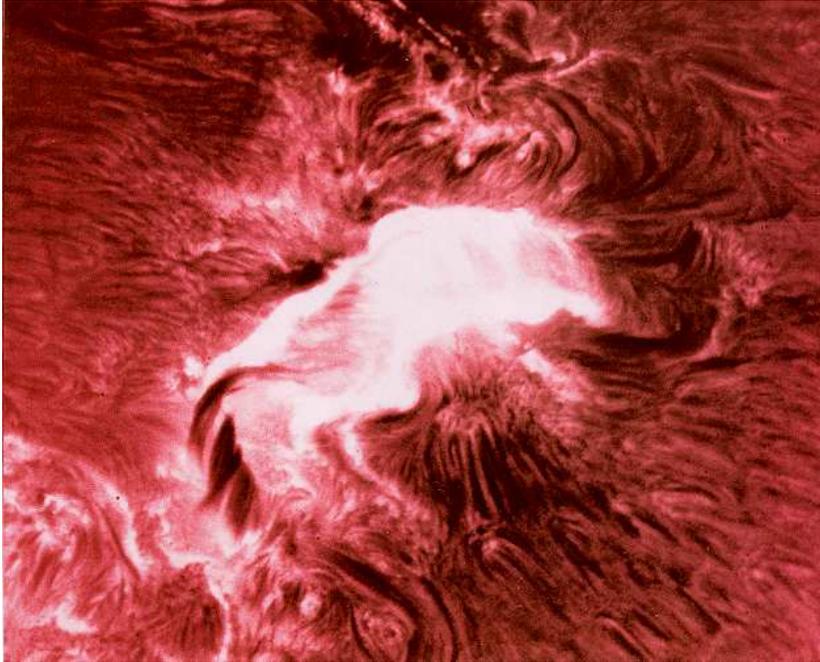
Figure 1.3: An image of a solar flare in Hα which occurred on 1984 April 25 taken with Domeless Solar Telescope at Hida Observatory (Kurokawa et al. 1987).

sometimes recognize relationships between flares and activities in filaments which lie along neutral lines in active regions. We will describe them later.

Measurements of magnetic field in the photosphere and the chromosphere also give us a great deal with important information. Magnetograms are mainly measured by using photopheric lines, and chromospheric magnetic field lines are extrapolated from the appearance in chromospheric filtergrams in which the field lines are visible due to frozen-in plasma. Magnetic energy stored in the corona is the energy sources of flares, and flares occur near magnetic-inversion regions. Therefore, precise and detailed measurement of the magnetic field evolution in flaring regions is required to examine the energy release mechanism.

Flares often occur following the emergence of new flux. This flux emergence carries magnetic energy into the corona, and the magnetic-inversion regions are generated. Shear motion on the photosphere also makes the magnetic field more complex and stores the magnetic energy in the corona. Large flares, such as X class flares, often occur at flare-generative δ-type sunspots.
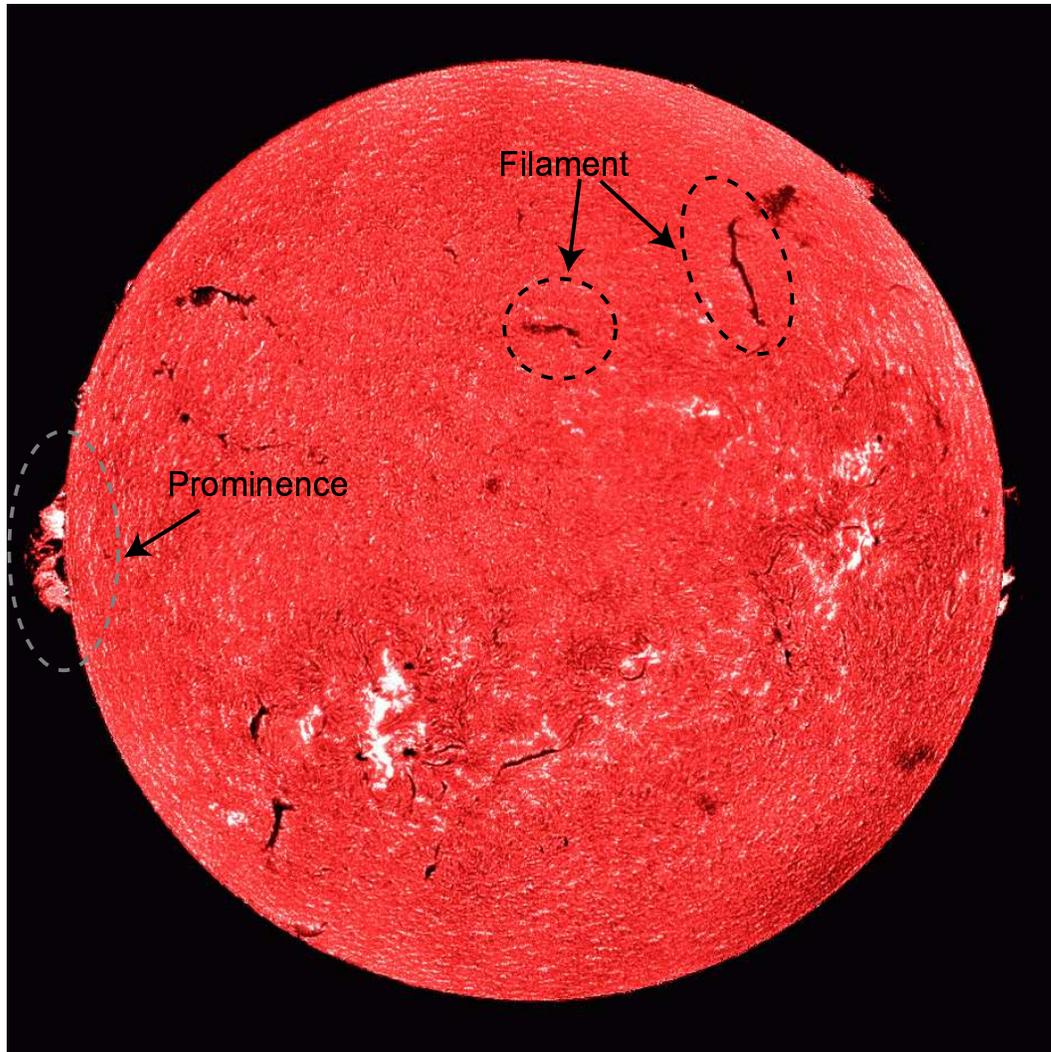
Figure 1.4: An Hα image obtained with Solar Magnetic Activity Research Telescope (SMART). Several filaments on the disk and prominences on the limb are seen.
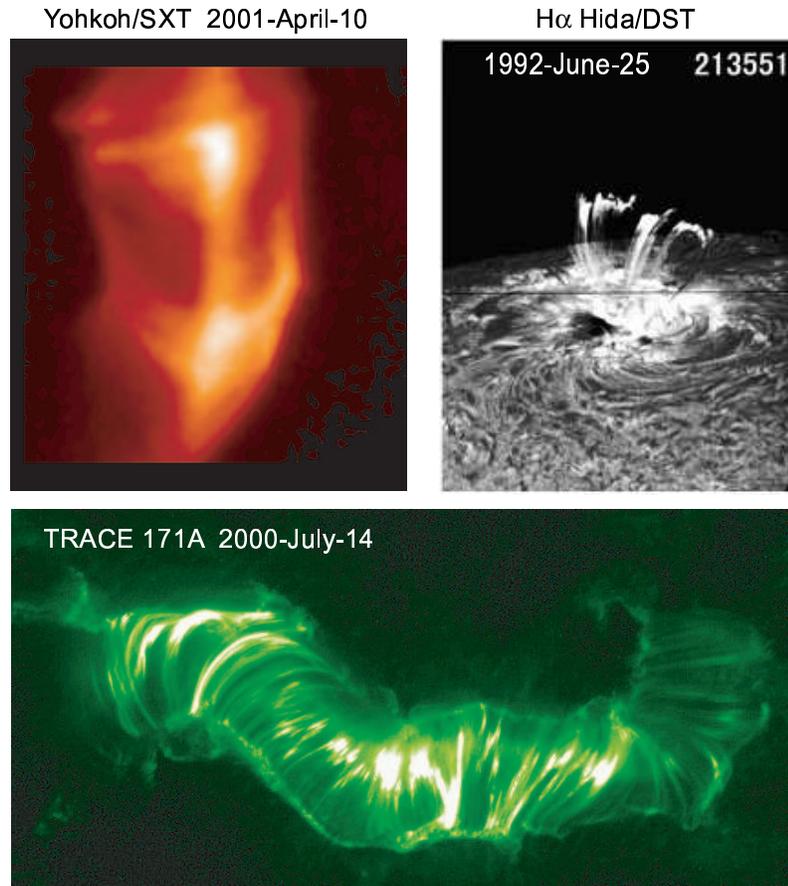
Figure 1.5: Post-flare loops seen in soft X-ray (*top left* panel), Hα (*top right* panel), and extreme ultraviolet (*bottom* panel).

Such super active regions are thought to be generated by the emergence of strongly twisted magnetic bundles (Kurokawa 1987; Ishii, Kurokawa, & Takeuchi 2000; Kurokawa, Ishii, & Wang 2002). Moreover, in some active regions, rotation of magnetic pairs together with rotation of the neutral lines is seen (Ishii et al. 2003). Therefore, where and how much energy is injected into the active region before a flare are important subjects for flare studies.

1.2.2 Coronal Structure

The solar corona is filled with low β ($= p_{gas}/p_{mag} < 1$) plasma, where magnetic force and magnetic energy dominate other types of force and energy, so that magnetic reconnection has a great influence on heating and dynamics
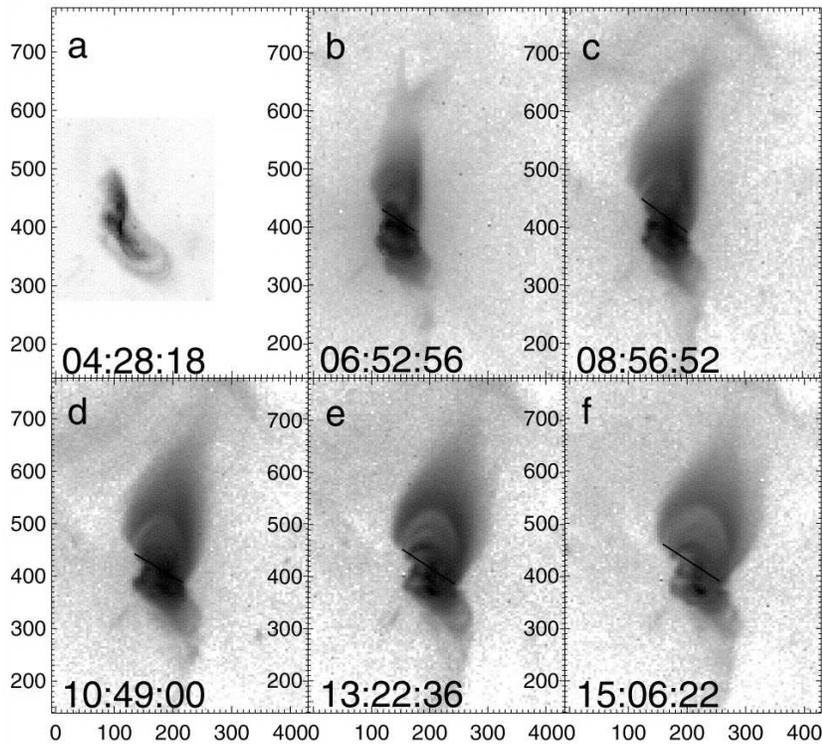
Figure 1.6: Soft X-ray images of a solar flare. Evolution of flare loops observed on 1997 May 12 with *Yohkoh*/SXT (Isobe et al. 2002).

once it happens. The phenomena which occur in the corona are much more dynamic than those in the chromosphere (average plasma $\beta \sim 1$) and the photosphere (average plasma $\beta \sim 10^4$). However, in the past it was very difficult to observe the structure of the solar corona, because the plasma is high temperature (more than 2 MK) and low density ($\sim 10^9$ cm^{-3}). The optical light from the corona is too faint to be observed on the ground except during total solar eclipses and with coronagraphs at 3,000 meters-high mountains. X-ray and extreme ultraviolet (EUV) observations, which are suitable for observing such high temperature plasma, are not easy, since they must be done by space-based instruments.

Skylab was the first X-ray satellite, and with the successful launch of *Yokhoh*, the situation was changed dramatically. *Yokhoh* revealed the dynamic features of the magnetic corona. Observations in the soft X-ray (SXR) range confirmed that flares are explosive events in the corona. The magnetic energy is released in the corona and then carried down to the chromosphere by energetic particles and thermal conduction. This makes the Hα emission

at the footpoints of the flare loops as a secondary response. The chromospheric plasma is pumped up explosively due to the pressure enhancement, which is called "chromospheric evaporation". The coronal density in the flare loops increases dramatically, because of the chromospheric evaporation, so that the flare loops become visible. Since plasma in the solar atmosphere is frozen in to the magnetic field, it has to travel along magnetic field lines. Therefore, the visible loops represent the structure of the magnetic field line.

The coronal plasma is heated up to 10 - 40 MK just after the energy release occurs, and then it cools down due to thermal conduction and radiation. It becomes visible in the EUV ($\sim$ 1 MK; the *bottom* panel in Fig. 1.5), and finally in Hα ($\sim 10^4$ K; the *top right* panel in Fig. 1.5). These loops are called post-flare loops. In the Hα range, the plasma is sufficiently cool, and therefore, we can see it draining back to the chromosphere due to the gravity force, which is called "coronal rain" because of its appearance.

Post-flare loops are well fitted with potential field lines. On the other hand, we can sometimes see twisted SXR loop structures in the pre-flare phase. Figure 1.6a shows the pre-flare stage of a flare. Such a twisted S-shape structure is called a "sigmoid". The change of the structure, from sigmoid to potential-like loops, implies that magnetic energy was released via a flare, and that the magnetic field jumped to a lower energy state.

During a flare, flare loops evolve larger and larger self-similarly as shown in Figure 1.6. Furthermore, the SXR flare often shows a cusp shaped structure (Tsuneta et al. 1992; Tsuneta 1996; Forbes & Acton 1996). As described below, this is one of the most important findings made by *Yohkoh*/SXT, since it is evidence that magnetic reconnection occurs successively at higher points.

In the microwave range, we often observe the coronal structure of flares. Especially in the impulsive phase of a flare, gyro-synchrotron emission by energetic nonthermal electrons which are accelerated during the flare are radiated in microwaves (see Fig. 1.2), and flare loops which contain these energetic electrons are lit up. We will describe the features of a flare in the microwave range again in §1.2.4 (Energetic Particle).

1.2.3 Filament/plasmoid ejections, and CMEs

We also notice some filamentary structures which are dark on the disk, and bright on the limb in Hα images. They are called dark filaments on the solar disk, and prominences on the solar limb (Fig. 1.4). They lie along magnetic neutral lines. Most of them are quiescent and do not show any drastic changes during the solar rotation, but some of them disappear or are ejected with solar flares, especially with large-scale long-duration ones. They are observed as filament/prominence eruptions (Fig. 1.7), and are

AR 8458 Hida/FMT
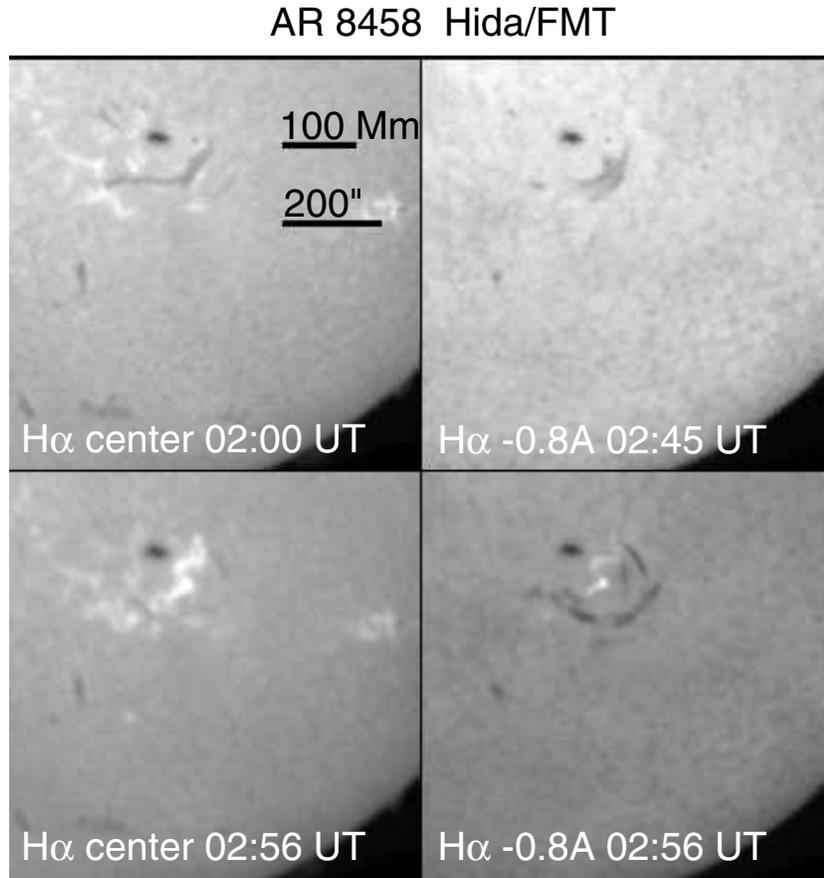
Figure 1.7: Hα images of a filament eruption, which occurred on 1999 February 16, taken with Flare Monitoring Telescope at Hida Observatory (Morimoto & Kurokawa 2003b).

associated with coronal mass ejections (CMEs; Fig. 1.9) which are released into interplanetary space.

Filaments are high-density and low-temperature plasma which are supported by the coronal magnetic field. Figure 1.7 shows a filament eruption event. Before a flare, a filament lies near a sunspot along magnetic neutral lines. As the filament erupts, it is observed clearly in the blue wing due to Doppler shift (*Right* panels of Figure), which is well known as a characteristic of filament eruption. Just after the filament is erupted, a two-ribbon flare occurred (*Left bottom* panel). On either side of the neutral line, along which the filament lies, Hα flare ribbons are located. Morimoto & Kurokawa
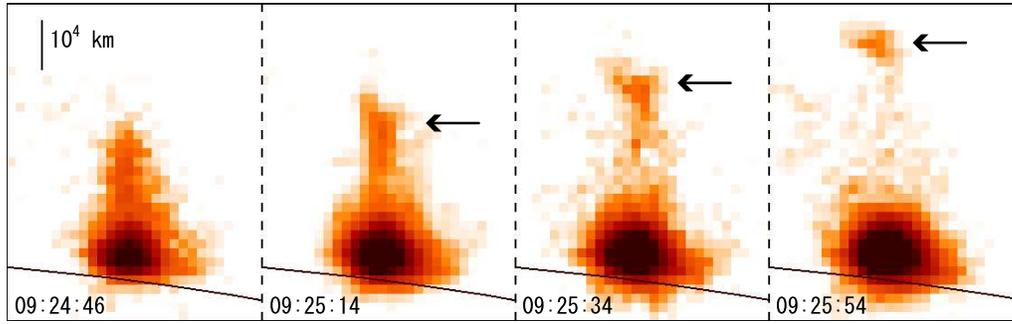
Figure 1.8: An example of plasmoid ejection taken with *Yohkoh*/SXT (Ohyama & Shibata 1998).

(2003a, 2003b) present detailed examinations of filament eruptions.

SXR plasmoid ejections are thought to be the coronal counterpart of filament eruptions. Figure 1.8 shows an example of an SXR plasmoid ejection which is associated with a flare. Since SXR plasmoids are much fainter than flare loops, they are hardly observed. Nevertheless, SXR plasmoid ejections are clearly flare-associated phenomena, and their movement strongly supports the magnetic reconnection model of flares. They are accelerated in the impulsive phase of a flare (Ohyama & Shibata 1987, 1988). Moreover, plasmoid ejections are observed even in impulsive flares, while Hα filament eruptions are often associated with large-scale long-duration flares.

Large flares are often followed by strong disturbances in interplanetary space. They are caused by mass ejections from the solar atmosphere, and called coronal mass ejections (CMEs). Figure 1.9 shows an example CME observed with *SOHO*/LASCO. They show a balloon-like shape and they expand as they rise above the solar corona. A CME releases mass of up to 10^{14} g, and the speed reaches up to 1000 km s^{-1}. During the impulsive phase of a flare they are accelerated explosively. CMEs disturb the interplanetary magnetic field. If they erupt earth-ward, the geomagnetic field is strongly affected, and geomagnetic active phenomena such as magnetic storms and aurorae are observed.

Hα filaments and X-ray plasmoids erupt into the outer atmosphere and interplanetary space with CMEs; filaments are thought to become the cores of CMEs, and filament eruptions. Almost all flares bring CMEs, but CMEs sometimes do not have any apparent activities on the solar surface.
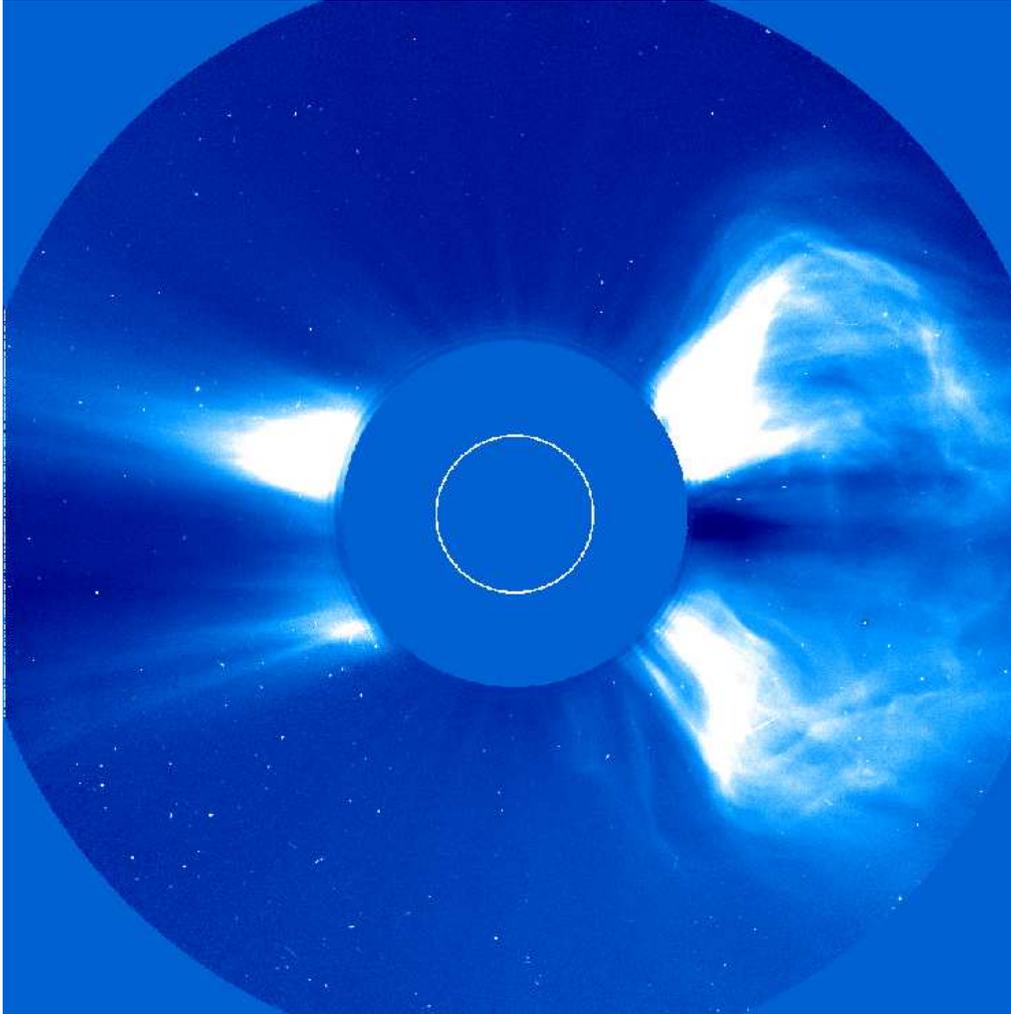
Figure 1.9: Large coronal mass ejection (CME) from 6 November 1997 as recorded by the *SOHO*/LASCO C2 coronagraph at 12:36 UT (negative image). Center black circle shows position of the sun.

1.2.4 Energetic Particle

Associated with solar flares, nonthermal emissions which are generated from accelerated high-energy particles are often observed in microwave, HXR, and γ-ray ranges. These particles are accelerated by released energy via magnetic reconnection, although the mechanisms are as yet unknown. Based on observational results, it is known that electrons and ions are accelerated up to 100 keV - 100 MeV, and up to 100 GeV, respectively.

Nonthermal emission in HXR and microwave appear when strong energy releases occur, and the sites of the radiation sources indicate where the energy is released. Neupert (1968) reported that the variation of the time integral of the microwave intensity often closely matches the variation of the SXR intensity in flares (Neupert effect). Since the SXR emission represents the total thermal energy, the Neupert effect indicates that the microwave intensity is proportional to the energy release rate. From the similarity between HXR and microwave light curves, the concept of the Neupert effect is extended to include the relationship between the SXR light curves and the HXR ones. Therefore, the HXR intensity emitted by bremsstrahlung and the nonthermal microwave synchrotron emission are thought to be correlated with the energy release rate (Hudson 1991; Wu et al. 1986; Neupert 1968). As shown in Figure 1.2, nonthermal emission, which is spiky and sometimes intermittent, appears in the initial phase of flares. This phase is called the "impulsive phase". During the impulsive phase, strong energy release occurs and energetic particles are accelerated.

Sakao (1994) reviewed in detail the features of HXR emitting sources during flares. In about half of the flares he studied, double HXR sources are observed, which are often located on both the footpoints of flare loops. Most HXR sources have accompanying Hα kernels, on the same positions. In the *left* panel of Figure 1.10 we show a map of a flare in HXR. In this flare we can see double sources and accompanying Hα kernels.

A loop-top HXR source (or "Masuda source") is one of the most surprising findings made by *Yohkoh* (Fig. 1.11). Although the intensity at the loop-top source is much weaker than that from the footpoints, the presence of the loop-top source implies that the energy release occurs at further higher sites, and therefore strongly supports the magnetic reconnection models.

The presence of nuclear reactions (when protons and α-particles are accelerated to more than about 30 MeV per nucleon) has also been confirmed by the detection of the 2.23 MeV γ-ray line. Recent space observation made by *RHESSI* allow us to synthesize γ-ray images in this line (Hurford et al. 2003).

Nonthermal emission from accelerated particles is also measured in the
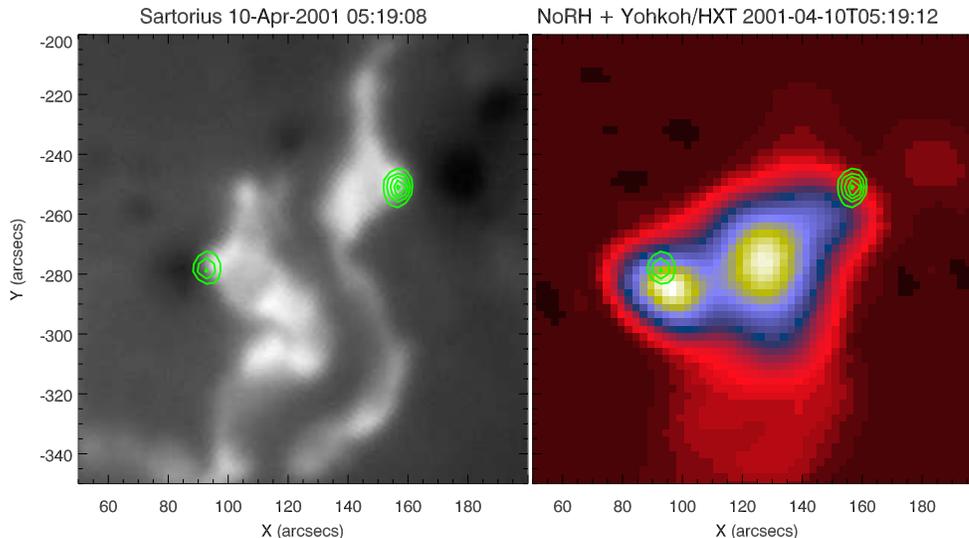
Figure 1.10: An HXR and microwave images of a flare which occurred 2001 April 10. *Left*: Hα image of the flare taken with Sartorius Telescope at Kwasan Observatory, Kyoto University. *Right*: Microwave (17 GHz) image ovserved with Nobeyama Radioheliograph. Both the images were overlaid with an HXR contour image to compare the spatial distribution of Hα kernels, HXR sources, and microwave emitting sources. Contour levels are 95%, 80%, 60%, 40%. and 20% of the peak intensity.

microwave range. The gyro-synchrotron emission from energetic electrons ($>$ several tens of keV) is often observed during the impulsive phase of a flare. Its intensity depends both on the number density of the energetic electrons and on the magnetic field strength. The *Right* panel of Figure 1.10 shows an image of a flare in the microwave range (17 GHz). We can see not only the loop source, which is emitted from electrons trapped in the flare loops, but also the footpoint sources.

The mechanism which accelerates such high energy particles that emit these nonthermal radiations is still unknown, although there are some theoretical candidates. In order to determine the particle acceleration mechanisms, both imaging and spectroscopic analyses (called "imaging spectroscopy") in these energy ranges are required.
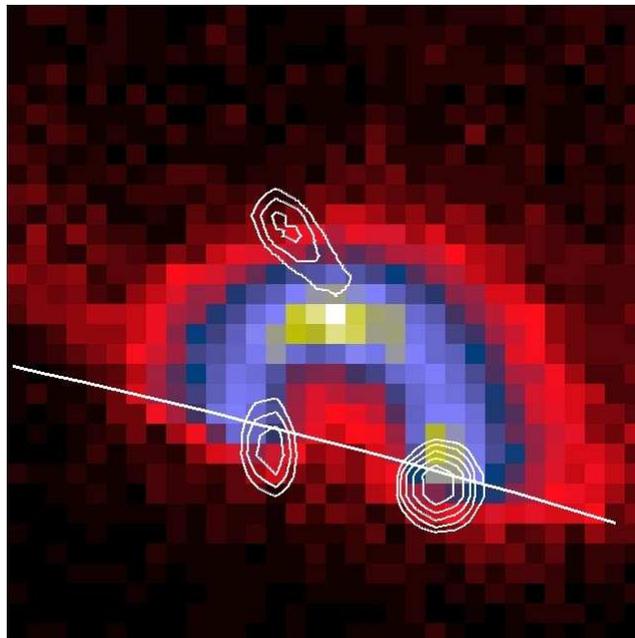
Figure 1.11: Loop top source (Masuda source) observed in the 1992 January 13 solar flare. White thick line shows the solar limb. Background color is SXR image of the flare which was taken with *Yohkoh*/SXT. Contour images was a hard X-ray image taken with *Yohkoh*/HXT (Masuda et al. 1994).

1.3 Magnetic Reconnection Model

1.3.1 Magnetic Reconnection Model of Flares

Magnetic reconnection is a physical process in which a configuration of antiparallel magnetic field lines is topologically changed. The application of magnetic reconnection to solar flares has been done by many authors, such as Sweet (1958), Parker (1957), and Petschek (1964). With magnetic reconnection we can explain the observed explosive phenomena such as solar flares (with short durations up to hours), otherwise it takes 3 million years (!) to release the stored magnetic energy by magnetic resistivity alone.

As the observations of solar flares have progressed, some scientists have tried to construct models to explain the observed phenomena, such as the Hα two-ribbon structure, post-flare loops, SXR flare loops, filament eruptions, CMEs and their influence on geomagnetic storms, and so on, based on magnetic reconnection. In particular, the magnetic reconnection model proposed by Carmichael (1964), Sturrock (1966), Hirayama (1974), and Kopp & Pneu-
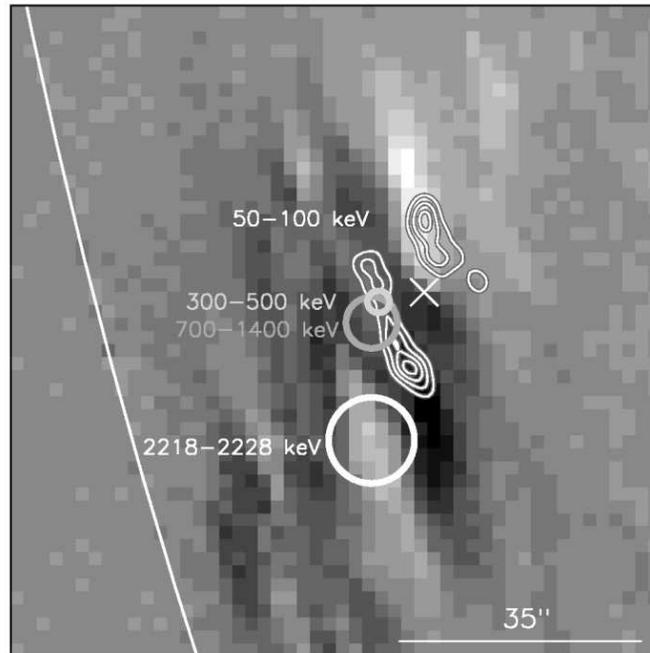
Figure 1.12: A γ-ray image of a flare which occurred 2002 July 23. The thick circles represent the 1σ errors for the 300 - 500 keV (*light gray*), 700 - 1400 keV (*dark gray*), and 2218 - 2228 keV (*white*) maps. The $35''$ FWHM angular resolution is shown in the lower right. The thin *white* contours show the detailed images at 50 - 100 keV map. The white contours show the high-resolution 50 - 100 keV map with $3''$ resolution. The cross shows the centroid of the 50 - 100 keV emission. The background image is a SOHO/MDI magnetogram acquired at 00:12 UT, 15 minutes prior to the flare.

man (1976) (CSHKP model) has been accepted by many solar physicists as a standard one. Švestka and Cliver (1992) and Sturrock (1992) presented a good historical review of the magnetic reconnection model. The CSHKP model suggests that magnetic field lines, at greater and greater heights, successively reconnect in the corona, and can explain such well-known features of solar flares as the growth of flare loops (Fig. 1.6) and the formation of the Hα two-ribbon structures at their footpoints (Fig. 1.3). In Figure 1.13, we present a cartoon of the model. The Hα flare ribbons are caused by the precipitation of nonthermal particles and the effect of thermal conduction. As the magnetic field lines reconnect, the reconnection points (X-points) move upward. As a result, the newly reconnected field lines have their footpoints further out than those of the field lines that have reconnected earlier. There-
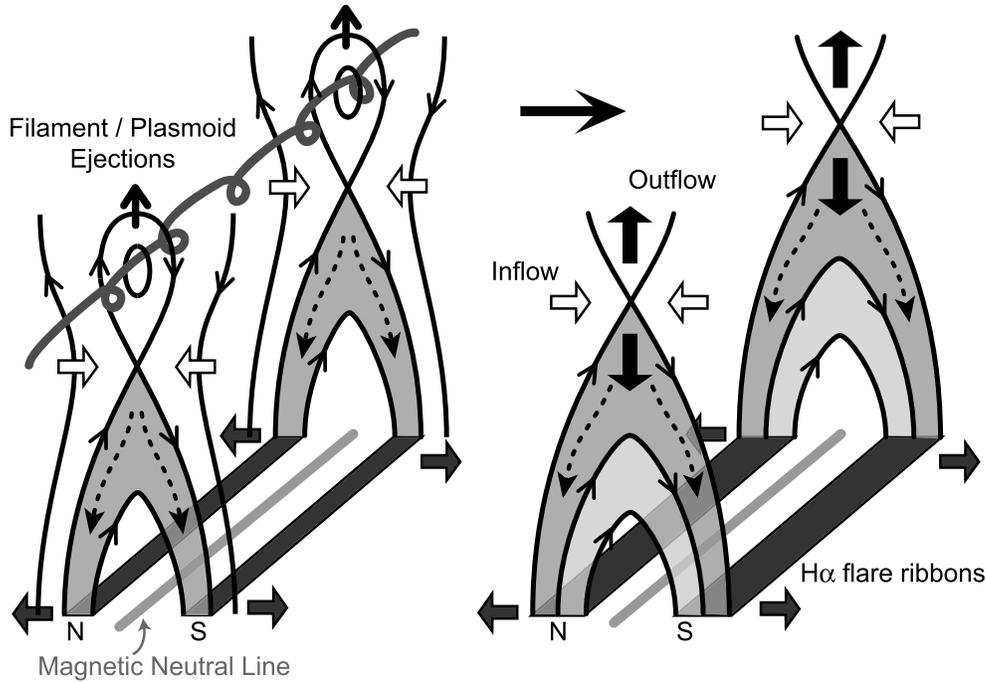
Figure 1.13: Cartoon of magnetic reconnection. Solid lines show the magnetic field lines. N and S show the magnetic polarities. Reconnected magnetic field lines form post-flare loops with a cusp shaped structure (gray regions). Along the reconnected loops, nonthermal particles and thermal conduction propagate from the reconnection site to the footpoints (dashed arrows). As they precipitate into the chromosphere the Hα flare ribbons are generated at the footpoints (dark gray region). They are located on either side of the magnetic neutral line (light gray line), and have opposite magnetic polarities to each other.

fore, the separation of the flare ribbons is not a real motion of the plasma, but an apparent shift of the heated footpoints. The observed temperature structure also supports the model. The outer loops are filled with high temperature plasma which is seen in soft X-rays, and the inner loops are filled with lower temperature plasma and are seen as post-flare loops in the EUV and Hα (Fig. 1.5). A good review of the relationship between magnetic reconnection and the Hα two-ribbon structures is presented in Pneuman (1981).

Recent satellite observations with high temporal and spatial resolutions such as *Yohkoh*, *SOHO*, and *TRACE* have revealed various pieces of observational evidence of magnetic reconnection in solar flares such as cusp shaped
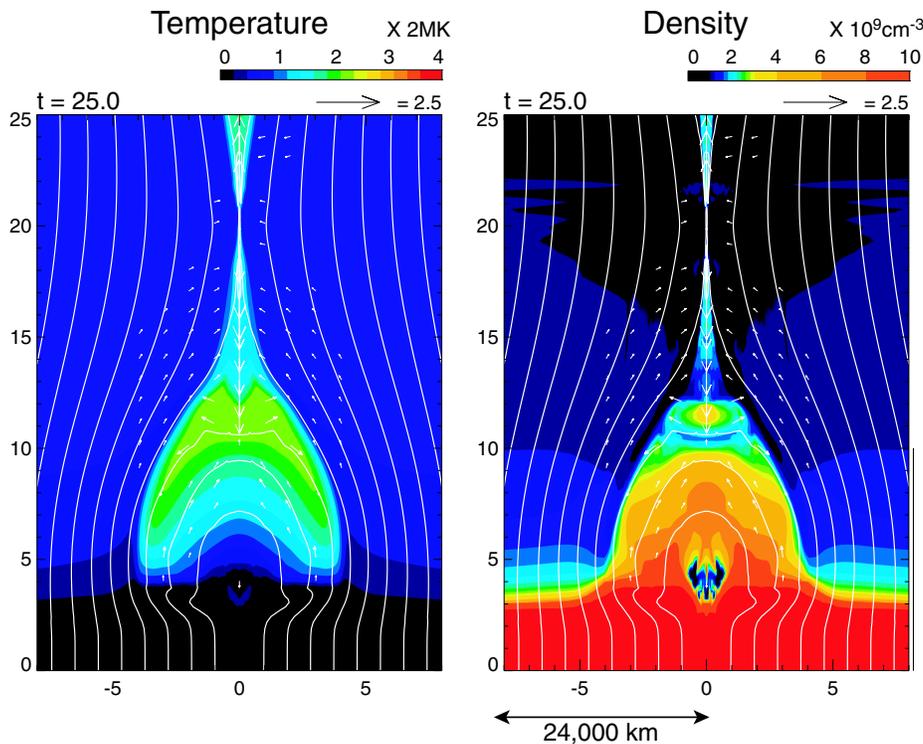
Figure 1.14: Results of a numerical simulation of magnetic reconnection. Left and right: Temperature and density distribution, respectively. The arrows show the velocity, and lines show the magnetic field lines. The units of length, velocity, time, temperature, and density are 3000 km, 170 km s^{-1}, 18 s, 2 $\times$ 10^6 K, and 10^9 cm^{-3}, respectively (Yokoyama & Shibata 2001).

structures (Fig. 1.6; Tsuneta et al. 1992; Tsuneta 1996; Forbes & Acton 1996), plasmoid ejections (Fig. 1.8; Ohyama & Shibata 1997; 1998), loop-top HXR sources (Fig. 1.11; Masuda et al. 1994), downflow motions (McKenzie & Hudson 1999, McKenzie 2000), and reconnection inflows (Yokoyama et al. 2001). Based on these discoveries, the magnetic reconnection models have been further extended by e.g. Priest & Forbes (1990; 2000), Moore & Roumeliotis (1992), Moore et al.(2001), Shibata (1995, 1999), and Yokoyama & Shibata (2001). In Figure 1.14 and 1.15 we show the result of a numerical simulation of magnetic reconnection. In this simulation many observational phenomena such as the cusp-shaped structure, chromospheric evaporation flare-ribbon expansion, are successfully reconstructed not only morphologically but also physically. Aschwanden (2002) also gives a good review of the recent magnetic reconnection models of solar flares.
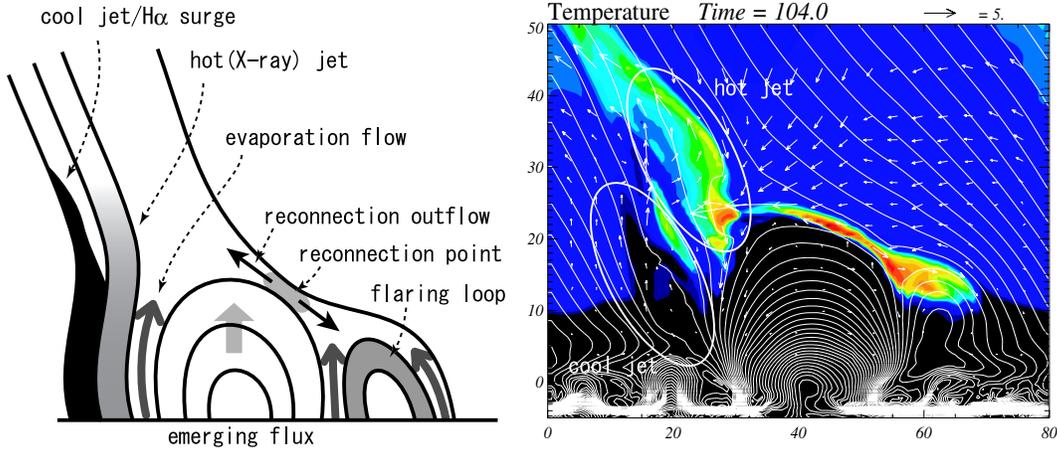
Figure 1.15: Cartoon and simulation result of Hα surge and X-ray jet. (a). Cartoon of the situation. (b). Simulation result about interaction between EFR and ambient field, which generates Hα surges and X-ray jet (Yokoyama & Shibata 1996).

We can now say that the magnetic reconnection mechanism of solar flares is established, at least, phenomenologically. However, there still remain a number of problems or puzzles both observationally and theoretically, and much more quantitative analyses of solar flares must be made to establish or reject this modern model. Therefore, we are required to quantitatively test the magnetic reconnection model, based on various observed phenomena, such as, reconnection inflow, downflow and plasmoid ejection (reconnection outflow), evolution of Hα flare ribbon, spatial distribution of radiation sources, and so on.

In addition, it is also important to study processes of magnetic reconnection in solar flares as the following reason; as we already mentioned, magnetic reconnection is just a physical process which often occurs in magnetized plasma. To solve the magnetic reconnection process probably leads us to understand many active phenomena observed in the space. We will discuss this more in the next section. Therefore, magnetic reconnection is intensively studied not only from magnetic reconnection in solar flares, but also from many aspects such as magnetospheric reconnection, laboratory experiments of magnetic reconnection, and so on. Some fundamental questions and puzzles yet to be solved in flare physics are: (1) What is the energy build-up process and the triggering mechanism of reconnection in solar flares? (2) How can we connect the macro-scale MHD and small-scale plasma processes?

What is the role of plasmoid ejections and non-steadiness in fast reconnection? (3) How are these nonthermal particles accelerated in association with magnetic reconnection? In solar physics, we mainly study the morphological structure by using 2D images of flares. If we can derive quantitative informations about the magnetic reconnection and the energy release mechanism from those data, it brings us a further great progress in solving the magnetic reconnection process. With such a motivation, in this thesis we present new observational evidence of magnetic reconnection and quantitative information about energy release in solar flares. In order to provide critical parameters necessary for the solution of the questions mentioned above, we perform quantitative analyses of the magnetic reconnection model. To do that, in the following chapters, we derive information about energy release during solar flares from observational data, and then compare the results with those the magnetic reconnection model suggests.

Figure 1.16: Examples of jet-like features on the solar surface. (a). Hα surge taken with DST at Hida Observatory. (b). X-ray jet taken with *Yohkoh*/SXT. (Shibata et al. 1994; Shimojo et al. 1996)

1.3.2   Application to Other Active Phenomena

There are many other active phenomena on the solar surface. Most of them relate to magnetic reconnection directly or indirectly. Here, we briefly introduce some phenomena which are considered to be produced by magnetic reconnection.

Solar Jets

On the solar surface, we can see a lot of jet-like structures, which are narrow and elongated, e.g., Hα surges (Fig. 1.16a) in Hα line, and SXR jet (Fig. 1.16b) in SXRs.

Many studies of Hα surges have been made for a long time (e.g., Roy 1973). Hα surges show the ejection of plasma whose temperature is $\sim 10^4$ K and are considered to be caused by magnetic reconnection in the chromosphere. The plasma motion in such a low temperature range is magnetically driven. On the other hand, the studies of X-ray jets have been promoted with *Yohkoh*/SXT and analyzed in detail by Shimojo et al. (1996). The average temperature is much higher, $\sim 5 \times 10^6$ K, and they are thought to

be caused by magnetic reconnection in the solar corona. They are pressure driven. The collimated structure indicates confinement by the surrounding magnetic field.

What kind of circumstance leads to such jet-like eruptions? Some scientists have paid attention to emerging flux regions (EFRs). Kurokawa (1988) and Kurokawa & Kawai (1993) have reported that Hα surges are often found at the earliest stage of emerging flux regions. X-ray jets are often found in EFRs, too (Shibata et al. 1992; Shimojo et al. 1996). Magnetic reconnection between newly emerging flux and the pre-existing magnetic field is the essential mechanism of production of Hα surges and X-ray jets (Kurokawa & Sano 2000), though the size of such EFR-associated surges is smaller than that of typical flare-associated surges. Moreover, Yokoyama & Shibata (1995, 1996) and Miyagoshi & Yokoyama (2003) showed in their numerical simulations that reconnection really produces Hα surges in EFRs. Figure 1.15 shows the result of these numerical simulations and a cartoon.

Nanoflare and Coronal Heating

The mechanism of solar coronal heating is one of the long-standing questions in astrophysics and is not yet solved. Recent new observations suggest the possibility that even the quiet corona may be heated by small scale reconnection events such as microflares, nanoflares, or picoflares (e.g. Parker 1991, Axford et al. 1999).

Shimizu et al. (1995) analyzed active region transient brightenings (ARTBs) in detail, and found that their energy corresponds to that of microflares. The total thermal energy content of ARTBs is 10^{25} - 10^{29} ergs, their lifetime ranges from 1 to 10 min, their length is $(0.5 - 4) \times 10^4$ km, and the temperature is about 6 - 8 MK. Recent observations in optical light showed that they occur in association with the emergence of tiny magnetic bipoles, suggesting reconnection between emerging flux and the pre-existing field. Shimizu et al. (1995) also showed that the occurrence frequency of microflares shows a power-law distribution; $dN/dE \propto E^{-\alpha}$, where dN is the number of events per day in the energy range between $E + dE$ and E, and $\alpha \sim 1.5$ - 1.6. This is nearly the same as that of larger flares. Since the index α is less than 2, the microflare distribution seems to suggest a universal physical origin for both microflares and large scale flares.

As application of SXR ARTBs to smaller energy ranges, Krucker & Bentz (1998) analyzed active region brightenings in the EUV and found that the spectral index α is about 2.3 - 2.6 in this case, which shows a possibility that such smaller flares may occur and can heat the corona. Moreover, Katsukawa & Tsuneta (2001) analyzed small fluctuations of SXR intensity, and also

suggested the possibility of coronal heating by picoflares.

Space Plasma

All active phenomena occurring in the solar atmosphere seem to be related to magnetic reconnection, directly or indirectly. This is probably a consequence of the universal properties of magnetized plasmas: the solar corona is low β $(= p_{gas}/p_{mag} < 1)$ plasma, where magnetic force and magnetic energy dominate other types of force and energy, so that magnetic reconnection has a great influence on heating and dynamics once it happens. This is also a result of the properties of magnetized plasma (e.g., Tajima & Shibata 1997): Magnetic fields tend to be concentrated in thin filaments in high β plasmas, so that the magnetic energy density in these filaments is much larger than the average value. Hence, once reconnection occurs in these filaments, the influence of reconnection is not small.

Therefore, the studies of active phenomena on the solar surface such as flares, solar jets, and so on, are essential and important for studying astrophysical plasma. We can see a lot of common features in astrophysical phenomena such as stellar flares, proto-stellar flares, proto-stellar jet, galactic jet, AGN[5] jets, γ-ray bursts, and so on. The solar events may be prototypes of such astrophysical phenomena. We can also apply the physics of solar phenomena to that of geomagnetic activities. Magnetic reconnection is essential for understanding them. Therefore, in order to solve the mechanism of such astrophysical and geophysical phenomena, it is important to investigate the magnetic reconnection mechanism in solar flares in details. This may enable us to understand more about universal space plasma.

---

[5]active galactic nuclei

1.4   Aim of This Thesis

As we have mentioned so far, current situation of the studies about magnetic reconnection in solar flares are summarized as follows;

(1) Many phenomena are observed, associated with solar flares, such as the Hα two-ribbon structure, post-flare loops, SXR flare loops, filament eruptions, CMEs, cusp shaped structures, plasmoid ejections, loop-top HXR sources, downflow motions, reconnection inflows, and so on. The magnetic reconnection is widely discussed to explain those active phenomena, at least, phenomenologically. (2) Magnetic reconnection is one of basic physical processes which often occur in magnetized plasma, and to study the processes in solar flares plays an important role in understanding various kinds of active phenomena observed in the space and cosmic plasma. (3) However, studies about magnetic reconnection in solar flares have been mainly done by the morphological ways, and the quantitative approaches have not yet been sufficient.

In this thesis we quantitatively study the evolutionary changes of three dimensional structures of solar flares, and aim to understand the energy release mechanisms of them, examining the magnetic reconnection model. We present a detailed examination of various active phenomena which are associated with solar flares by using a variety of observational data obtained in multiple wavelengths, and discuss the relationship between these phenomena and magnetic field structures. We derive information about the mechanism of energy release which occurs during flares. Then, we examine quantitatively the current unified picture of solar flares based on the magnetic reconnection mechanism in details. Here, we enumerate the topic and questions to be discussed in each chapter below;

Question 1 : Can conjugate system be identified in a huge complex flare?

Firstly, we examine chromospheric sites of direct bombardment of nonthermal particles by using Hα images, and then, discuss a **conjugate system**, an essential unit of a flare, by examining the light curves of each Hα kernels (**Chapter 2**). HXR emissions mark the chromospheric sites of direct bombardment of nonthermal particles. Hα observations, although numerous and frequently reported, have been thought to be difficult to use in a quantitative way for particle kinematics, because its complicated physics involving radiative transfer is less understood. However, Hα kernels often show good spatial and temporal correlation with HXR fluxes, suggesting that both signatures are excited by the same precipitating electrons (Canfield et al. 1984;

Canfield & Gayley 1987; Kurokawa, et al. 1988; Kurokawa 1989; Kitahara & Kurokawa 1990). If Hα emission is produced by the same precipitating electrons as HXR one, we expect to see the sites of them with higher spatial resolution by using Hα data.

A solar flare is an assembly of simple units, each of which consists of two footpoints and a flare loop connecting them, even if it is a huge and complexed flare. By resolving a flare into such conjugate systems, and by examining their temporal evolution, we can follow the essential process of flare development, in which the simple units are successively formed by energy releases and particle accelerations owing to successive magnetic reconnection. So far, evolution of solar flares has been mainly discussed to explain the evolution of a whole structure, such as separation of Hα two ribbons and formation of post-flare loops. Furthermore, no previous observation has ever succeeded in determining precisely conjugate footpoints, since it has been difficult to judge whether highly correlated pairs of footpoints are really connected by flare loops. Although Kurokawa et al. (1992) examined coincidences of spatial configurations of Hα bright kernels with flare loops using SXR images obtained with *Yohkoh*/SXT, they could not confirm coincidences because of the insufficient spatial resolution of SXT. Now, however, coronal images with high spatial resolution in extreme-ultraviolet (EUV) images obtained with the *Transition Region and Coronal Explorer* (*TRACE*) are available. Therefore, we can check whether a loop really connects Hα conjugate footpoints.

In Chapter 2 we present a detailed examination of the temporal evolutions of fine structures inside Hα flare ribbons during an X2.3 solar flare, which occurred on 2001 April 10. We examine systems of conjugate footpoints, inside flare ribbons, by using Hα images obtained with the Sartorius telescope at Kwasan Observatory, Kyoto University. Then, We identify Hα conjugate footpoints in both flare ribbons by a new method that uses cross-correlation functions of the light curves. We also compare the sites of the Hα kernels with *TRACE*, and examine whether Hα kernels are really connected by flare loops seen in the *TRACE* 171 Å images.

Question 2 : Can we estimate energy release rate quantitatively which explain observed variations of emission sources?

In the next two chapters we examine the energy release mechanism during a solar flare, and evaluate the **amount of released energy** by using observable physical parameters (**Chapter 3, 4**). Hα kernels and HXR sources observed in the impulsive phase of a flare show a high correlation in their

locations and light curves (Kurokawa, et al. 1988; Kurokawa 1989; Kitahara & Kurokawa 1990), while the difference between the spatial distributions of Hα kernels and HXR sources is also well known: Hα images sometimes show elongated brightenings, called Hα flare ribbons, with many Hα kernels within them. On the other hand, HXR images show very few sources, sometimes only one. HXR sources are accompanied by Hα kernels in many cases, but many Hα kernels are not accompanied by HXR sources. The only exception is the Bastille Day event on 2000 July 14 (Masuda, Kosugi, & Hudson 2001), which shows a two-ribbon structure even in HXRs. The lack of radiation sources in HXRs may be explained by the difference in radiation mechanisms between HXRs and Hα. The HXR intensity is proportional to the number of accelerated electrons and is thought to be proportional to the energy release rate (Hudson 1991; Wu et al. 1986). Therefore, only compact regions where the largest energy release occurred are observable as HXR sources. On the other hand, the mechanisms for Hα radiation are much more complicated than those for HXR radiation, and to derive the effect of electrons is quite difficult (Ricchiazzi & Canfield 1983; Canfield, et al.1984). Some weaker Hα kernels may be caused by other effects, such as thermal conduction. Nevertheless, since the light curve of each Hα kernel has a high correlation with that of the HXR intensity as we mentioned above, we suggest that the difference between the spatial distributions of Hα kernels and HXR sources is caused by the low dynamic range of the HXR data. In the HXR images, only the strongest sources are seen, and the weaker sources are buried in the noise.

We present a study of the relationship between the spatial distribution of Hα kernels and that of HXR sources seen during the 2001 April 10 solar flare. We compared the spatial distribution of the HXR sources with that of the Hα kernels. While many Hα kernels are found to brighten successively during the evolution of the flare ribbons, only a few radiation sources are seen in the HXR images. We use the HXR data taken with *Yohkoh*/HXT, and the dynamic range of the HXT images is about 10. Therefore, if the released energy at the Hα kernels associated *with* HXR sources is at least 10 times larger than that at the Hα kernels *without* HXR sources, then the difference of appearance can be explained. We measure the photospheric magnetic field strengths at each radiation source in the Hα images and found that the Hα kernels accompanied by HXR radiation have magnetic strengths about 3 times larger than those without HXR radiation. We also estimate the energy release rates based on the magnetic reconnection model by using the photospheric magnetic field strengths alone in Chapter 3. Next, we examine the relationship between the evolution of the Hα flare ribbons and the released magnetic energy in the solar flare. Based on the magnetic recon-

nection model, the released energy is quantitatively calculated by using the photospheric magnetic field strengths and separation speeds of the fronts of the Hα flare ribbons in Chapter 4. We compare the variation of the released energy with the temporal and spatial fluctuations in the nonthermal radiation observed in HXRs and microwaves. We also reconstruct the peaks in the nonthermal emission by using the estimated energy release rates. With these analyses, we, for the first time, quantitatively show that the current magnetic reconnection model can precisely reproduce the temporal and spatial variations of flare emissions.

Next, we present the results of the examinations on other flare-associated phenomena. They show evidence of non-steady dynamical magnetic reconnection and associated energy release which occurs in solar flares.

Question 3 : What is a characteristic of reconnection outflows?

Observational studies on reconnection inflow/outflow are very important, since they have direct information about magnetic reconnection. As we already mentioned above, **downflow** has been paid attention as a new candidate of a reconnection outflow from the first observation report done by *Yohkoh*/SXT (McKenzie & Hudson 1999, 2001). Although these values contain considerable uncertainties, they suggested that they are "moving voids" which consist of such low-density and high-temperature plasma. These voids are pushed downward because of magnetic reconnection which occurred at higher altitudes, and therefore, they are thought to be new observational and morphological evidence of magnetic reconnection. Moreover, Gallagher et al. (2002) and Innes, McKenzie, and Wang (2003a,b) reported similar downflows in EUV images obtained with the *TRACE*. By using the *TRACE* images, we have been able to examine downflows with higher spatial resolution than was done with *Yohkoh*/SXT. Furthermore, Innes et al. (2003a) performed spectroscopic analyses with the data obtained with the Solar Ultraviolet Measurements of Emitted Radiation (SUMER) instrument (Wilhelm et al. 1995) aboard *SOHO*. The results discard the possibility that the downflows are cold absorbing material, and support a model in which the downflows are moving voids. However, there are many unsolved questions, even including what they are. So far, almost all the downflows have been observed in long duration event (LDE) flares, and many of them (about 70% of all) were observed after the peak times of SXR light curves (McKenzie & Hudson 2001; Hudson & McKenzie 2001. In these events, therefore, HXR enhancements are not so strong to be compared with downflows. If downflows are really related to magnetic reconnection, they are expected to be observed

even in the impulsive phase, when magnetic reconnection occurs vigorously, and when nonthermal emissions are observed in HXRs and in microwaves.

On the other hand, we observed the *TRACE* downflows and the impulsive HXR and microwave bursts, simultaneously. In **Chapter 5** we present a detailed examination of downflow motions above flare loops observed in the 2002 July 23 flare. Then, we discuss a characteristic of the downflows as downward reconnection outflows. The extreme ultraviolet images obtained with the *TRACE* show dark downflow motions (sunward motions) above the post-flare loops, not only in the decay phase but also in the impulsive and main phases. We also demonstrate that the times when the downflow motions start to be seen correspond to the times when bursts of nonthermal emissions in HXRs and microwave are emitted. Furthermore, we discuss one of an important characteristic of downflows that they appear intermittently, and are associated with impulsive nonthermal emissions.

Question 4 : How does a global flare structure affect periodic particle acceleration?

We report a result on periodic features of nonthermal emissions associated with solar flares. To solve the particle acceleration mechanism is one of the most difficult and unsolved problems, both in the astrophysics and in the plasma physics, and has been intensively challenged theoretically and observationally. Nonthermal particles are accelerated associated with energy release processes, such as magnetic reconnection, and therefore, they have information about energy release mechanisms in solar flares. Periodic features of nonthermal emissions are sometimes observed, and have been studied so far. A good example of such **quasi-periodic pulsations** (**QPPs**) in HXR and microwave was seen in a flare on 1980 June 7 (Kiplinger et al. 1983; Nakajima et al. 1983; Kane et al. 1983). Tajima, Brunel, & Sakai (1982) and Tajima et al. (1987) showed by their numerical simulation that the current loop coalescence instability induces the QPPs, and that the period of the QPP is equal to the Alfvén transit time across the current loop. However, that situations have never diagnosed by using 2-dimensional images of flares, and the relationship between the QPP and the magnetic loop structure is still unclear.

In **Chapter 6** we present an examination of multi-wavelength observations of a C7.9 flare that occurred on 1998 November 10. We found bursty and intermittent particle acceleration which is modulated due to the dynamical changes in the global magnetic field. Since this is the first imaging observation of QPPs, we could examine the flare by using the information of

spatially resolved physical parameters, such as, temperature, emission measure, magnetic field strength, and so on. We examine the relationship between the QPP and the global structure of the magnetic field in the flare. We estimate the Alfvén transit time along the flare loop by using the images of *Yohkoh*/SXT and photospheric magnetograms, and examine the relation between the transit time and the period of the QPP. We discuss, based on a shock acceleration model, that variations of macroscopic magnetic structures, such as oscillations of coronal loops, affect the efficiency of particle injection/acceleration.

Finally, we summarize this thesis and present future prospects in **Chapter 7**.

We attached a summary of the instrumentation in **Appendix A**. In this thesis we used a lot of observation data, which were obtained in various wavelengths both with ground-based and space-based instruments. By examining the appearance of active regions and flares in the photosphere, the chromosphere, and the corona, which are observed with these instruments, we derived information on energy release during flares. In this appendix we summarize the instruments and the data, which we mainly used in the thesis, and/or which are related to our studies. Furthermore, we introduce characteristics of each of the instruments.

This thesis is based on five published papers, which were collaboration works by myself (AA) and coauthors. In each of them, main parts of the work (motivation, data analyses, and discussions) were performed by AA. We used multiple observational data of solar flares in each paper. Hα images were obtained with Sartorius Telescope at Kwasan Observatory, Kyoto University. Data in EUVs, SXRs, HXRs, and magnetogram were obtained by satellites, *Yohkoh*, *SOHO*, *TRACE*, and *RHESSI*.

Bibliography

Aschwanden, M. J. 2002, Space Science Reviews, 101, p. 1

Axford, W. I., McKenzie, J. F., Sukhorukova, G. V., Banaszkiewicz, M., Czechowski, A., Ratkiewicz, R. 1999, Space Science Reviews, 87, 25

Bruzek, A. & Durrant, C. J. 1977, Astrophysics and Space Science Library, 69, Illustrated Glossary for Solar and Solar-Terrestrial Physics, (Dordrecht: Reidel)

Canfield, R. C., Gunkler, T. A., and Ricchiazzi, P. J. 1984, ApJ, 282, 296

Ganfield, R. C. & Gayley, K. G. 1987, ApJ, 322, 999

Carmichael, H. 1964, in The Physics of Solar Flares, ed. W. N. Hess (NASA SP-50), 450

Carrington, R. C. 1859, MNRAS, 20, 13

Forbes, T. G. & Acton, L. W. 1996, ApJ, 459, 330

Gallagher, P. T., Dennis, B. R., Krucker, S., Schwartz, R. A., Tolbert, A. K. 2002, Sol. Phys., 210, 341

Handy, B. N., et al. 1999, Sol. Phys., 187, 229

Hirayama, T. 1974, Sol. Phys., 34, 323

Hudson, H. S. 1991, Sol. Phys., 133, 357

Hudson, H. S. & McKenzie, D.E. 2001, Earth Planets Space, 53, 581

Hurford, G. J., Schwartz, R. A., Krucker, S., Lin, R. P., Smith, D. M., Vilmer, N. 2003, ApJ, 595, L77

Innes, D. E., McKenzie, D. E., Wang, T. 2003a, Sol. Phys., 217, 247

Innes, D. E., McKenzie, D. E., Wang, T. 2003b, Sol. Phys., 217, 267

Ishii, T. T., Kurokawa, H., Takeuchi, T. T. 2000, PASJ, 52, 337

Ishii, T. T., Asai, A., Kurokawa, H., Takeuchi, T. T. 2003, in 25th meeting of the IAU, in press

Isobe, H., Yokoyama, T., Shimojo, M., Morimoto, T., Kozu, H., Eto, S., Narukage, N., Shibata, K. 2002, ApJ, 566, 528

Kane, S. R. 1974, Impulsive (flash) phase of solar flares: hard X-ray, microwave, EUV, and optical observations, in *Coronal disturbances* (ed. G. Newkirk), Proc. 54th IAU Symp., Reidel, Dordrecht, p. 105

Kane, S. R., Kai, K., Kosugi, T., Enome, S., and Landecker, P. B., & McKenzie, D. L. 1983, ApJ, 271, 376

Katsukawa, Y. & Tsuneta, S. 2001, ApJ, 557, 343

Kiplinger, A. L., Dennis, B. R., Frost, K. J., & Orwig, L. E. 1983, ApJ, 273, 783

Kitahara, T. & Kurokawa, H. 1990, Sol. Phys., 125, 321

Kopp, R. A. & Pneuman, G. W. 1976, Sol. Phys., 50, 85

Kurokawa, H., Hanaoka, Y., Shibata, K., Uchida, Y. 1987, Sol. Phys., 108, 251

Kurokawa, H. 1987, Sol. Phys., 113, 259

Kurokawa, H., Takakura, T., Ohki, K. 1988, PASJ, 40, 357

Kurokawa, H. 1988, Vistas in Astronomy, 31, 67

Kurokawa, H. 1989, Space Science Reviews, p. 49

Kurokawa, H., Kawai, G., Kitai, R., Funakoshi, Y., Nakai, Y., Tsuneta, S., Acton, and L. W., Ogawara, Y. 1992, PASJ, 44, 129

Kurokawa, H. & Kawai, G. 1993, in ASP Conf. Ser., 46, The Magnetic and Velocity Fields of Solar Active Regions, ed. H. Zirin, G. Ai, & H. Wang (San Francisco: ASP), 507

Kurokawa, H., & Sano, S. 2000, Adv. Space Res., 26, 441

Kurokawa, H., Wang, T. J., Ishii, T. T. 2002, ApJ, 572, 598

Krucker, S. & Bentz, A. 1998, ApJ, 501, L213

Lin, R. P., et al. 2002, Sol. Phys., 210, 3

Lin, R. P., et al. 2003, ApJ, 595, L69

Masuda, S., Kosugi, T., Hudson, H. S. 2001, Sol. Phys., 204, 57

Masuda, S., Kosugi, T., Hara, H., Tsuneta, S., Ogawara, Y. 1994, Nature, 371, 495

McKenzie, D. E. & Hudson, H. S. 1999, ApJ, 519, L93

McKenzie, D. E. 2000, Sol. Phys., 195, 381

McKenzie, D. E. & Hudson, H. S. 2001, Earth Planets Space, 53, 577

Miyagoshi, T. & Yokoyama, T. 2003, ApJ, 593, L133

Moore, R. L., Sterling, A. C., Hudson, H. S., Lemen, J. M. 2001, ApJ, 552, 833

Moore, R. L. & Roumeliotis, G. 1992, in IAU Colloq. 133, Eruptive Solar Flares, ed., Z. Svestka, B. V. Jackson, & M. E. Machado (New York: Springer), 69

Morimoto, T. & Kurokawa H. 2003a, PASJ, 55, 505

Morimoto, T. & Kurokawa, H. 2003b, PASJ, 55, 1141

Nakajima, H., Kosugi, T., Kai, K., & Enome, S. 1983, Nature, 305, 292

Neupert, W. M. 1968, ApJ, 153, L59

Ogawara, Y., Takano, T., Kato, T., Kosugi, T., Tsuneta, S., Watanabe, T., Kondo, I., & Uchida, Y. 1991, Solar phys., 136, 10

Ohyama, M., Shibata, K. 1997, PASJ, 49, 249

Ohyama, M., Shibata, K. 1998, ApJ, 499, 934

Parker, E. N. 1957, J. Geophys. Res., 62, 509

Parker, E. N. 1991, ApJ, 372, 719

Petschek, H. E. 1964, in AAS-NASA Symp. on Solar Flares, ed. W. N. Hess (NASA SP-50), 425

Pneuman, G. W. 1981, in Solar Flare Magnetohydrodynamics, ed. E. R. Priest, (New York: Gordon & Breach), 379

Priest, E. & Forbes, T., 1990, Sol. Phys., 126, 319

Priest, E. & Forbes, T. 2000, Magnetic Reconnection (Cambridge: Cambridge University Press)

Ricchiazzi, P. J., and Canfield, R. C. 1983, ApJ, 272, 739

Roy, J.-R. 1973, Sol. Phys., 32, 139

Sakao, T. 1994, Ph.D. thesis (University of Tokyo)

Scherrer, P. H., et al. 1995, Sol. Phys., 162, 129

Schrijver, C. J., et al. 1999, Sol. Phys., 187, 261

Shibata, K., et al. 1992, PASJ, 44, L173

Shibata, K., Nitta, N., Strong, K. T., Matsumoto, R., Yokoyama, T., Hirayama, T., Hudson, H., Ogawara, Y. 1994, ApJ, 431, L51

Shibata, K., Masuda, S., Shimojo, M., Hara, H., Yokoyama, T., Tsuneta, S., Kosugi, T., Ogawara, Y. 1995, ApJ, 451, L83

Shibata, K. 1999, Ap&SS, 264, 129

Shimizu, T., et al. 1995, PASJ, 47, 251

Shimojo, M., Hashimoto, S., Shibata, K., Hirayama, T., Hudson, H. S. and Acton, L. W. 1996, PASJ, 48, 123

Sturrock, P. A. 1966, Nature, 211, 695

Sturrock, P. A. 1992, in Eruptive Solar Flares, eds. Z. Švestka, B. V. Jackson, M. E. Machado (Berlin: Springer), 397

Švestka, Z., Cliver, E. W. 1992, in Eruptive Solar Flares, eds. Z. Švestka, B. V. Jackson, M. E. Machado (Berlin: Springer), 1

Sweet, P. A. 1958, in IAU Symp. 6, Electromagnetic Phenomena in Cosmical Physics, ed. B. Lehnert (Cambridge: Cambridge University Press), 123

Tajima, T., Brunel, F., and Sakai, J. 1982, ApJ, 258, L45

Tajima, T., Sakai, J., Nakajima, H., Kosugi, T., Brunel, F., & Kundu, M. R. 1987, ApJ, 321, 1031

Tajima, T. & Shibata, K. 1997, Plasma Astrophysics, Addison-Wesley, Frontiers in physics, v. 98

Tsuneta, S., Hara, H., Shimizu, T., Acton, L. W., Strong, K. T., Hudson, H. S., Ogawara, Y. 1992, PASJ, 44, L63

Tsuneta, S. 1996, ApJ, 456, 840

Wilhelm, K., et al. 1995, Sol. Phys., 162, 189

Wu, S. T., et al. 1986, in Energetic Phenomena on the Sun, ed.s M. Kundu & B. Woodgate (NASA CP-2439), 378

Yokoyama, T. & Shibata, K. 1995, Nature, 375, 42

Yokoyama, T. & Shibata, K. 1996, PASJ, 48, 353

Yokoyama, T. & Shibata, K. 2001, ApJ, 549, 1160

Chapter 2

Evolution of Conjugate Footpoints inside Flare Ribbons During a Great Two-Ribbon Flare*

We present detailed examinations of the fine structure inside flare ribbons and the temporal evolution of such structure during a typical great two-ribbon (X2.3) solar flare, which occurred on 2001 April 10. In this chapter we examined fine structures, such as systems of conjugate footpoints, inside flare ribbons by using the Hα images obtained with the Sartorius telescope at Kwasan Observatory, Kyoto University. We identified the conjugate footpoints of each Hα kernel in both flare ribbons by a new method that uses cross-correlation functions of the light curves. We also compared the sites of the Hα kernels with the spatial configurations of flare loops seen in the extreme-ultraviolet images obtained with the *Transition Region and Coronal Explorer*. We found that the highly correlated pairs of Hα kernels were connected by flare loops seen in the 171 Å images. Investigating such fine structures inside the flare ribbons, we can follow the history of energy release and acquire key information about particle acceleration.

2.1   Motivation

Nonthermal electrons are generated in the impulsive phase of solar flares and mainly observed in microwaves, hard X-rays (HXRs), and γ-rays (see Figs. , , and). The electrons are thought to be accelerated up to several tens of keV or more (e.g., Kane 1981; Aschwanden 1999) near the energy release site or the magnetic reconnection site. The accelerated electrons flow with speeds of roughly one-third the speed of light ($\sim 10^5$ km s^{-1}). Due to such high speeds, they are expected to precipitate into the chromosphere at both the footpoints of the flare loops almost simultaneously. Even when the energy release is asymmetric, time lag of precipitation at both footpoints is still within about 1 s. Kurokawa, Takakura, & Ohki (1988) and Sakao (1994) actually found that the light curves of both the conjugate footpoints are very similar and highly correlated with each other. Figure 2.1 shows temporal correlation among Hα, HXR, and soft X-ray(SXR) emissions. Therefore, the location and time of the acceleration and/or the energy release can be determined by identifying such highly correlated pairs of footpoints and the precipitation times of the nonthermal electrons. If we investigate fine structures inside the flare ribbons, and identify simple units which consist of conjugate footpoints and a flare loops connecting the footpoints as the magnetic reconnection model predicts, we can follow the history of energy release and acquire key information about particle acceleration even for very complexed flares.

Electron precipitation not only produces HXR radiation caused by bremsstrahlung, but also stimulates the excitation and ionization of hydrogen atoms, which in turn cause enhanced Hα emissions immediately (Canfield & Gayley 1987; Trottet et al. 2000; Wang et al. 2000; Qiu et al. 2001). Locations and light curves of the HXR sources show high correlations with those of the Hα kernels (Kurokawa et al. 1988; Kitahara & Kurokawa 1990). Since at the time of this flare, the spatial resolution of Hα images is much higher than that of HXR and/or microwave images, we can investigate the precipitation sites of the nonthermal electrons in more detail by using Hα images.

In this chapter we precisely identify such highly correlated pairs of footpoints by calculating cross-correlation functions between light curves of Hα kernels that appeared during the 2001 April 10 flare. We also determine where and when nonthermal electrons precipitated into the chromosphere by comparing the Hα light curves with the HXR and microwave time profiles. No previous observation has ever succeeded in determining precisely conjugate footpoints, since it has been difficult to judge whether highly correlated pairs of footpoints are really connected by flare loops. Although Kurokawa et al. (1992) examined coincidences of spatial configurations of Hα bright
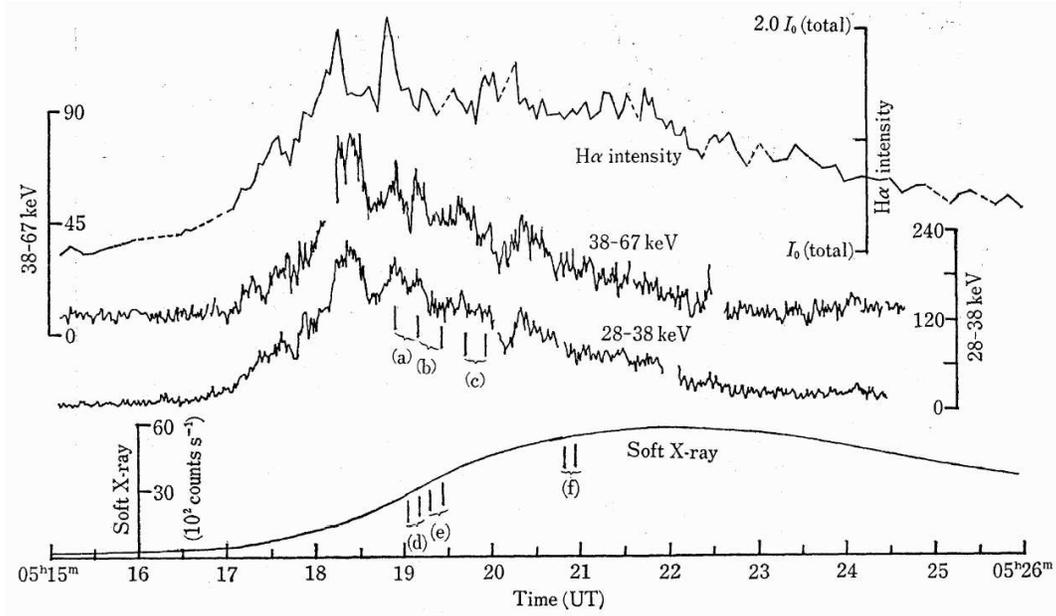
Figure 2.1: Temporal correlation among Hα, HXR, and SXR emissions. Hα intensity is the total of six flare kernels. The HXR light curves in the 38 - 67 keV and 28 - 38 keV ranges are obtained by HXM, and the SXR light curves by FLM on *Hinotori* (Kurokawa et al. 1988, Fig. 4).

kernels with flare loops using SXR images obtained with the soft X-ray telescope (SXT; Tsuneta et al. 1991) aboard *Yohkoh* (Ogawara et al. 1991), they could not confirm coincidences because of the insufficient spatial resolution of SXT. Conversely, the spatial resolution of the *Transition Region and Coronal Explorer* (*TRACE*; Handy et al. 1999; Schrijver et al. 1999) gives us information about post-flare loops with much higher resolution than before. Therefore, in this chapter we examine whether the highly correlated pairs of Hα footpoints are really connected by flare loops by using the *TRACE* 171 Å data. In §2.2 we summarize the observational data. In §2.3 we describe the methods used for analyzing Hα data and selecting highly correlated pairs of Hα kernels. We then compare the pairs with the 171 Å flare loops to determine the conjugate footpoints. In §2.4 we examine the spatial and temporal distribution of the Hα pairs and follow the evolution of the energy release sites. A summary and discussion are given in §2.5.

2.2   Observations

We observed a big two-ribbon flare (X2.3 on the *GOES* scale), which occurred in the NOAA Active Region 9415 (S22°, W01°) at 05:10 UT, 2001 April 10 with the 18 cm Sartorius Refractor (Sartorius) at Kwasan Observatory, Kyoto University. The Hα monochromatic images of the flare were obtained with a Halle Lyot filter of 0.5 Å bandwidth in Hα line center and a Kodak 1.6i Megaplus CCD Camera. The pixel size of the CCD is about 0″6. The temporal and spatial resolutions of the Sartorius data are about 1 s and 1″, respectively. The left panels of Figure 2.2 (I to V) are Sartorius images which show temporal evolution of Hα flare ribbons. The flare shows a typical two-ribbon structure. During the observation, the exposure time was properly regulated so that the fine structure inside the flare ribbons, like Hα kernels, can be clearly seen without saturating. Therefore, we can precisely study temporal variations of the footpoints.

The extreme-ultraviolet (EUV) images of the flare were obtained with *TRACE*, with a pixel size of 0″5. *TRACE* 171 Å images clearly show post-flare loops which confine $\sim$ 1 MK-plasma. The right panels of Figure 2.2 (VI to X) show the temporal evolution of the flare ribbons and the flare loops seen in the *TRACE* 171 Å images. The flare ribbons in the *TRACE* 171 Å images appear nearly simultaneously with the Hα flare ribbons, or just after the energy release, as the result of the precipitation of nonthermal electrons. On the other hand, the formation of the 171 Å post-flare loops are noted after the evolution of the flare ribbons. This is because it takes a certain time for hot plasma, which are heated up to about 10 MK or more, to cool down to 1 MK. During the formation of the 171 Å post-flare loops, we notice the successive changes of the loop directions: the highly sheared loops are observed at the beginning and the more relaxed loops at later stages. Here, the word "relaxed" means that flare loops lie more perpendicular to the neutral line or along the potential magnetic field, and "sheared" means that their directions deviate more from the potential field.

To examine nonthermal electrons, we used the microwave total flux measured with Nobeyama Radioheliograph (NoRH; Nakajima et al. 1994) and the HXR data taken with the hard X-ray telescope (HXT; Kosugi et al. 1991) aboard *Yohkoh*. These instruments have temporal resolutions of 0.1 s and 0.5 s, respectively. Figure 2.3 shows the time profiles in microwaves, SXR, HXR, and Hα. The top solid line is that of NoRH (17 GHz), the dotted line shows the GOES 1.0 - 8.0 Å channel, the middle solid line for the HXT *H* band (53 - 93 keV), and the plus signs at the bottom show total intensities of Hα ribbons obtained with Sartorius. The time profile of the combined Hα ribbons consist of a gradual rise and some spikes. The gradual rise is similar

Sartorius Hα TRACE 171Å
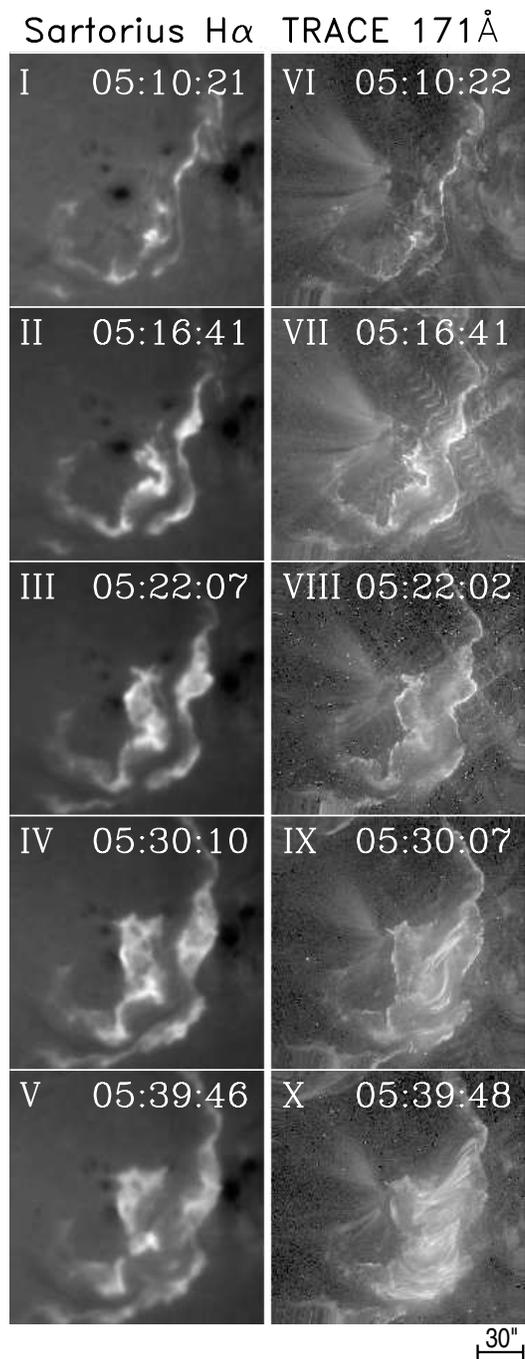
Figure 2.2: Temporal evolutions of the 2001 April 10 flare in Hα and EUV. *Left panels* (I to V): Hα images obtained with the Sartorius. *Right panels* (VI to X): 171 Å image obtained with *TRACE*. Celestial north is up, and west is to the right.
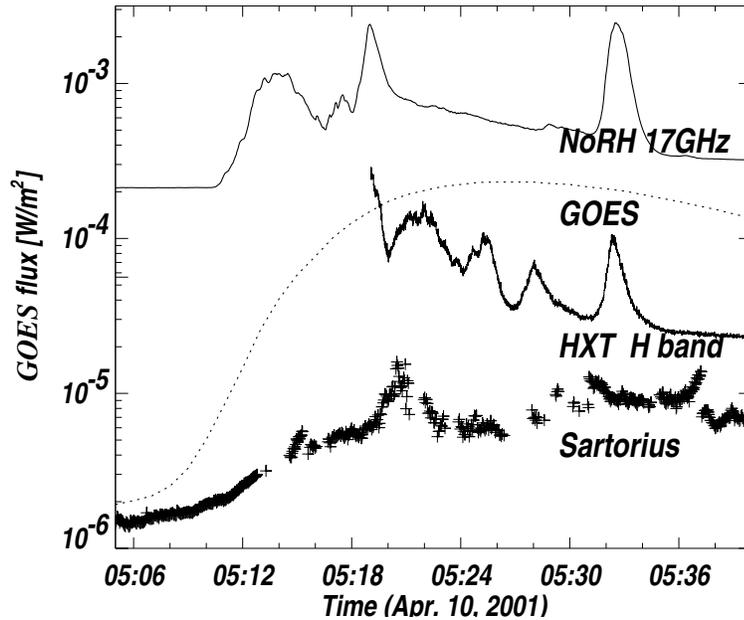
Figure 2.3: Light curves of the flare. *From top to bottom*: Radio correlation plot observed at 17 GHz with NoRH (*scaled arbitrarily*); soft X-ray flux in the *GOES* 1.0-8.0 Å channel (*dotted line*); hard X-ray count rate measured in *H* band (53 - 93 keV) of *Yohkoh*/HXT (*scaled arbitrarily*); and Hα obtained with Sartorius (*plotted with plus signs, scaled arbitrarily*).

to the thermal time profile of the GOES SXR. On the other hand, spiky structure is similar to that of nonthermal profiles, like microwave and HXR as mentioned by Kurokawa et al. (1988) and Kitahara & Kurokawa (1990).

2.3   Identification of Conjugate Footpoints

In this section we focus on the questions of when and where nonthermal electrons precipitated into the chromosphere by studying in detail locations and start times of brightenings of the Hα kernels. We present a new method for the analysis of the brightenings in the Hα flare ribbons (see Fig. 2.4).

Figure 2.4a shows a photospheric magnetogram taken with the Michelson Doppler Imager (MDI; Scherrer et al. 1995) on board the *Solar and Heliospheric Observatory* (*SOHO*; Domingo, Fleck, and Poland 1995). Figure 2.4b is an Hα image obtained at 05:31 UT. We divided both flare ribbons into
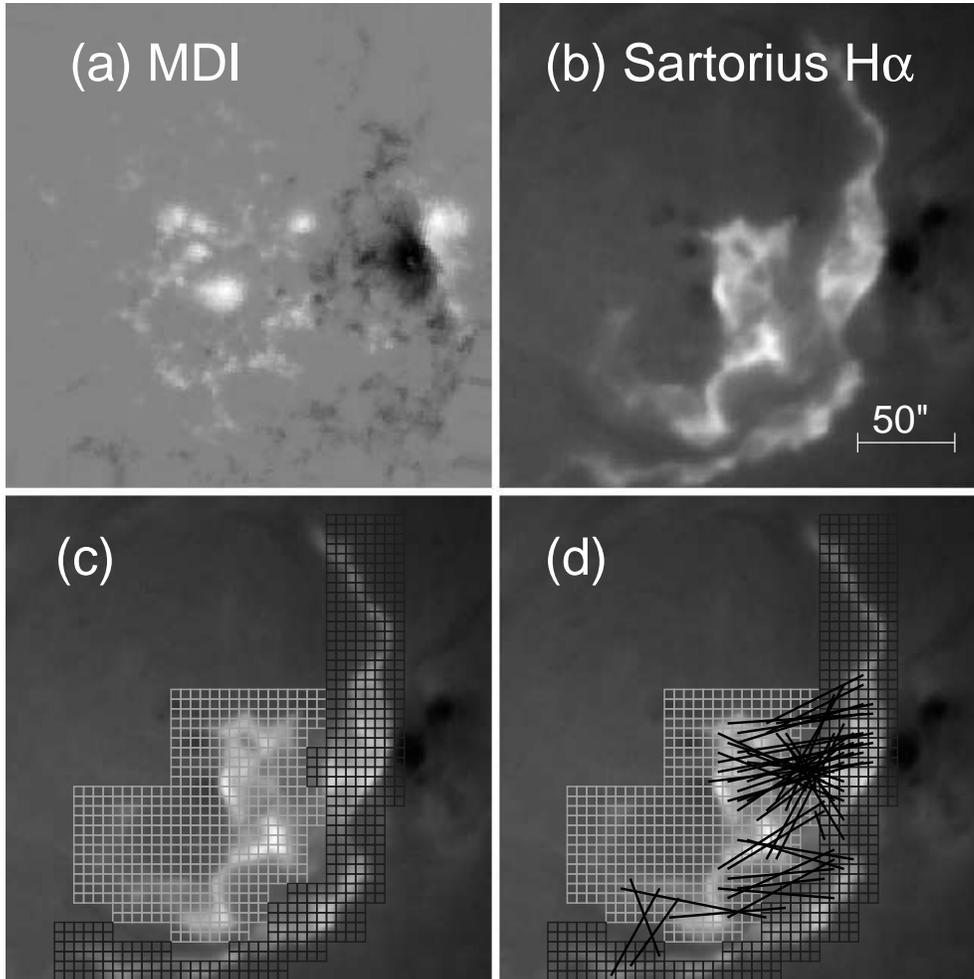
Figure 2.4: Method of analyses. Celestial north is up, and west is to the right. (a) Photospheric magnetogram taken with *SOHO* MDI. (b) Raw Hα image of the Sartorius at 05:31 UT. (c) Hα image overlaid with the fine meshes on (b). The left (*east*) mesh drawn with light gray lines is positive polarity, and the right (*west*) one with dark gray lines is negative polarity. (d) Hα image overlaid with black solid lines which connect highly correlated pairs on (c).

fine meshes (see Fig. 2.4c). The two flare ribbons have opposite magnetic polarities. In Figure 2.4c the light gray (*left*) mesh covers positive polarity, and the dark gray (*right*) mesh, overlies the negative polarity. Each mesh box is square with sides of $\sim 4.8''$. Although this is larger than elemental Hα kernels, which are considered to be about $1''$ or even smaller (Kurokawa 1986), it is small enough for us to determine the essential characteristics of structures inside the flare ribbons. Next, we drew light curves of total intensity for each box in both the meshes. We defined the "flare ribbons" as the region in which the maximum intensity is twice as that of the surrounding quiet region, at least at some moment in the flare duration. The regions outside ribbons are excluded from the analysis. Then, we identified the highly correlated pairs (partners), the two points that show the synchronized time variation in Hα. For all the boxes in *one* mesh, e.g., with positive polarity, we calculated cross-correlation functions with all boxes in the *other* mesh, which has the opposite magnetic polarity (i.e., negative polarity), and searched for the highest correlated box. It sometimes happened that two or more boxes of the positive flare ribbon selected the same box of the negative flare ribbon as their partner. Therefore, to determine the "one-to-one" high correlated pairs, the next operation of cross-correlation was done on the negative flare ribbon with the positive one. If this second operation chooses the same pair as the first operation, we define this pair of points as "highly correlated" pair. In other words, only when each box of one pair selects the other box as the highest correlated box at each operation, they were defined as "highly correlated" pair. Even if a box of the negative flare ribbon was selected as the highest correlated partner by a box of the positive flare ribbon at the first operation, the former might not select the latter but another box as the highest correlated one in the second operation. In such a case, we did not define them as a pair. In Figure 2.4d black solid lines are drawn to connect such highly correlated pairs.

We examined the spatial relation between the post-flare loops seen in the *TRACE* 171 Å images and the highly correlated pairs of the Hα kernels. We checked whether or not the Hα pairs are actually connected by the 171 Å flare loops. Figure 2.5 shows the comparison of their locations. Some Hα pairs selected above are connected with black solid lines in the right panels of Figure 2.5. Almost all the pairs are connected by 171 Å flare loops, and only a few pairs have no correspondence to any 171 Å flare loops. As a result, 33 pairs were determined as the "conjugate footpoints" of the 171 Å flare loops. This good coincidence between the Hα pairs and the 171 Å flare loops strongly supports the scenario of the flare loop formation: the 171 Å flare loops are formed by the plasma evaporated from the brightening Hα pairs. Notice that the spatial distribution of the Hα pairs shows a strongly
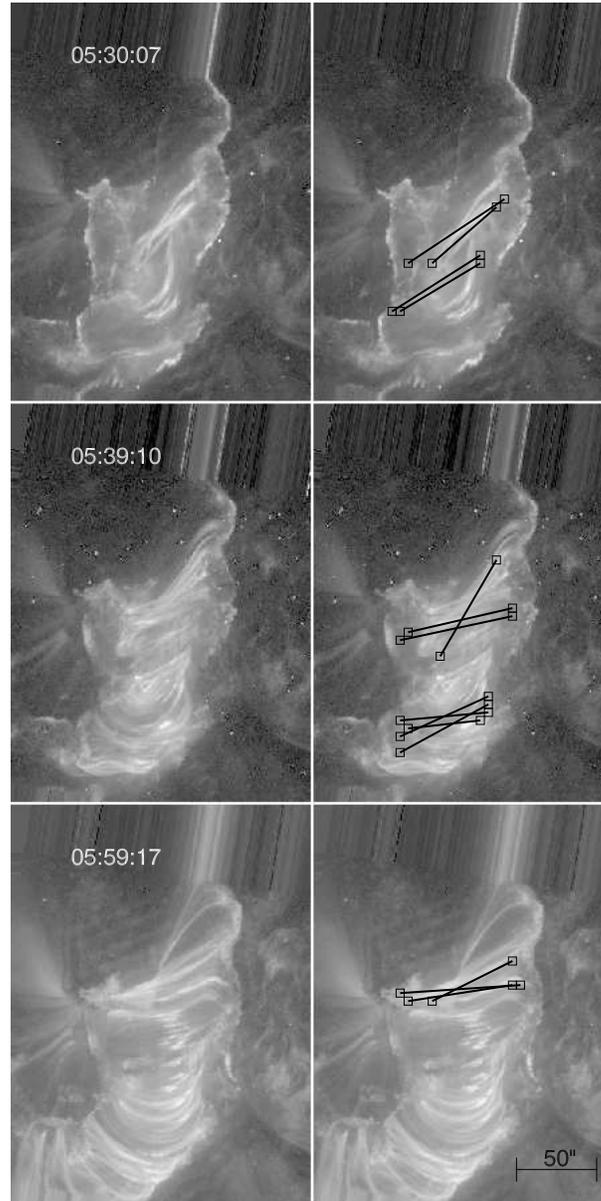
Figure 2.5: Comparison of the spatial configuration between the highly correlated pairs of the Hα kernels and the post-flare loops seen in the *TRACE* 171 Å. Celestial north is up, and west is to the right. *Left panels*: *TRACE* 171 Å images. *Right panels*: *TRACE* 171 Å images overlaid with the solid lines that connect some highly correlated pairs of Hα kernels.

Table 2.1: Classification of pairs of Hα kernels (total 33 pairs)

Group	Number of Pairs (North/South)	Approximate Brightening Times (UT)
1	7 (2/5)	05:11:30
2	8 (4/4)	05:14:15
3	8 (8/0)	05:17:40
4	4 (4/0)	05:19:20
5	6 (6/0)	05:23:40

sheared structure at the beginning and the more relaxed structure later. Such an evolution of Hα pairs contains information of the magnetic field configuration of the energy release sites. We discuss this in more detail in the next section.

2.4   Fine Structure inside Flare Ribbons

Here we examine in detail the temporal and spatial evolution of the pairs of the Hα conjugate footpoints selected in §2.3. The start times of brightening of each Hα pair tell us the site and the time of the energy release or the magnetic field reconnection. We follow the evolution of the energy release sites by examining the fine structures inside the flare ribbons, or Hα kernels.

To follow global evolution, we classified the Hα pairs into five groups according to the brightening times of each pair. The light curves and the sites of the pairs in each group are shown in Figure 2.6, and the classification is summarized in Table 2.1. At the beginning of the flare ribbon evolution, the Hα kernels appear in the northern and the southern part of the ribbons. Especially in southern part, the clear brightenings of the Hα pairs are seen only in groups 1 and 2 (see Fig. 2.6, *top right panel*, and Table 2.1). Most of lines connecting the Hα pairs in groups 1 and 2 are nearly parallel to the magnetic neutral line or are in a strongly sheared configuration. As the flare progresses, the flare ribbons quickly separate from each other, and many Hα kernels appear successively in northern part. The pairs that belong to group 3, 4, and 5 appear only in northern area (see Fig. 2.6, *bottom right panel*). The expansion of the ribbons lasts for much longer time in the north than in the south. The locations of the Hα kernels tend to move toward the northeast in the eastern ribbon and the southwest in the western ribbon (see Fig. 2.6, *right panels*). Such changes from the strongly sheared to less-sheared directions of the lines that are connecting Hα pairs were also

found in the previous works (Kitahara & Kurokawa 1990) and indicate the configuration of the height-dependent sheared magnetic field in the corona over the neutral line.

The Hα pairs that belong to the same group brighten almost simultaneously. Moreover, the start times of brightening of each group are almost simultaneous with those of the nonthermal bursts seen in HXRs and microwaves (see Fig. 2.6, *broad arrows in the left panel*). It shows that the flare ribbons expand and many Hα kernels appear when there are large energy releases, which are seen as the nonthermal bursts in HXRs and microwaves. When we consider each group in more detail, however, the Hα pairs in each group have slightly different in brightening times from each other. This shows that the energy release occurs successively during nonthermal bursts and the successive energy release may be responsible to subpeaks seen in the bursts (see Fig. 2.3).

2.5 Summary and Discussions

We examined in detail the temporal and spatial evolution of the fine structure inside the flare ribbons with a new method. We have identified the conjugate footpoints in both the flare ribbons with different magnetic polarities by calculating cross-correlation functions of the light curves of each Hα kernel. Using the Hα images obtained with the Sartorius telescope at Kwasan Observatory, we investigated the conjugate footpoints with higher spatial resolution than possible with HXR and microwave data. Second, we examined whether or not the pairs of Hα conjugate footpoints are really connected by the post-flare loops seen in the *TRACE* 171 Å images and found, for the first time, that almost all the Hα pairs are connected by the 171 Å loops.

This result strongly supports the flare scenario that the Hα kernels are brightened by the precipitation of high-energy electrons or by heat conduction and that evaporated plasma from the Hα kernels produces the high-temperature flare loops observed in SXR and EUV. Our finding suggests that we can study the magnetic field configuration in the energy release sites by examining evolution of Hα kernels. We have been able to follow the formation of the flare loops and the evolution of energy release sites.

The lines that are connecting the pairs of the Hα conjugate footpoints were found to turn from the strong-to-weak shear configuration. The post-flare loops seen in the *TRACE* 171 Å images also show the tightly sheared structure in the beginning, then larger and more relaxed structures later. Such an evolution of flare loops indicates that the configuration of a height-
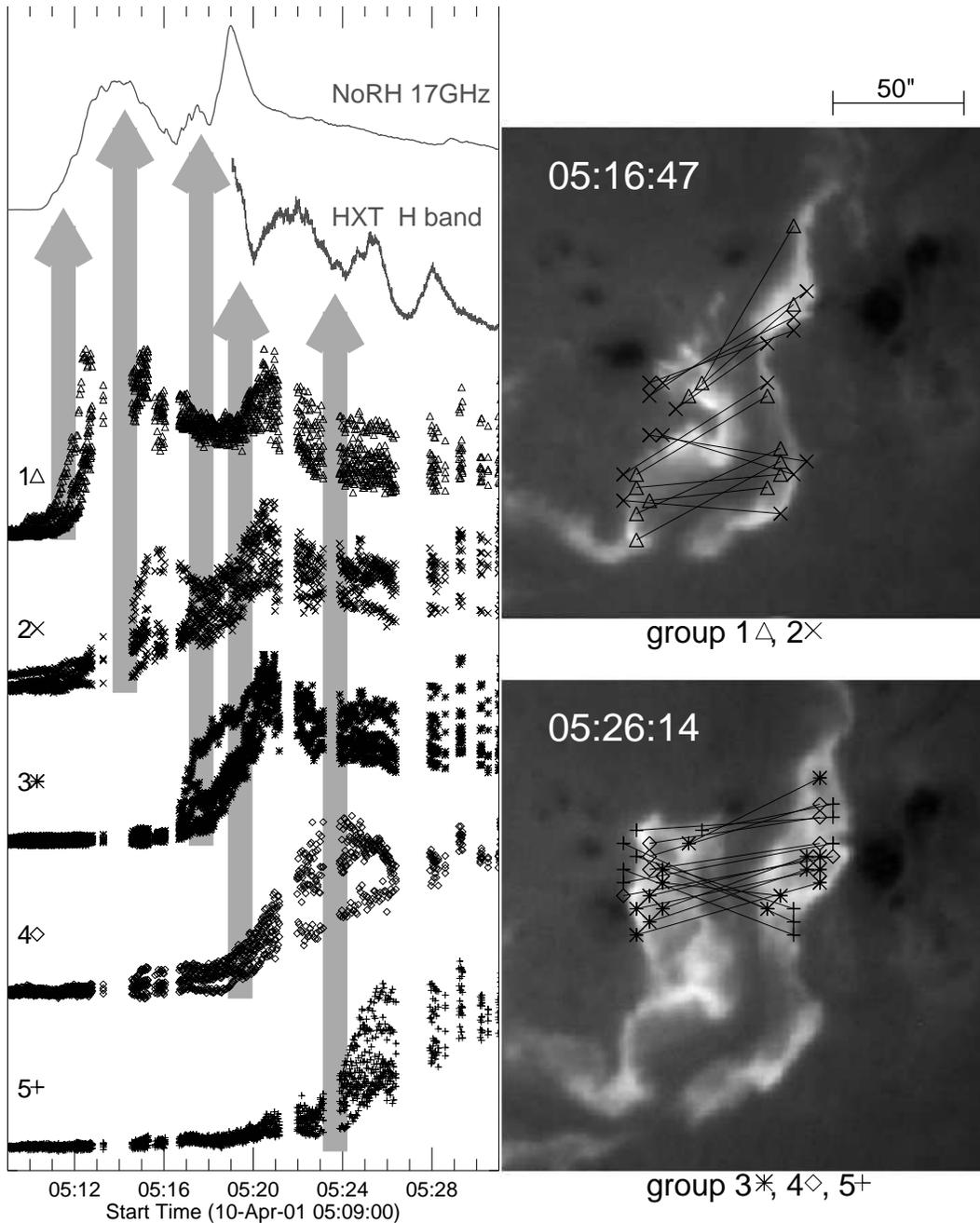
Figure 2.6: Temporal and spatial evolutions of the pairs of the Hα conjugate footpoints. *Left panel*: Light curves (*scaled arbitrarily*). The top two dark gray lines show microwave and hard X-ray fluxes, and the other curves are for each Hα group as numbered at the left side. They are plotted with different symbols for each group, as shown on the left. Light gray broad vertical arrows show rough brightening times of each group. *Right panels*: Hα images marked with pairs of the Hα conjugate footpoints. *Top panel*: Groups 1 and 2. *Bottom panel*: Groups 3, 4 and 5. Celestial north is up, and west is to the right. The marks are the same as those of the time profiles in left panel.

dependent sheared magnetic field had been formed in the corona over the magnetic neutral lines before the flare. In other words, the large and less-sheared configuration of magnetic field lies over the inner sheared magnetic structure. It may be caused by the emergence of tightly twisted flux tubes and their relaxations (Ishii, Kurokawa, & Takeuchi 2000). Note that the movement of footpoints from strong-to-weak sheared structure are also observed in HXRs (Masuda, Kosugi, & Hudson 2002).

The evolution of the southern part of the flare ribbons is much different from that of the north. The duration of the flare ribbon evolution in the south is much shorter, as mentioned in §2.4, and the apparent width of the ribbons is also much thinner than that of the northern ribbons. This difference of evolution of the flare ribbons between the south and the north may result from the difference of the amount and/or the mechanism of energy release. The difference of the apparent thickness of the flare ribbons may be caused by the initial global magnetic field and differences of magnetic field strength. Therefore, we need to investigate in more detail the relation of global structure of the flaring region with the amount of energy release and examine the factors that cause such a difference of the energy release.

Bibliography

Aschwanden, M. J. 1999, in The many faces of the sun, ed. K. T., Strong, et al. (New York: Springer), 273

Canfield, R., and Gayley K. G. 1987, ApJ, 322, 999

Domingo, V., Fleck, B., Poland, A. I., 1995 Sol. Phys., 162, 1

Handy, B. N., et al., 1999, Sol. Phys., 187, 229

Ishii, T. T., Kurokawa, H., & Takeuchi, T. T. 2000, PASJ, 52, 337

Kane, S. R. 1981, ApJ, 247, 1113

Kitahara, T. & Kurokawa, H. 1990, Sol. Phys., 125, 321

Kosugi, T., et al. 1991, Sol. Phys., 136, 17

Kurokawa, H. 1986, the Low Atmosphere of Solar Flares; Proc. of NSO/SMM Flare Symp., ed. D. Neidig, 51

Kurokawa, H., Takakura, T., Ohki, K. 1988, PASJ, 40, 357

Kurokawa, H., Kawai, G., Kitai, R., Funakoshi, Y., Nakai, Y., Tsuneta, S., Acton, and L. W., Ogawara, Y. 1992, PASJ, 44, 129

Masuda, S., Kosugi, T., and Hudson, H. S. 2002, Sol. Phys., 204, 57

Nakajima, H., et al. 1994, Proc. IEEE, 82, 705

Ogawara, Y., Takano, T., Kato, T., Kosugi, T., Tsuneta, S., Watanabe, T., Kondo, I., and Uchida, U. 1991, Sol. Phys., 136, 1

Qiu, J., Ding, M. D., Wang, H., Gallagher, P. T., Sato, J., Denker, C., and Goode, P. 2001, ApJ, 554, 445

Sakao, T. 1994, Ph.D. thesis (University of Tokyo)

Scherrer, P. H., et al. 1995, Sol. Phys., 162, 129

Schrijver, C. J., et al. 1999, Sol. Phys., 187, 261

Trottet, G., Rolli, E., Magun, A., Barat, C., Kuznetsov, A., Sunyaev, R., and Terekhov, O. 2000, A&A, 356, 1067

Tsuneta, S., et al. 1991, Sol. Phys., 136, 37

Wang, H., Qiu, J., Denker, C., Spirock, T., Chen, H., and Goode R. 2000, ApJ, 542, 1080

Chapter 3

Difference between Spatial Distributions of the Hα Kernels and Hard X-Ray Sources in a Solar Flare**

In this chapter we present a new interpretation for the relation of the spatial distribution of Hα kernels with the distribution of hard X-ray (HXR) sources by using observational data of the 2001 April 10 solar flare. This flare was observed in Hα with the Sartorius telescope at Kwasan Observatory, Kyoto University, and in HXRs with the Hard X-ray Telescope (HXT) on board *Yohkoh*. We compared the spatial distribution of the HXR sources with that of the Hα kernels. While many Hα kernels are found to brighten successively during the evolution of the flare ribbons, only a few radiation sources are seen in the HXR images. We measured the photospheric magnetic field strengths at each radiation source in the Hα images and found that the Hα kernels accompanied by HXR radiation have magnetic strengths about 3 times larger than those without HXR radiation. We also estimated the energy release rates based on the magnetic reconnection model. The release rates at the Hα kernels with accompanying HXR sources are 16-27 times larger than those without HXR sources. These values are sufficiently larger than the dynamic range of HXT, which is about 10, so that the difference between the spatial distributions of the Hα kernels and the HXR sources can be explained.

3.1 Introduction of This Chapter

In the impulsive phase of a solar flare, precipitations of nonthermal electrons from the corona generate radiation from denser layers, such as the transition region and/or the upper chromosphere. This radiation is often observed in hard X-rays (HXRs) or microwaves. Precipitations of nonthermal electrons also cause radiation sources in Hα because of rapid thermalization or other mechanisms. Therefore, Hα kernels and HXR sources show a high correlation in their locations and light curves (Kitahara & Kurokawa 1990). However, the difference between the spatial distributions of Hα kernels and HXR sources is also well known. Hα images sometimes show elongated brightenings, called Hα flare ribbons, with many Hα kernels within them. The size of elemental Hα kernels is considered to be about $1''$ or even smaller (Kurokawa 1986), which is larger than the spatial resolution achieved with Hα instruments ($\sim 0''.2$) but is smaller than that with HXR instruments of about $5''$. On the other hand, HXR images show very few sources, sometimes only one. HXR sources are accompanied by Hα kernels in many cases, but many Hα kernels are not accompanied by HXR sources. The only exception to this "lack of radiation sources in HXRs" that is known is the Bastille Day event on 2000 July 14 (Masuda, Kosugi, & Hudson 2001). This event shows a clear two-ribbon structure in HXRs such as in Hα.

This difference of spatial distributions may be explained by the difference in radiation mechanisms between HXRs and Hα. The HXR intensity is proportional to the number of accelerated electrons and is thought to be proportional to the energy release rate (Hudson 1991; Wu et al. 1986). Therefore, only compact regions where the largest energy release occurred are observable as HXR sources. On the other hand, the mechanisms for Hα radiation are much more complicated than those for HXR radiation, and to derive the effect of electrons is quite difficult (Ricchiazzi & Canfield 1983; Canfield, Gunkler, & Ricchiazzi 1984). Some weaker Hα kernels may be caused by a secondary effect of precipitation or thermal conduction. However, as we mentioned above, the light curve of each Hα kernel has a high correlation with that of the total HXR intensity, even if their intensity is not so strong and they do not have an HXR counterpart. We suggest that the difference between the spatial distributions of Hα kernels and HXR sources is caused by the low dynamic range of the HXR data. In the HXR images, only the strongest sources are seen, and the weaker sources are buried in the noise. We use the HXR data taken with the hard X-ray telescope (HXT; Kosugi et al. 1991) on board *Yohkoh* (Ogawara et al. 1991) in this chapter. The dynamic range of the HXT images is about 10. Therefore, if the released energy at the Hα kernels associated *with* HXR sources is at least 10 times

larger than that at the Hα kernels *without* HXR sources, then the difference of appearance can be explained.

In this chapter, we measure the photospheric magnetic field strengths at each radiation source seen in Hα images which have much higher spatial resolution than HXR images. We also estimate the energy release rates based on the magnetic reconnection model (Isobe et al. 2002) at each radiation source. Then we compare the energy release rates with the spatial distribution of radiation sources in an HXR image since they suggest the site where the strong energy release occurred. To examine the difference of the amount of the released magnetic energy, we measured the photospheric magnetic field strengths at each radiation source. In §3.2, we summarize the observational data and the results. In §3.3, we discuss the amount of energy release at each radiation source. In §3.4, the summary and the conclusion are given.

3.2 Observations and Results

We observed a large two-ribbon flare (X2.3 on the GOES scale), which occurred in the NOAA Active Region 9415 (S22°, W01°) at 05:10 UT, 2001 April 10, with the Sartorius Refractor Telescope at Kwasan Observatory, Kyoto University. The highest temporal and spatial resolutions of the Sartorius data are 1 s and $1''.2$, respectively. The details of the flare were reported in several papers (Asai et al. 2003; Pike & Mason 2002; Foley et al. 2001). To compare the locations of the HXR radiation sources with those of the Hα kernels, we used the HXR data taken with HXT, whose temporal and spatial resolutions are 0.5 s and $5''$, respectively. We also used a magnetogram obtained at 05:18 UT with the Michelson Doppler Imager (MDI; Scherrer et al. 1995) on board the *Solar and Heliospheric Observatory* (*SOHO*; Domingo, Fleck, and Poland 1995) to measure photospheric magnetic field strengths. The spatial resolution of the MDI image is about $3''.9$.

Figure 3.1 shows the images of the flare at 05:19 UT in Hα and HXR. We overlaid the HXR contour image on the Hα image (Fig. 3.1b), to compare the spatial distribution of radiation sources in these two wavelengths. There are many Hα kernels inside the flare ribbons. In Figure 3.1a we can identify 10 Hα kernels by eyes, which are numbered from E1 to E6 and from W1 to W4. Here "E" and "W" mean the eastern and the western flare ribbons, respectively.

On the other hand, the HXR image (Fig. 3.1b) shows only two sources even at the contour level of 10% of the peak intensity. These HXR sources are associated with the Hα kernels E2 and W2. We confirmed that those Hα kernels, E2 and W2, are conjugate footpoints (Asai et al. 2003). The soft
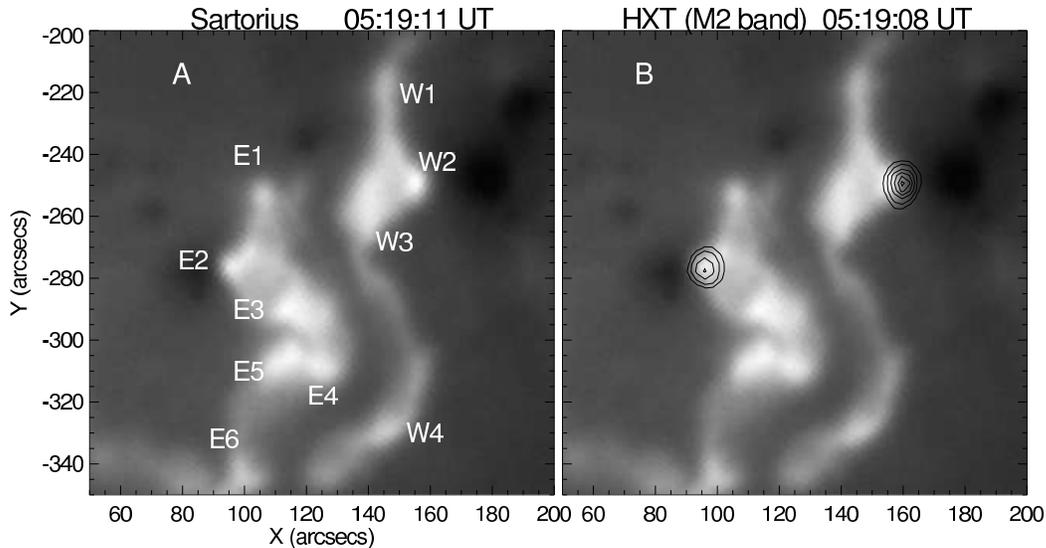
Figure 3.1: Hα image of the flare at 05:19 UT. Solar north is up, and west is to the right. (a) Hα image taken with Sartorius in which 10 Hα bright kernels are numbered from E1 to E6 and from W1 to W4. (b) Hα image overlaid with the HXR contour image to compare the spatial distribution of Hα kernels with that of the HXR sources. Contour levels are 95%, 80%, 60%, 40%, 20% and 10% of the peak intensity.

X-ray images of the flares taken with the Soft X-ray Telescope (Tsuneta et al. 1991) on board *Yohkoh* also show the flare loops that connect E2 and W2. Such differences between the spatial distributions of the Hα kernels and the HXR sources may be caused by the differences in energy release rates at each radiation source. We measured the magnetic field strengths at each Hα kernel, both with and without HXR sources, and estimated their energy release rates. Then we compared these rates with the spatial distribution of the HXR sources. The estimation is discussed in §3.3. Here we examine the relation between the photospheric magnetic field strength and the radiation sources.

Figure 3.2 shows the Hα image in which the flare ribbons are clearly seen (*left panel*), and the photospheric magnetogram of the same region obtained with MDI (*right panel*). The outer edges of the Hα flare ribbons are plotted by cross signs in both the panels of Figure 3.2. The magnetic reconnection model indicates that the newest energy release occurs on the outermost flare loops, and the Hα kernels and HXR sources appear at the footpoints of the flare loops, say, at the fronts of the Hα flare ribbons. Therefore, we measured
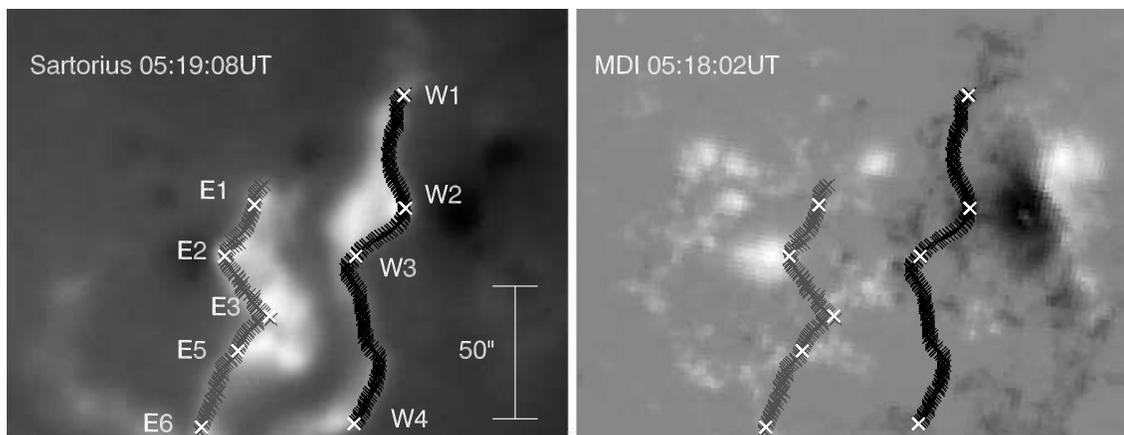
Figure 3.2: Hα images (Sartorius) and photospheric magnetogram (MDI). Celestial north is up, and west is to the right. The outer edges of both the flare ribbons are plotted by crosses. Gray and black plots show the east (positive) and west (negative) magnetic polarity, respectively.

the photospheric magnetic field strengths along the outer edges of the flare ribbons. The source E4 is excluded from the discussion, because it is not located on the ribbon-front.

Figure 3.3 shows the photospheric magnetic field strengths along the outer edges of both the Hα flare ribbons. The *left gray* plot shows the magnetic strengths for the east ribbon with positive magnetic polarity, and the *right black* plot is for the west ribbon with negative magnetic polarity. The magnetic field strengths at the Hα kernels are higher than in the other non-kernel regions, 300 G on average, and those at the HXR sources (E2 and W2) are especially high ($\sim$ 1000 G). We summarize the magnetic field strengths at each Hα kernel in Table 3.1. The photospheric magnetic field strengths of the Hα kernels accompanied by HXR sources are about 3 times larger than the other Hα kernels.

3.3 Energy Release Rate

In this section, we examine the energy release rates in the flare ribbons and discuss the relation between the rates and the spatial distribution of the Hα kernels and HXR sources. We assume that the HXR intensity observed with the HXT is proportional to the energy release rate dE/dt owing to magnetic reconnection. The energy release rate is written as the product of
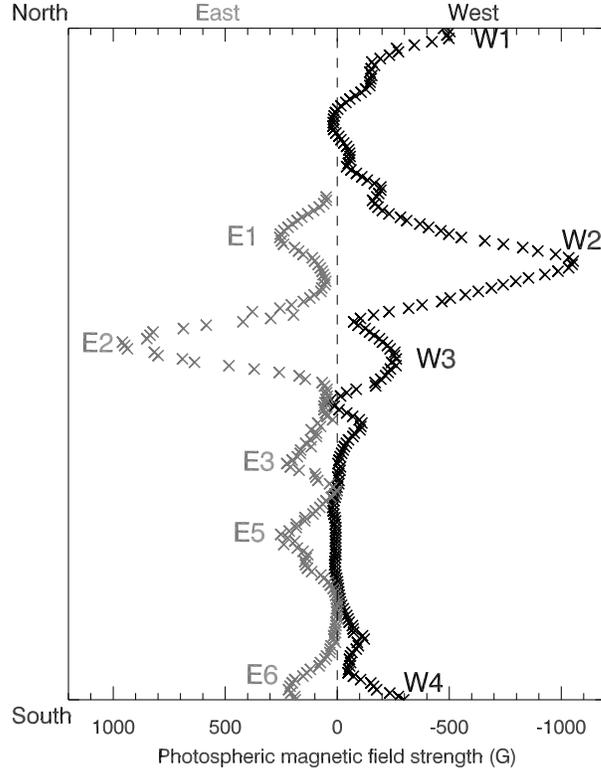
Figure 3.3: Magnetic field strength along the outer edges of both the flare ribbons (see Fig. 3.2). Left gray plot shows the east (positive) ribbon, right black plot shows the west (negative) one. Note E1 - E6 (except for E4) and W1 - W4 indicate the position of Hα kernels. E2 and W2 are associated with HXR sources.

the Poynting flux into the reconnection region $(4\pi)^{-1}B_c^2 v_i$ and the area of the reconnection region A (Isobe et al. 2002) as follows;

$$\frac{dE}{dt} = \frac{B_c^2}{4\pi} v_i A, \qquad (3.1)$$

where B_c is the magnetic field strength in the corona and v_i is the inflow velocity into the reconnection region. For simplicity, we assume that the area of the reconnection region does not change much during the flare and is independent of the magnetic field strength. Therefore, the energy release rate is simply written as $dE/dt \propto B_c^2 v_i$. Here we use magnetic field strengths at the the photosphere B_p instead of those at the corona B_c to estimate the energy release rates, since to measure B_c directly is difficult. We assume that

B_c is proportional to B_p in the same ratio all over the flaring region. If this assumption is true, the differences of the energy release rates estimated with B_p are the same as those with B_c. From now on, we estimate the energy release rate by using the photospheric magnetic field strength, and we write it simply as B.

If v_i has no dependence on B, the energy release rate is directly proportional to the square of the magnetic field strength, $dE/dt \propto B^2$. Since the Hα kernels accompanied by HXR radiation have magnetic field strengths about 3 times larger than those without the HXR radiation, the energy release rates at the former are about 9 times larger than those at the latter. The difference in the energy release rates is just comparable to the dynamic range of the HXT (~ 10), but is not enough for weaker radiation sources to be buried in noise. At other Hα kernels, HXR sources should be observed. Therefore, under this assumption the spatial distribution of radiation sources cannot be explained.

This result suggests that v_i may have some dependence on B as some authors have suggested. Sweet (1958) and Parker (1957) give the relation $v_i = R_m^{-1/2} v_A$, where R_m is the magnetic Reynolds number, and v_A is the Alfvén velocity. Here v_A is expressed as $v_A = (4\pi\rho)^{-1/2} B_c \propto B_c$, where ρ is the mass density; R_m is defined as $R_m = L v_A / \eta \propto B$, where L and η are the characteristic length of the flare region and the magnetic diffusivity, respectively. Therefore, we can derive the relation $v_i \propto B^{1/2}$, and then $dE/dt \propto B^{5/2}$. On the other hand, Petschek (1964) suggests that v_i hardly depends on R_m, and indicates $v_i \propto (\log R_m)^{-1} v_A \approx v_A \propto B$. Hence, we can derive the relation $dE/dt \propto B^3$. Since B at the HXR sources is 3 times larger, these two models of magnetic recconection predict that the energy release is 16 and 27 times stronger for the Hα sources accompanied by HXR sources than for the other Hα kernels, respectively. This is sufficiently larger than the dynamic range of HXT, and the difference between the spatial distributions can be explained.

3.4 Summary and Conclusion

We have examined the difference between the spatial distributions of Hα kernels and HXR sources. The HXR sources indicate where large energy release has occurred, while the Hα kernels show the precipitation sites of nonthermal electrons with higher spatial resolution. We measured the photospheric magnetic field strength at each Hα kernel, and found that the magnetic field strengths at the Hα kernels accompanied by HXR sources are about 3 times higher than those at the other Hα kernels (without any HXR sources). We

Table 3.1: Photospheric magnetic field strengths at Hα kernels

Hα kernel	Magnetic Field Strength (G)	HXR Association
E1	260	no
E2	960	yes
E3	240	no
E5	230	no
E6	220	no
W1	-500	no
W2	-1050	yes
W3	-260	no
W4	-300	no

also estimated their energy release rates, by using the photospheric magnetic field strengths and by considering the dependence of v_i on B as derived by some authors (e.g. Sweet 1958; Parker 1957; Petschek 1964). The estimated energy release rates at the HXR sources are large enough to explain the difference of appearance of the Hα and HXR images.

The gap in our understanding of large-scale structure such as Hα flare ribbons and compact radiation sources has been well known not only in HXRs, but also in microwaves. Even in SXRs, flare loops often appear only in a part of the whole flaring region and/or seem to connect only a few radiation sources. The lack of radiation sources does not mean that no energy release occurs there. We just cannot "observe" the radiation because of the dynamic ranges of the instrument for those wavelengths.

We compared the photospheric magnetic field strenghts at each Hα kernel with the spatial distribution of HXR sources, and found that HXR sources appear at strong magnetic regions. However, our result was based on only one event, and the statistical studies about the relation between HXR intensities and magnetic field strengths are needed. We will be able to perform more detailed analysis in the near future by using HXR images, with a higher dynamic range, obtained with the *Reuven Ramaty High Energy Solar Spectroscopic Imager*.

Bibliography

Asai, A., Ishii, T. T., Kurokawa, H., Yokoyama, T., and Shimojo, M. 2003, ApJ, 586, 624

Canfield, R. C., Gunkler, T. A., and Ricchiazzi, P. J. 1984, ApJ, 282, 296

Domingo, V., Fleck, B., Poland, A. I. 1995, Sol. Phys., 162, 1

Foley, C. R., Harra, L. K., Culhane, J. L., and Mason, K. O. 2001, ApJ, 560, L91

Hudson, H. S. 1991, Sol. Phys., 133, 357

Isobe, H., Yokoyama, T., Shimojo, M., Morimoto, T., Kozu, H., Eto, S., Narukage, N., and Shibata, K. 2002, ApJ, 566, 528

Kitahara, T. & Kurokawa, H., 1990 Sol. Phys., 125, 321

Kosugi, T., et al. 1991, Sol. Phys., 136, 17

Kurokawa, H. 1986, in Proc. of NSO/SMM Flare Symp., the Low Atmosphere of Solar Flares, ed. D. Neidig, (National Solar Observatory, Sacramento Peak, Sunspots), 51

Kurokawa, H., Takakura, T., Ohki, K. 1988, PASJ, 40, 357

Masuda, S., Kosugi, T., Hudson, H. S. 2001, Sol. Phys., 204, 57

Ogawara, Y., Takano, T., Kato, T., Kosugi, T., Tsuneta, S., Watanabe, T., Kondo, I., and Uchida, Y. 1991, Sol. Phys., 136, 1

Parker, E. N. 1957, J. Geophys. Res., 62, 509

Petschek, H. E. 1964, in AAS-NASA Symp. on Solar Flares, ed. W. N. Hess (NASA SP-50), 425

Pike, C. D., Mason, H. E. 2002, Sol. Phys., 206, 359

Ricchiazzi, P. J., and Canfield, R. C. 1983, ApJ, 272, 739

Sweet, P. A. 1958, in IAU Symp. 6, Electromagnetic Phenomena in Cosmical
    Physics, ed. B. Lehnert (Cambridge: Cambridge University Press), 123

Scherrer, P. H., et al. 1995, Sol. Phys., 162, 129

Tsuneta, S., et al. 1991, Sol. Phys., 136, 37

Wu, S. T., et al. 1986, in Energetic Phenomena on the Sun, ed.s M. Kundu
    & B. Woodgate (NASA CP-2439), 5-i

Chapter 4

Flare Ribbon Expansion and Energy Release Rate[†]

In this chapter we present a more detailed analyses of the relation between the evolution of the Hα flare ribbons and the released magnetic energy in a solar flare which occurred on 2001 April 10. Based on the magnetic reconnection model, the released energy was quantitatively calculated by using the photospheric magnetic field strengths and separation speeds of the fronts of the Hα flare ribbons. We compared the variation of the released energy with the temporal and spatial fluctuations in the nonthermal radiation observed in hard X-rays (HXRs) and microwaves. These nonthermal radiation sources indicate when and where large energy releases occur. We also estimated the magnetic energy released during the flare. The estimated energy release rates in the Hα kernels associated with the HXR sources are locally large enough to explain the difference between the spatial distribution of the Hα kernels and the HXR sources. We also successfully reconstructed the peaks in the nonthermal emission by using the estimated energy release rates. With such results, we first succeeded to show the magnetic reconnection model of the two-ribbon flare is quantitatively consistent with the observed variations of Hα, HXR, and microwave emissions.

4.1 Motivation

Where and when does the energy release occur in a solar flare? In addition, what quantity of energy is released? It is very important to answer these questions in order to understand the mechanisms which trigger and excite solar flares. Here, we first discuss the magnetic reconnection model which we suggest in this thesis, although it is a repetition of §1.3. The magnetic reconnection model proposed by Carmichael (1964), Sturrock (1966), Hirayama (1974), and Kopp & Pneuman (1976) (CSHKP model) suggests that magnetic field lines successively reconnect in the corona, and can explain such well-known features of solar flares such as the growing flare loops and the formation of the Hα two-ribbon structures at their footpoints. A good review of the CSHKP model is presented by Sturrock (1992) and Švestka & Cliver (1992). The Hα flare ribbons are caused by the precipitation of non-thermal particles and the effect of thermal conduction. As the magnetic field lines reconnect, the reconnection points (X-points) move upward. Therefore, newly reconnected field lines have their footpoints further out than that of the field lines that have already reconnected. Hence, the separation of the flare ribbons is not a real motion, but an apparent one. The relation between the features of two-ribbon flares and the CSHKP model is summarized by Pneuman (1981). These magnetic reconnection models have been further extended by e.g. Priest & Forbes (1990, 2000), Moore & Roumeliotis (1992), Moore et al. (2001), Shibata (1999), and Yokoyama & Shibata (2001). In Figure 4.1 we present a cartoon of the magnetic reconnection model. The solid lines show the magnetic field lines. The reconnected magnetic field lines form post-flare loops with a cusp shaped structure (gray regions). Non-thermal particles and thermal conduction propagate along the reconnected loops from the reconnection site to the footpoints (dashed arrow). As they precipitate into the chromosphere at the footpoints, the Hα flare ribbons are generated (dark gray regions). The Hα flare ribbons are located on either side of the magnetic neutral line (light gray line), and have opposite magnetic polarities to each other. These are marked N (for positive magnetic polarity) and S (for negative magnetic polarity), respectively. The ribbons expand outward at a speed of v_f in a direction perpendicular to the magnetic neutral line due to the magnetic reconnection which successively occurs in the corona with a speed of v_{in}.

Based on the reconnection models, the energy release rate can be written as the product of the Poynting flux into the reconnection region S $(= (4\pi)^{-1}B_c^2 v_i)$ and the area of the reconnection region A (e.g. Isobe et
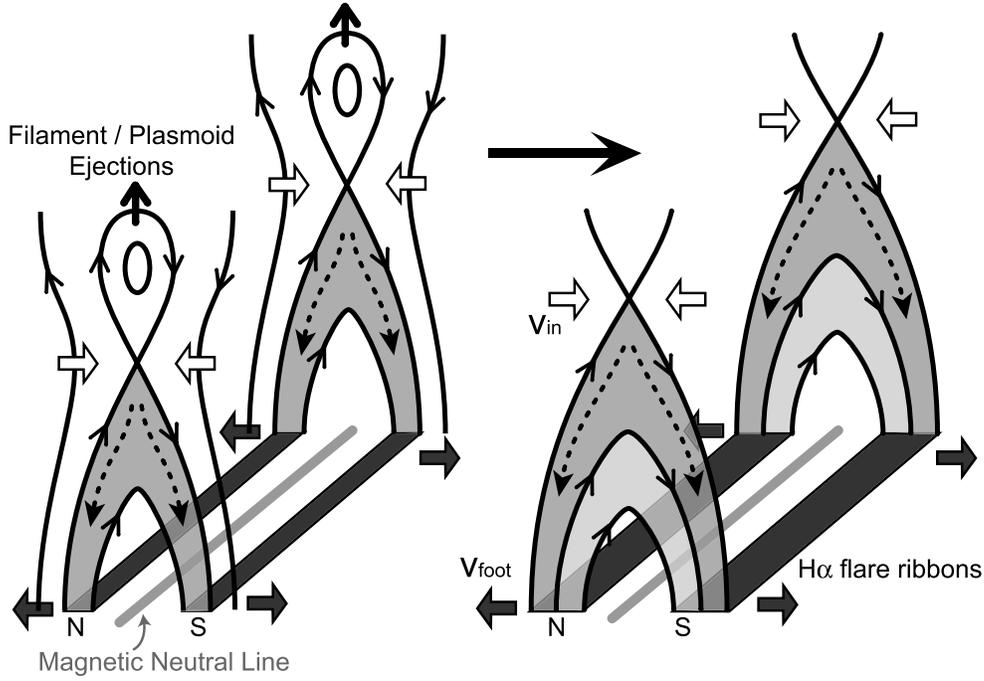
Figure 4.1: Cartoon of magnetic reconnection. Solid lines show the magnetic field lines. N and S show the magnetic polarities. Reconnected magnetic field lines form post-flare loops with a cusp shaped structure (gray regions). Along the reconnected loops, nonthermal particles and thermal conduction propagate from the reconnection site to the footpoints (dashed arrows). As they precipitate into the chromosphere the Hα flare ribbons are generated at the footpoints (dark gray region). They are located on either side of the magnetic neutral line (light gray line), and have opposite magnetic polarities to each other.

al. 2002) as follows;

$$\frac{dE}{dt} = SA = 2\frac{B_c^2}{4\pi}v_i A, \tag{4.1}$$

where B_c is the magnetic field strength in the corona and v_i is the inflow velocity into the reconnection region.

It is very difficult to measure the coronal magnetic field strength directly, so we often estimate it from the photospheric magnetic field by assuming that it is a potential field or a force free field. It is also difficult to measure the inflow velocity, and so far the case reported by Yokoyama et al. (2001) is the only direct observation. Consequently, an indirect method is needed to evaluate the energy release rate quantitatively by using observable values. Forbes

& Lin (2000), Fletcher & Hudson (2001), and Qiu et al. (2002) performed indirect estimates of the released magnetic energy by using observable features. In this chapter, we examine the relation between the expanding motions of the Hα flare ribbons and the magnetic energy released during a flare, which was observed on 2001 April 10. We estimate the released magnetic energy by using the magnetic field strengths at the photospheric level (B_p) and the separation speed of the flare ribbons (v_f), instead of direct coronal values such as B_c and v_i.

Hard X-ray (HXR) and microwave bursts appear when strong energy releases occur, and the sites of the radiation sources indicate where the energy is released. The HXR intensity emitted in bremsstrahlung is correlated with the number of accelerated electrons, and is thought to be proportional to the energy release rate (e.g. Hudson 1991; Wu et al. 1986). The nonthermal microwave synchrotron emission is also thought to be well correlated with the energy release rate (Neupert 1968). We assumed that the HXR intensity and the microwave intensity are proportional to the energy release rate dE/dt, and we constructed light curves for comparison with the estimated magnetic energy.

In §4.2 we summarize the observational data and the features of the flare. In §4.3 we examine when and where strong energy releases occur during the flare. We measured and compared the photospheric magnetic field strengths B_p at each Hα kernel with and without the HXR sources. We also measured the separation speeds of the fronts of the Hα flare ribbons v_f, and compared them with the nonthermal light curves taken in HXRs and microwaves. In §4.4 we derived the amount of energy released at each radiation source by using the B_p and v_f, based on the magnetic reconnection model (eq. 4.1). We also compared the temporal evolution of the estimated energy release rates with the light curve of the HXR total intensity. In §4.5 a summary and our conclusions are given.

4.2   Observations

We observed a large two-ribbon flare (X2.3 on the *GOES* scale), which occurred in the NOAA Active Region 9415 (S22°, W01°) at 05:10 UT, 2001 April 10 with the Sartorius Refractor Telescope (Sartorius) at Kwasan Observatory, Kyoto University (Asai et al. 2002, 2003).

The Hα monochromatic images of the flare were obtained, with a Halle Lyot filter with a 0.5 Å bandwidth in the Hα line center, and the Kodak 1.6i Megaplus CCD Camera. The pixel size of the CCD is 9 μm and corresponds to about 0″6. The highest temporal and spatial resolutions of the Sartorius
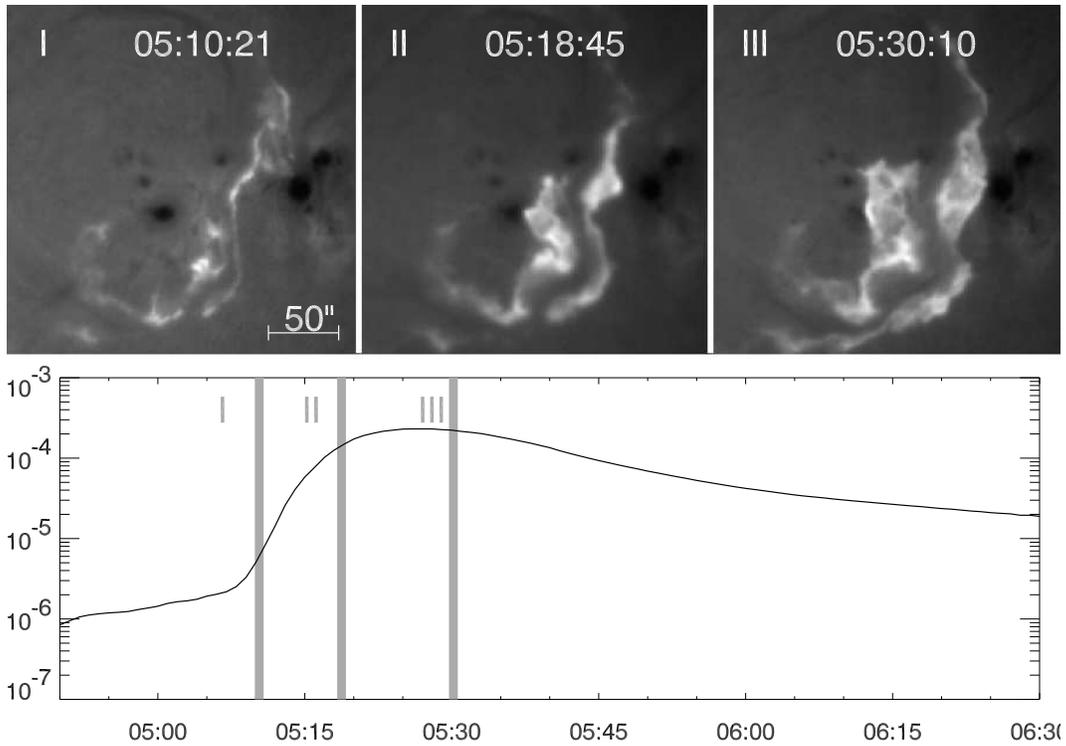
Figure 4.2: Temporal evolution of the 2001 April 10 flare. The top panels (I to III) show Hα images obtained with Sartorius. Celestial north is up, and west is to the right. The bottom panel shows the SXR flux in the *GOES* 1.0 - 8.0 Å channel. The times of the *vertical gray* lines, which are numbered from I to III, correspond to those of the Hα snapshots in the top panels.

Hα data are about 1 s and 1″, respectively. Figure 4.2 shows the temporal evolution of the flare in Hα observed with Sartorius (top panels) and the soft X-ray (SXR) flux obtained with *GOES* (1.0 - 8.0 Å channel, bottom panel). The flare was a long duration event, and showed a typical two-ribbon structure. The *left* (east) flare ribbon is of positive magnetic polarity, and the *right* (west) one is of negative polarity. Foley et al. (2001) and Pike & Mason (2002) reported a filament eruption and a halo coronal mass ejection which were associated with this flare. These authors discussed the acceleration mechanisms of the ejection. In this chapter we discuss in detail the evolution of the Hα flare ribbons.

To examine the locations of the HXR radiation sources where strong energy releases occur, and to compare the temporal variations of the estimated energy release rates with the light curve of the HXR total intensity, we used
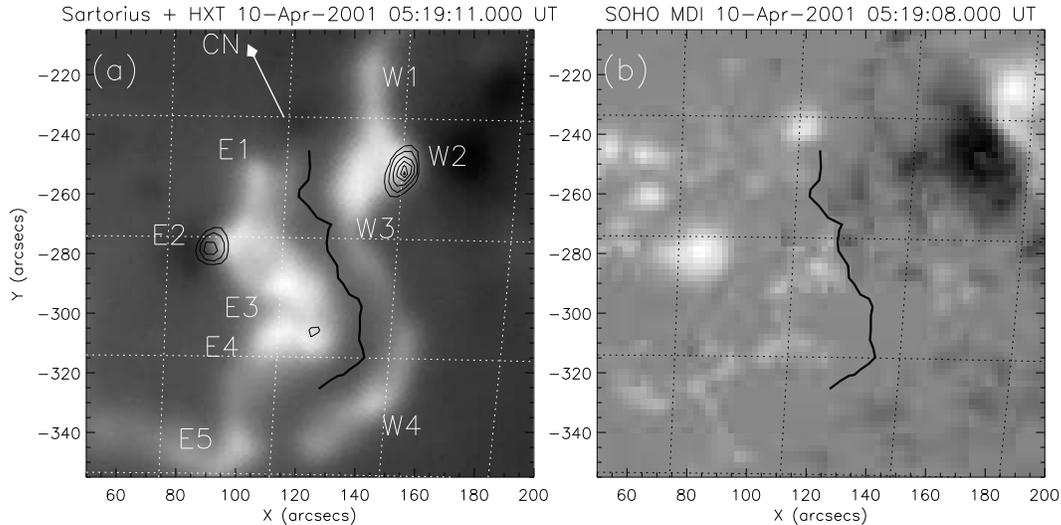
Figure 4.3: Comparison between the spatial distribution of the Hα kernels and that of the HXR sources. The horizontal and vertical axes show the distance from the disk center in arcseconds. Solar north is up, and west is to the right. (a). An Hα image taken with Sartorius at 05:19 UT. In the image nine Hα bright kernels numbered from E1 to E5 and from W1 to W4 are seen. The HXR contour image overlaid on the Hα image was obtained by *Yohkoh*/HXT (H band, 53 - 93 keV). Contour levels are 95%, 80%, 60%, 40%, 20% and 10% of the peak intensity. (b). A photospheric longitudinal magnetogram obtained by *SOHO*/MDI at 05:19 UT. Black solid lines show the position of the magnetic neutral line, and a white arrow, marked with CN, points the direction of celestial north at that time.

HXR data taken with the hard X-ray telescope (HXT; Kosugi et al. 1991) aboard *Yohkoh* (Ogawara et al. 1991). The temporal and spatial resolutions of the HXT data are 0.5 s and 5″, respectively. Figure 4.3a shows a comparison between the spatial distribution of the HXR sources and that of the Hα kernels. The HXR contour image taken with HXT is overlaid on an Hα image obtained at 05:19 UT with Sartorius. To examine the nonthermal behavior of the flare, we also used microwave time profiles obtained with the Nobeyama Radioheliograph (NoRH; Nakajima et al. 1994). The NoRH microwave data were obtained at 17 GHz with a temporal resolution of 1.0 s. Figure 4.4 shows the light curves in microwaves, SXR, and HXR. The top line is that of the HXT H band (53 - 93 keV), the middle one is NoRH 17 GHz, and the bottom one is the *GOES* 1.0 - 8.0 Å channel. Both of the HXT and NoRH light curves show some bursts. The dawn of *Yohkoh* was

at 05:19 UT, and the earlier part of the flare was missed because of night. No large NoRH bursts are seen from 05:20 to 05:31 UT, since the emission mechanism becomes optically-thick during the time range, while the other bursts are from optically-thin gyrosynchrotron radiation.

We used a magnetogram obtained at 05:19 UT with the Michelson Doppler Imager (MDI; Scherrer et al. 1995) aboard the *Solar and Heliospheric Observatory* (*SOHO*; Domingo, Fleck, and Poland 1995) to measure photospheric magnetic field strengths. We show the MDI image in Figure 4.3b. The spatial resolution of the MDI image is about $4''$.

We co-aligned the Hα images and the MDI image by our eyes. The accuracy of the co-alignment is about $2''$, which is comparable to the pixel size of the MDI data. For the co-alignment between the HXT and the MDI, we used the informations of position which the satellites themselves have. We checked the accuracy of the co-alignment by using MDI and SXT data, and it is about $2''$, which is also comparable to the pixel size of the MDI data. The errors for the separation velocity of Hα flare ribbons and the photospheric field strength caused by the co-alignment are approximately 10 km s^{-1} and 30 G, respectively.

4.3 Evolution of Flare Ribbons and Energy Release

4.3.1 Places Where Strong Energy Releases Occur

First, we examined the relation between the photospheric magnetic field strength at each Hα kernel and the energy release. It has been reported that the locations of HXR sources are associated with the locations of Hα kernels (Kurokawa, Takakura, & Ohki 1988; Kitahara & Kurokawa 1990; Sakao 1994). This is because both radiation sources are caused by the precipitation of nonthermal electrons into the chromosphere. On the other hand, differences between the locations of these two radiation sources have also been known. While many Hα kernels are found to brighten successively during the evolution of the flare ribbons, only a few radiation sources are seen in the HXR images (see Fig. 4.3a). This is a feature which has been noted in many other flares. Since the mechanisms for Hα radiation are much more complicated than those for HXR radiation (Ricchiazzi & Canfield 1983; Canfield, Gunkler, & Ricchiazzi 1984), it is possible that some weaker Hα kernels are caused by some effects other than the precipitation of nonthermal particles, for example, thermal conduction. We suggested in a previous paper Asai et al. (2002) that the difference between the spatial distributions of Hα kernels
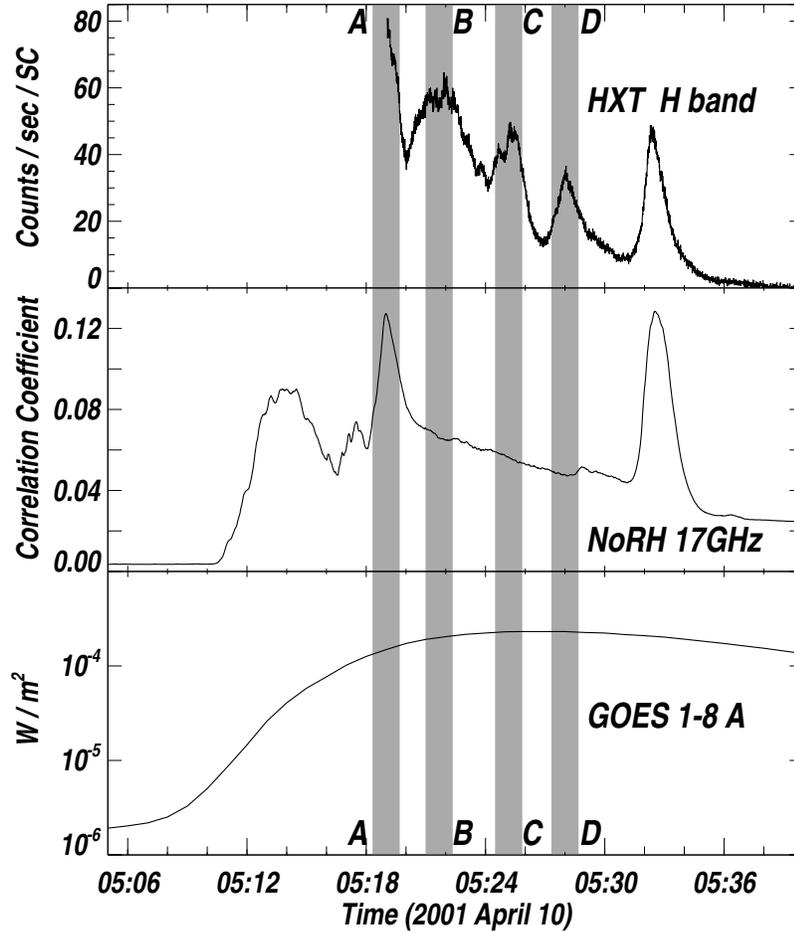
Figure 4.4: Temporal evolution of the 2001 April 10 flare. From top to bottom: hard X-ray count rate measured in the H band (53 - 93 keV) of *Yohkoh*/HXT; radio correlation plot observed at 17 GHz with NoRH; SXR flux in the GOES 1.0 - 8.0 Å channel. Four *light gray* vertical lines numbered A to D show the peak times of the HXR bursts.

and HXR sources is caused by the low dynamic range of the HXR data. For example, HXT has a dynamic range of about 10. In the HXR images only the strongest sources are seen, and the weaker sources are buried in the noise.

We measured the magnetic field strength at the location of each Hα kernel along the outer edges of the flare ribbons (Fig. 4.3). The Hα kernels accompanied by HXR radiation (E2 and W2) have magnetic field strengths about 3 times larger than those without HXR radiation (Table 3.1). We have also estimated energy release rates based on the magnetic reconnection model. Eq. 4.1 shows the relation, $dE/dt \propto B_c^2 v_i$. As some authors have suggested, v_i may have some dependence on B. For example, with the Sweet-Parker model (Sweet 1958; Parker 1957), $v_i \propto B^{1/2}$ and thus $dE/dt \propto B^{5/2}$. On the other hand, with the Petschek model (Petchek 1964), which indicates the relation $v_i \propto B$, we have $dE/dt \propto B^3$. Since B at the HXR sources is 3 times larger, both models of magnetic reconnection predict much larger energy release, for the Hα sources accompanied by HXR sources than for the other Hα kernels 16 or 27 times stronger, respectively. These values are larger than the dynamic range of HXT, so the difference between the spatial distributions of the Hα kernels and the HXR sources can in principle be explained.

4.3.2 Timings When Strong Energy Releases Occur

Next, we examined the relation between the separation speeds of the Hα flare ribbons and the energy releases. Successive reconnection produces the outward motions of the flare ribbons. Thus, some authors have suggested that the separation speed of the flare ribbons is related to the amount of energy release, and hence, the released magnetic energy due to magnetic reconnection (e.g. Fletcher & Hudson 2001). In order to examine this suggestion in more detail, we compared the separation speeds of the flare ribbons with the timing and locations of the HXR sources.

In Figure 4.4 we can identify three main bursts in the microwave emission. Five bursts are seen, in HXR emission, though the first microwave burst is completely missed because *Yohkoh* was in the shadow of the Earth (*Yohkoh*'s night). Here, we investigate the HXR bursts which occurred at the times emphasized by the *light gray* vertical lines. We examined the relation between the separation speeds of the Hα flare ribbons at the HXR sources and the timing of the bursts. The HXR sources appeared as local compact points along the Hα flare ribbons and the sites are different for each HXR burst. Figure 4.5 shows the positions of the HXR sources at the time of each HXR burst. The labels from A to D, correspond to the times of the HXR bursts shown in Figure 4.4. Here, we concentrate on the evolution of the east (*left*) flare ribbon, since it is more obvious and less complicated than the west
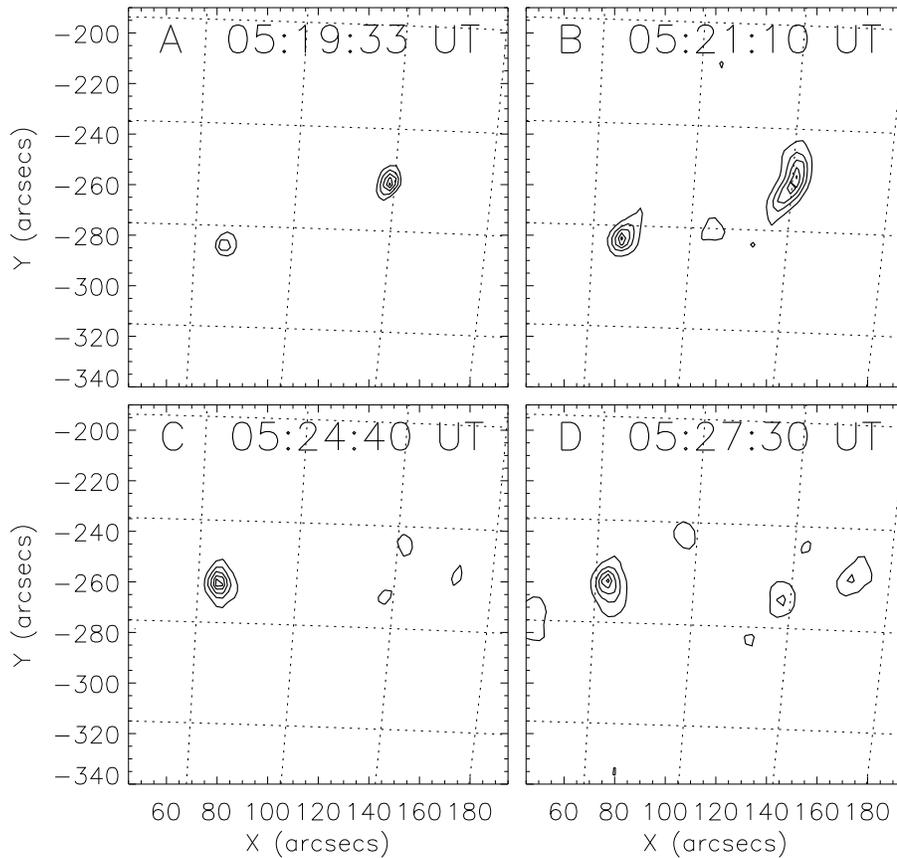
Figure 4.5: HXR contour images of each HXR burst taken with *Yohkoh*/HXT (H band, 53 - 93 keV). Contour levels are 95%, 80%, 60%, 40% and 20% of the peak intensity.

(*right*) one. In the left panels of Figure 4.6 the position of the HXR source in the east ribbon at the time of each HXR burst is marked with a cross (×). The time of each Hα image, named A to D, corresponds to that of the vertical lines in Figure 4.4. In Figures 4.5 and 4.6, the positions of the HXR east sources, at the time of burst A, correspond to the position of the Hα kernel named "E2" in Figure 4.3.

Although the evolution of the Hα flare ribbons is spatially and temporally complicated, roughly speaking, they separate from each other in the east-west direction, since the magnetic neutral line lies approximately in the north-south direction (see Fig. 4.3b). In the left panels of Figure 4.6 *white* slit lines denoted SA to SD have been placed on the Hα images. They are
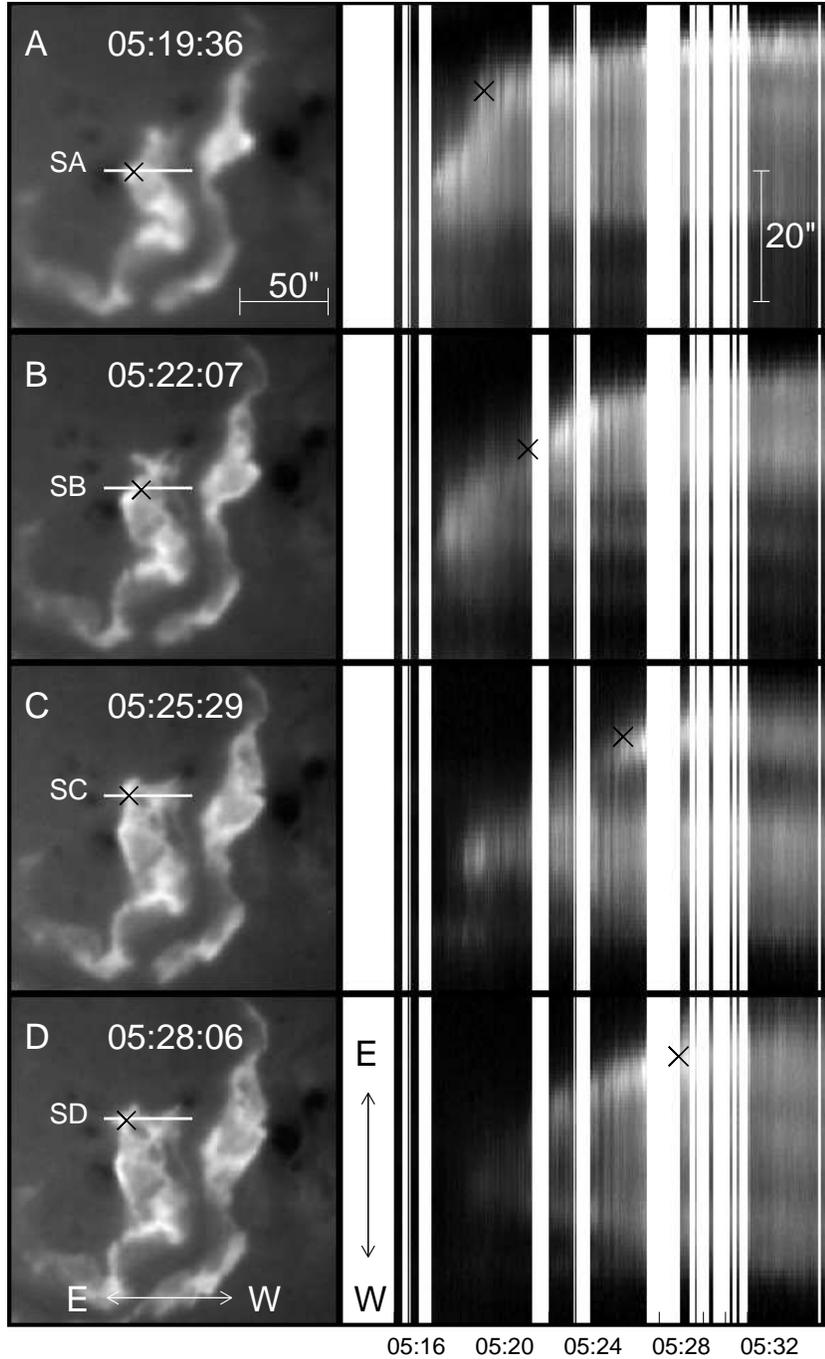
Figure 4.6: Sites of the HXR sources at the times of each HXR burst and flare ribbon separations along slits which placed on the HXR sources. *Left*: Hα images obtained with *Sartorius* at the times of each HXR burst. A to D are the same as in Figure 4.4. Celestial north is up, and west is to the right. *Right*: time-sequenced Hα images along the slit lines SA to SD in the left panels. The horizontal axis is time, and the vertical axis is the distance along the slit.

positioned on the east (*left*) Hα flare ribbon in the east-west (horizontal) direction so that each are passes through the corresponding HXR source. Following the temporal expansion of the Hα ribbon, we tracked the positions of the outer edges of the ribbons along the "slit lines" and examined the distances between the east flare ribbon and the magnetic neutral line. The right panels are time-sequenced Hα images through the slits of the left panels. The vertical axis shows the space along the slits, and celestial east is up. The horizontal axis is time. Upward expansion of the bright belts shows the increasing separation of the front of the flare ribbon from the magnetic neutral line in each image. Again, the cross ($\times$) shows the position and time of the HXR sources corresponding to that of the left panel. The HXR bursts tend to appear when the separation speeds of the flare ribbons reduce. Figure 4.7 also shows comparisons between the separation speeds of the flare ribbons and the timing of the HXR bursts. Here, the separation speeds are determined by using the temporal variation of the position of the ribbon-front in the east-west direction.

It is reasonable to think that the faster the Hα flare ribbons separate from each other, the larger the magnetic flux participating in the magnetic reconnection, and hence, the larger the magnetic energy release. The tendency that the HXR sources appear when the separation speed decreases seems to be inconsistent with this supposition. However, it is also known that the separation of flare ribbons decelerates or even stops in strong magnetic field regions (e.g. Kitahara & Kurokawa 1990). It is possible that more magnetic flux participates in reconnection even when the separation of the flare ribbons decelerates near sunspot umbrae. Therefore, it is necessary to examine the energy release rate taking both the separation speed and magnetic field strength into account, simultaneously. We discuss this in the next section.

4.4 Energy Release Rate

We now estimate the amount of energy released via magnetic reconnection during the flare. The energy release rate, i.e. the released energy per unit time, is written as equation (4.1). Here, we assume that the area of the reconnection region (A) does not change significantly during the flare and is independent of the magnetic field strength. Therefore, the energy release rate is simply proportional to the Poynting flux S ($= 2(4\pi)^{-1}B_c^2 v_i$). Before the estimation, we determined the temporal variation of the photospheric magnetic field strengths (B_p). We followed the positions of the outer edges of the ribbons along the slit lines, in the same manner as for the measurement of v_f shown in §4.3.2, and we measured B_p there at each time. We

are able to measure the B_p at the sites where the newest energy release occurred with this method, even though we did not use a temporal series of the magnetic field data. Some authors have reported rapid changes of the photospheric magnetic field in the vicinity of a neutral magnetic line during flares (Kosovichev & Zharkova 2001; Wang et al. 2002). In Figure 4.7 we show the temporal variation of B_p.

We estimated the reconnection rate ($\dot{\Phi}$), i.e. the electric field strength in the corona, by using B_p and v_f. The reconnection rate is one of the most important physical values in reconnection physics, because it shows how violently magnetic reconnection progresses. It is defined as the reconnected magnetic flux per unit time, and expressed as follows (Isobe et al. 2002)

$$\dot{\Phi} = B_c v_i. \tag{4.2}$$

From the conservation of magnetic flux, we can write

$$\dot{\Phi} = B_p v_f. \tag{4.3}$$

Strictly speaking, the separation of the Hα flare ribbons is a chromospheric phenomenon, and therefore, we should calculate the reconnection rate by using the chromospheric magnetic field strength (B_{ch}) instead of B_p. As Leka & Metcalf (2003) reported, magnetic field strength in an active region generally decreases with height, and B_{ch} shows a correlation with B_p. However, they also reported that the relation between B_p and B_{ch} becomes somewhat complex in some regions, such as penumbra and plage. In this chapter, we do not consider the difference and calculate the reconnection rate simply by using B_p.

We also estimated the Poynting flux by using B_p and v_f instead of B_c and v_i, which are difficult to measure. The total Poynting flux carried into the reconnection region is rewritten as

$$S = \frac{1}{2\pi} B_c B_p v_f, \tag{4.4}$$

with the above assumption. The released energy is approximately equal in the upward and downward directions at the reconnection point, and the downward amount is additionally divided among the footpoints. Therefore, the amount which arrives at one footpoint is reduced by a factor ϵ ($0 \leq \epsilon \lesssim 1/2$) such that

$$S = \frac{\epsilon}{2\pi} B_c B_p v_f. \tag{4.5}$$

We assume that the factor ϵ has almost the same value everywhere. Furthermore, we assume that B_c is proportional to B_p in the same ratio all over the
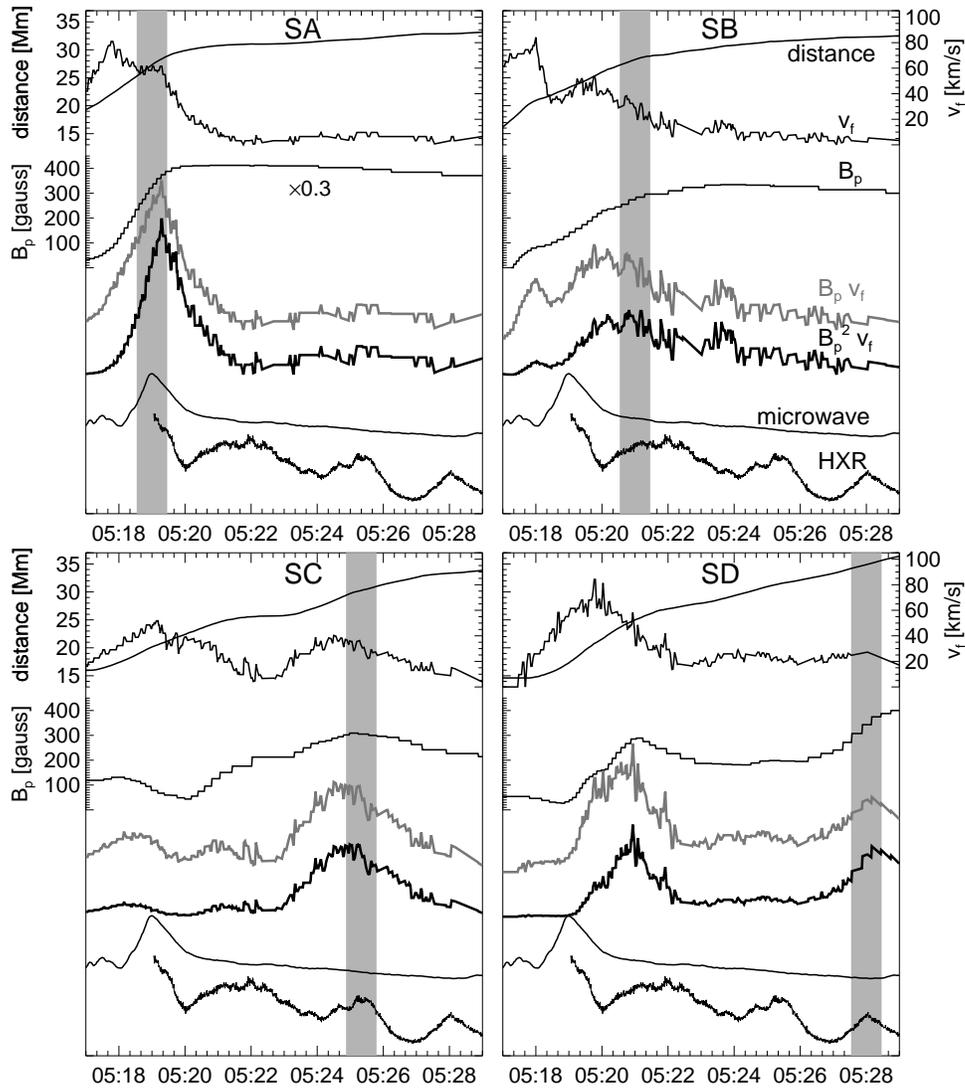
Figure 4.7: Temporal variations of the physical parameters measured along each slit line (from SA to SD) shown in Figure 4.6 for the eastern ribbon. From top to bottom: distance between the outer edge of the ribbon and the magnetic neutral line (NL); separation speed of the ribbon (v_f) from the NL; photospheric magnetic field strength (B_p) at the outer edge of the ribbon; estimated reconnection rate, $B_p v_f$ (*gray lines*; scaled arbitrarily); estimated Poynting flux, $B_p^2 v_f$ (scaled arbitrarily); microwave correlation plot in 17 GHz obtained with NoRH; hard X-ray count rate measured in the *Yohkoh*/HXT H band (53 - 93 keV). v_f was determined as the time derivative of the distance of the flare ribbons. B_p measured along SA is plotted with multiplied by 0.3. The enhancements of the estimated reconnection rates and the Poynting fluxes, which are accompanied by the HXR bursts, can be seen.
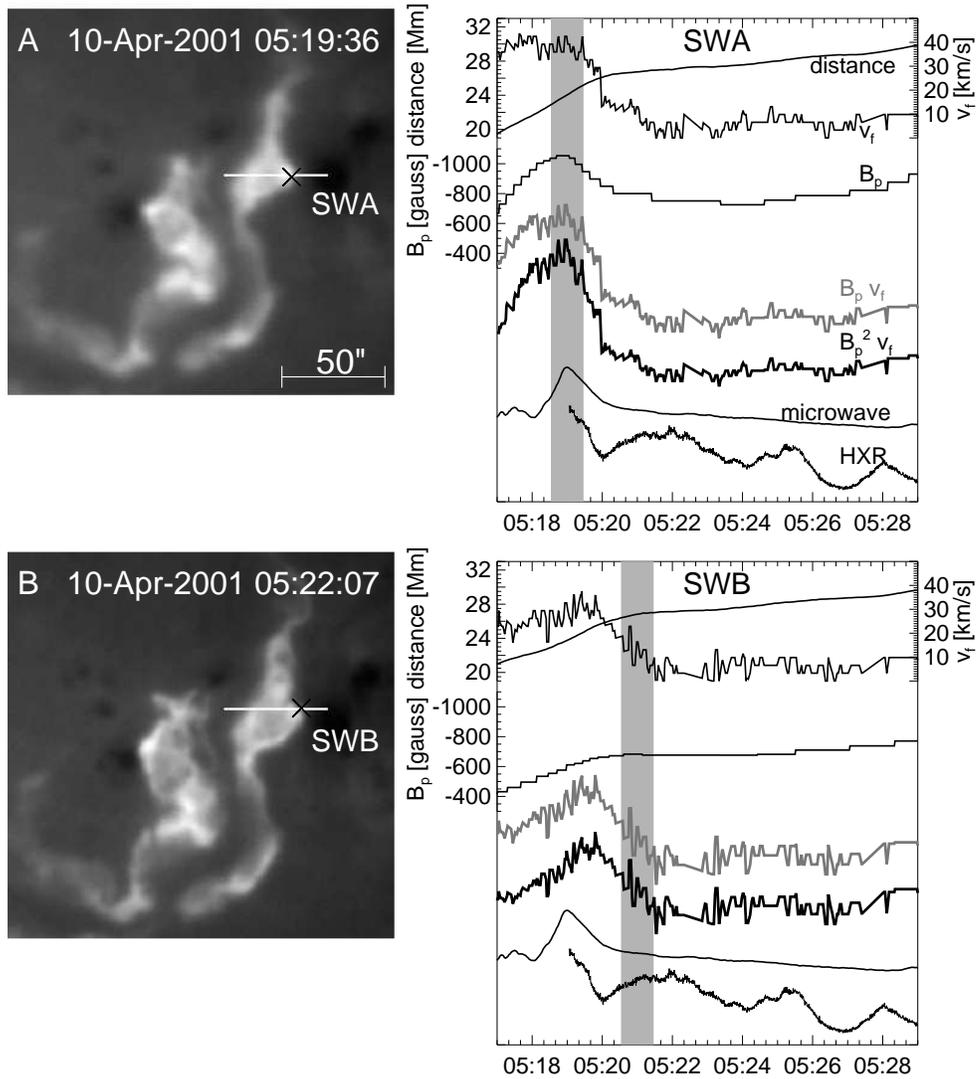
Figure 4.8: The west (*right*) flare ribbon. *Left*: Hα images at the time of the HXR bursts A and B (see Fig. 4.4). *Right*: temporal variations of the physical parameters measured along the slit lines SWA and SWB in the left panels. From top to bottom: distance; v_f; B_p; $B_p v_f$ (*gray lines*; scaled arbitrarily); $B_p^2 v_f$ (scaled arbitrarily); microwave correlation plot in 17 GHz obtained with NoRH; hard X-ray count rate measured in the *Yohkoh*/HXT H band (53 - 93 keV). The quantities are measured in the same way as those in Figure 4.7.

flaring region, i.e. $B_c = aB_p$ (a = const.), and that the Poynting flux can be expressed as

$$S = \frac{\epsilon a}{2\pi} B_p^2 v_f. \tag{4.6}$$

Although the assumption may be simplistic, it is reasonable, provided we do not discuss the energy release rates of the whole active region. This is because the B_c-to-B_p-ratio remains approximately constant in narrow regions. According to a potential field calculation, which is extrapolated by using the software package MAGPACK2 (Sakurai 1982), a ($= B_c/B_p$) is about 0.2, and tends to be smaller at the points with stronger magnetic field strength. Therefore, we assume $\epsilon a = 1/10$ for an order of magnitude estimation here, and calculate

$$S = \frac{1}{20\pi} B_p^2 v_f \tag{4.7}$$

as the Poynting flux released at the source.

Here, we defined v_f as the speed of the flare-ribbon separation, relative to the magnetic neutral line, in the perpendicular direction. This assumption is based on the 2-D view of the magnetic reconnection model. We discuss the assumption in the next section. Moreover, the magnetic neutral line lies almost in the north-south direction (see Fig. 4.3b), as mentioned in the previous section. We estimated the reconnection rate (eq. 4.3) and Poynting flux (eq. 4.7) along the slit line. Then, we compared these with the light curves in HXRs and microwaves which are assumed to be proportional to the energy release rate dE/dt due to magnetic reconnection. Figure 4.7 shows the estimated reconnection rates and Poynting fluxes compared with the light curves in HXR and microwaves which were obtained with HXT and NoRH. The temporal evolutions of the other physical values, such as the photospheric magnetic field strength B_p, the distance of the front of the flare ribbons from the magnetic neutral line, and the separation speed of the flare ribbons from the magnetic neutral line v_f, are also given. The evolutions of the reconnection rates and Poynting fluxes appear to match the HXR and microwave light curves well (see vertical light gray lines in Fig. 4.7). We also made a similar estimate for the west (*right*) flare ribbon. Figure 4.8 shows the positions of the slit lines (SWA and SWB) on the HXR sources at the times of bursts A and B, and the estimated physical parameters along the slits. For the HXR bursts C and D, we did not estimate the parameters, since the positions of the HXR sources are ambiguous (see Fig. 4.5). We again successfully reconstructed the enhancements in both the reconnection rate and the Poynting flux for the HXR burst A but not for burst B. This is because the evolution of the west flare ribbon is more complex than the east one, as mentioned earlier, and the location of the HXR sources at the time of

burst B is positioned close to that of the burst A. In addition, the amount of released energy is probably smaller there than that released at the burst A, and therefore, the enhancements for burst B did not appear as clear peaks.

Are the estimated energy release rates at the Hα kernels associated with the HXR bursts large enough to explain the difference between the spatial distribution of the HXR sources and that of the Hα kernels? To answer the question, we compared them with those at the Hα kernels without HXR bursts, e.g. E1 and E3 in Figure 4.3, at the time of the first HXR burst (05:19UT). Figure 4.9 shows the comparison between the estimated energy release rates at the Hα kernels associated "with" HXR sources (E2 in Fig. 4.3) and those at the other Hα kernels "without" the HXR sources (E1 and E3 in Fig. 4.3). These curves of the reconnection rates and the Poynting fluxes for E1 and E3 are plotted but multiplied by factors of 3 and 10, respectively. We investigated the behaviors during the time range enclosed by the two vertical dotted lines in Figure 4.9. We found that the reconnection rate of E2 is at least 16 times stronger than that of the other two kernels. The Poynting flux at E2 is also much more enhanced, and is 150 times stronger than that of the others. The results are summarized in Table 4.1. Both the estimated reconnection rates and Poynting fluxes are large enough locally at the HXR sources. The results can explain the difference between the spatial distribution of the HXR sources and that of the Hα kernels. In this chapter we assume that the B_c-to-B_p-ratio a is the same value for all the Hα kernels, E1, E2, and E3. However, the value a tends to be smaller for the sources with stronger magnetic field strength, and smaller again for E2 than for the other sources, since it is located much closer to the large umbra. Nevertheless, the calculated Poynting flux at E2 is as large as 150 times that of the other sources, so we can still conclude that the released energy at E2 is large enough to overcome the dynamic range, even if this tendency is taken into account. Here, we perform an order of magnitude estimation for the energy budget of an HXR source. The photon spectral index, which was derived from the ratio of photon counts of M2/H bands, is about -3. If we adopt the thick target model (Brown 1971), and assume that the low energy cut-off is 20 keV, then, the total energy of electrons that produced HXR burst at the source E2 during 05:19 - 05:20 UT is estimated as 6×10^{29} erg. In our analysis, the derived energy release rate (Poynting flux) for the Hα kernel E2 is about 1×10^{11} erg cm^{-2} s^{-1}, and this lasts for about 1 minute (see Fig. 4.9 and Table 4.1). The area of E2 is about 10^{18} cm^2. Then, the released energy is estimated as 6×10^{30} erg. So, the estimated released energy is large enough to generate the HXR source.
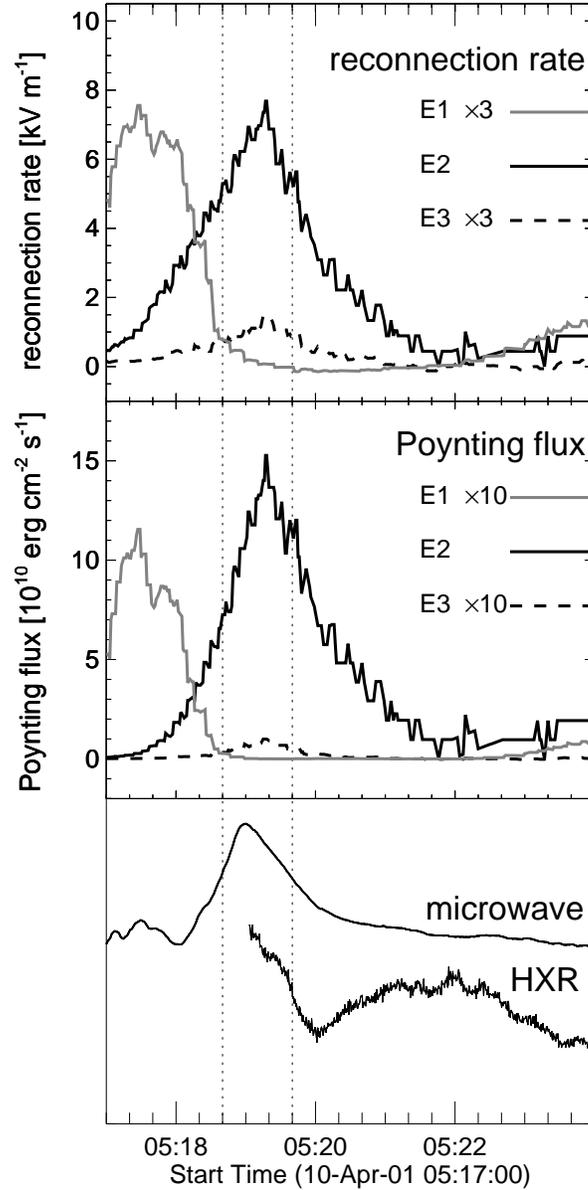
Figure 4.9: Comparison between the estimated energy release rates of the Hα kernels associated with the HXR sources (E2) and those without HXR sources (E1 and E3). Each Hα kernel is shown in Figure 4.2. In the top two panels the curves for E1, E2, and E3 are plotted with gray lines, solid lines, and dashed lines, respectively. Top panel shows the time variations of the reconnection rate ($B_p v_f$). Those for E1 and E3 are plotted with multiplied by 3. Middle panel shows the time variations of the Poynting flux ($B_p^2 v_f$). Those for E1 and E3 are plotted with multiplied by 10. Bottom panel shows the microwave correlation plot in 17 GHz and the hard X-ray count rate obtained with the NoRH and *Yohkoh*/HXT H band, respectively.

Table 4.1: Reconnection rates and Poynting fluxes at Hα kernels

Hα kernel	reconnection rate $\dot{\Phi}$ (ratio) [V m^{-1}]	Poynting flux S (ratio) [erg cm^{-2} s^{-1}]
E1	2.6×10^2 (0.52)	2.7×10^8 (0.27)
E2	7.7×10^3 (16)	1.5×10^{11} (150)
E3	4.9×10^2 (1.0)	1.0×10^9 (1.0)

Note: Each ratio (parenthesis) of the reccontion rate and the Poynting flux has been normalized by using the value of E3.

4.5 Summary and Conclusions

We examined the relation between the evolution of the Hα flare ribbons and the released magnetic energy during a solar flare which occurred on 2001 April 10. We measured the photospheric magnetic field strength of each Hα kernel, and found that the magnetic field strengths of the Hα kernels associated with HXR sources were about 3 times larger than those at the other Hα kernels without HXR sources. We also measured the separation speed of the Hα flare ribbons from the magnetic neutral line. The separation speed reduces when the HXR bursts occur at the site of the HXR sources. We also estimated the energy release rate, based on the magnetic reconnection model, by using the photospheric magnetic field strength and the separation speed of the Hα flare ribbons. We calculated $B_p v_f$ and $(4\pi)^{-1} B_p^2 v_f$, as the reconnection rate ($\dot{\Phi}$) and the Poynting flux (S), respectively. Both $\dot{\Phi}$ and S of the HXR sources are much stronger than those of the Hα kernels without HXR sources. The estimated energy release rates of the Hα kernels associated with the HXR sources are locally large enough to explain the difference between the spatial distribution of the Hα kernels and the HXR sources. The temporal evolution of the energy release rates also shows peaks corresponding to the HXR bursts.

In this paper we applied 2-D reconnection model to the flare which shows really 3-D structure, and estimated the energy release rate in such 2-D view. In this approach, v_f should be defined as the separation speed of the Hα flare ribbons in the "perpendicular" direction to the neutral line as we performed. So, if the formation of the flare ribbons (and post-flare loops) proceeds in the "parallel" direction to the neutral line, that effect is ignored. On the other hand, there is another approach, to follow Hα kernels or HXR sources, to estimate energy release rate during a flare. For example, Qiu et al. (2002) measured the reconnection rate $B_p v_f$ and compared it with HXR light curves, as they defined v_f as the temporal evolution of the sites of the "brightest Hα kernels". However, the motion of the flare kernels does not
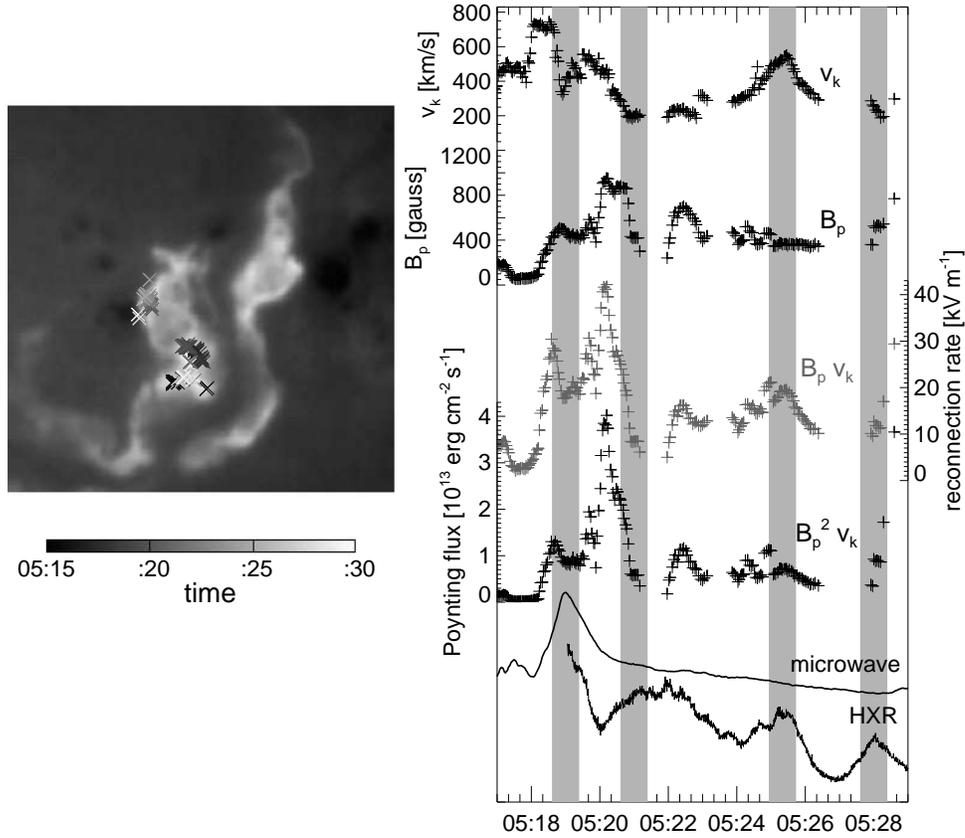
Figure 4.10: Evolution of the Hα kernels in the east ribbon. *Left*: cross signs (×) show the positions of maximum intensity in each time. Color shows the time indicated below the panel. *Right*: time profiles about the evolution of Hα kernels. From top to bottom: velocity (v_k), photospheric magnetic field strength (B_p), reconnection rate ($B_p v_k$), and Poynting flux ($B_p^2 v_k$). Four *light gray* vertical lines are the same as those in Figure 4.4.

necessarily represent the speed of reconnection, because kernel motion might follow the successive occurrence of impulsive reconnection point "along" the X-line in 3-D space. Bright flare kernels appear, at the times when strong energy releases occur, and at the sites where strong energy releases occur. In Figure 4.10 we showed the evolution of the Hα kernels, and results of the estimation of the energy release rate by following the motion of the Hα kernels. Hα kernels also appear sometimes continuously, and sometimes jump to the remote points, which makes the speed of the kernel motion v_k larger. The obtained time profile of $B_p v_k$ and $B_p^2 v_k$ is quite different from that of nonthermal emissions. This is probably because these kernel motions do not correspond to the progress of energy release, and magnetic reconnection. We also estimated the energy release by using the motion of the Hα kernels. In this case, the energy release rate (Poynting flux) for the Hα kernel E2 is about 2×10^{13} erg cm^{-2} s^{-1}. Then, the released energy is estimated as 1.2×10^{33} erg, which is much larger than the enegy which generates the HXR source in thick target model. To understand completely the whole 3-D structure of the flare is difficult task at present, and beyond the scope of the paper. Both these approaches have merits and demerits, and we chose the former approach in this paper. Although our 2-D approach contains quite simplified assumption, the obtained results are well consistent with the observed features, both qualitatively and quantitatively.

In this chapter we also estimated the energy release rate by assuming that B_c is proportional to B_p with a constant ratio. Despite these assumptions, we were able to reconstruct well the behavior of the impulsive energy release seen in the microwave and HXR light curves. These assumptions, however, are reasonable only within a narrow region, and more detailed analyses are needed to extend our discussion to the whole flare region. We will discuss this topic in future papers.

Bibliography

Asai, A., Masuda, S., Yokoyama, T., Shimojo, M., Isobe, H., Kurokawa, H., and Shibata, K. 2002, ApJ, 578, L91

Asai, A., Ishii, T. T., Kurokawa, H., Yokoyama, T., and Shimojo, M. 2003, ApJ, 586, 624

Brown, J. C. 1971, Sol. Phys., 18, 489

Canfield, R. C., Gunkler, T. A., and Ricchiazzi, P. J. 1984, ApJ, 282, 296

Carmichael, H. 1964, in The Physics of Solar Flares, ed. W. N. Hess (NASA SP-50), 450

Domingo, V., Fleck, B., Poland, A. I. 1995, Sol. Phys., 162, 1

Fletcher, L., Hudson, H. 2001, Sol. Phys., 204, 71

Foley, C. R., Harra, L. K., Culhane, J. L., and Mason, K. O. 2001, ApJ, 560, L91

Forbes, T. G., and Lin, J. 2000, J. Atmos. Sol-Terr. Phys., 62., 1499

Hirayama, T. 1974, Sol. Phys., 34, 323

Hudson, H. S. 1991, Sol. Phys., 133, 357

Isobe, H., Yokoyama, T., Shimojo, M., Morimoto, T., Kozu, H., Eto, S., Narukage, N., and Shibata, K. 2002, ApJ, 566, 528

Kitahara, T. & Kurokawa, H. 1990, Sol. Phys., 125, 321

Kopp, R. A., & Pneuman, G. W. 1976, Sol. Phys., 50, 85

Kosovichev, A. G., Zharkova, V. V. 2001, ApJ, 550, L105

Kosugi, T., et al. 1991, Sol. Phys., 136, 17

Kurokawa, H., Takakura, T., Ohki, K. 1988, PASJ, 40, 357

Leka, K. D., Metcalf, T. R. 2003, Sol. Phys., 212, 361

Moore, R. L., Sterling, A. C., Hudson, H. S., Lemen, J. M. 2001, ApJ, 552, 833

Moore, R. L., Roumeliotis, G. 1992, in IAU Colloq. 133, Eruptive Solar Flares, ed., Z. Svestka, B. V. Jackson, & M. E. Machado (New York: Springer), 69

Nakajima, H., et al. 1994, in Proc. of the IEEE, 82, 705

Neupert, W. M. 1968, ApJ, 153, L59

Ogawara, Y., Takano, T., Kato, T., Kosugi, T., Tsuneta, S., Watanabe, T., Kondo, I., and Uchida, U. 1991, Sol. Phys., 136, 10

Parker, E. N. 1957, J. Geophys. Res., 62, 509

Petschek, H. E. 1964, in AAS-NASA Symp. on Solar Flares, ed. W. N. Hess (NASA SP-50), 425

Pike, C. D., Mason, H. E. 2001, Sol. Phys., 206, 359

Pneuman, G. W. 1981, in Solar Flare Magnetohydrodynamics, ed. E. R. Priest, (New York: Gordon & Breach), 379

Priest, E., Forbes, T., 1990, Sol. Phys., 126, 319

Priest, E., Forbes, T. 2000, Magnetic Reconnection (Cambridge: Cambridge University Press)

Ricchiazzi, P. J., and Canfield, R. C. 1983, ApJ, 272, 739

Qiu, J., Lee, J., Gary, D. E., Wang, H. 2002, ApJ, 565, 1335

Sakao, T. 1994, Ph.D. thesis (University of Tokyo)

Sakurai, T. 1982, Sol. Phys., 76, 301

Scherrer, P. H., et al. 1995, Sol. Phys., 162, 129

Shibata, K. 1999, Ap&SS, 264, 129

Sturrock, P. A. 1966, Nature, 211, 695

Sturrock, P. A. 1992, in Eruptive Solar Flares, eds. Z. Švestka, B. V. Jackson, M. E. Machado (Berlin: Springer), 397

Švestka, Z., Cliver, E. W. 1992, in Eruptive Solar Flares, eds. Z. Švestka, B. V. Jackson, M. E. Machado (Berlin: Springer), 1

Sweet, P. A. 1958, in IAU Symp. 6, Electromagnetic Phenomena in Cosmical Physics, ed. B. Lehnert (Cambridge: Cambridge University Press), 123

Wang, H., Spirock, T. J., Qiu, J., Ji, H., Yurchyshyn, V., Moon, Y. J., Denker, C., Goode, P. R. 2002, ApJ, 576, 497

Wu, S. T., et al. 1986, in Energetic Phenomena on the Sun, ed.s M. Kundu & B. Woodgate (NASA CP-2439), 378

Yokoyama, T. & Shibata, K. 2001, ApJ, 549, 1160

Yokoyama, T., Akita, K., Morimoto, T., Inoue, K., Newmark, J. 2001, ApJ, 546, L69

Chapter 5

Downflow Motions Associated with Impulsive Nonthermal Emissions Observed in the 2002 July 23 Solar Flare[‡]

Recent progress of solar observations has brought us new piece of the evidence of magnetic reconnection in solar flares. In this chapter we present a detailed examination of downflow motions above flare loops observed in the 2002 July 23 flare. The extreme ultraviolet images obtained with the *Transition Region and Coronal Explorer* show dark downflow motions (sunward motions) above the post-flare loops, not only in the decay phase but also in the impulsive and main phases. We also found that the times when the downflow motions start to be seen correspond to the times when bursts of nonthermal emissions in hard X-rays and microwave are emitted. This result implies that the downflow motions occurred when strong magnetic energy was released and that they are, or are correlated with, reconnection outflows.

5.1   Background of This Work

In this thesis we have tried to derive informations about magnetic reconnection, so far. In this chapter we examine another phenomenon, downflow, which was newly found with recent progresses of solar observations, and which is thought to be directly related to magnetic reconnection. The finding of supra-arcade downflow motions (downflows) is one of the most important results which the Soft X-Ray Telescope (SXT; Tsuneta et al. 1991) aboard *Yohkoh* (Ogawara et al. 1991) achieved. McKenzie & Hudson (1999, 2001), and McKenzie (2000) examined, in detail, these dark and sometimes bright features moving sunward from the high corona with speeds of 45 - 500 km s^{-1}. They also performed the temperature analysis with the filter ratio method (Hara et al. 1992), although it is very difficult to extract these physical values for such low emission features owing to instrumental effects like scattering. They reported that density and temperature of the downflows are about 10^9 cm^{-3} and 10^7 K, respectively. Although these values contain considerable uncertainties, they suggested that they are "moving voids" which consist of such low-density and high-temperature plasma. These voids are pushed downward because of magnetic reconnection which occurred at higher altitudes, and therefore, they are thought to be new observational and morphological evidence of magnetic reconnection. Moreover, downflows are seen only in super hot plasma regions, which are located within cusp structures above post-flare loops (Akiyama 2001; Tsuneta 1996). The regions are also located beneath the reconnection points and are defined by magnetic flux which has just gone through reconnection. Therefore, the regions can be used to obtain some direct information about the magnetic reconnection process. Figure 5.1 shows sequence of images showing motion of downflows obtained with *Yohkoh*/SXT (McKenzie & Hudson 1999).

Recently, Innes, McKenzie, and Wang (2003a,b) reported similar downflows in extreme ultraviolet (EUV) images obtained with the *Transition Region and Coronal Explorer* (*TRACE*; Handy et al. 1999; Schrijver et al. 1999) and the Solar Ultraviolet Measurements of Emitted Radiation (SUMER) instrument (Wilhelm et al. 1995) aboard the *Solar and Heliospheric Observatory* (*SOHO*; Domingo, Fleck, and Poland 1995). By using the *TRACE* images, we have been able to examine downflows with higher spatial resolution than was done with *Yohkoh*/SXT. Furthermore, the SUMER data give spectroscopic information about the downflow. The results of spectroscopic analyses, which Innes et al. (2003a) performed, discard the possibility that the downflows are cold absorbing material, and support a model in which the downflows are moving voids. Innes et al. (2003b) found that highly blue-shifted features, which correspond to a Doppler velocity of up to 1000
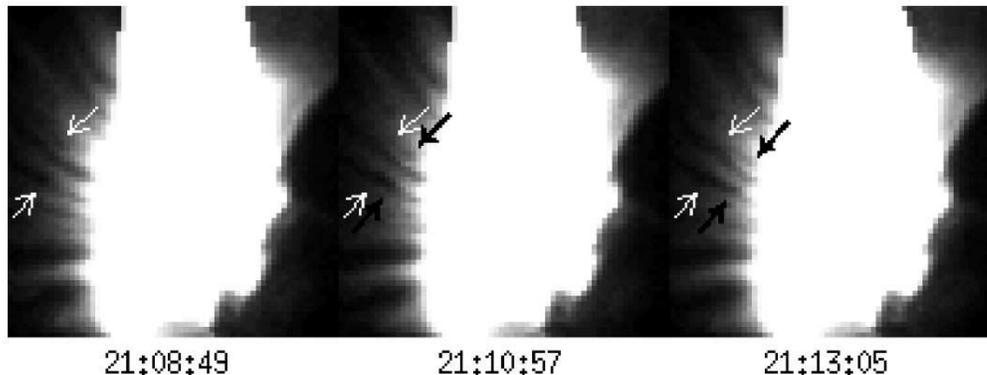
Figure 5.1: Sequence of images showing motion of SXT downflows. The white arrows show the locations of these two voids at 21:08:49 UT; the black arrows show the positions at later times. The main body of the arcade is not discernible in these half-resolution images because of pixel saturation (McKenzie & Hudson 1999).

km s^{-1}, were associated with the downflows, though it was not clear if they were the reconnection outflows themselves.

In this chapter, we examine the relationship between downflows and non-thermal emission, like hard X-ray (HXR) and microwave emissions, which implies strong energy release. If downflows are really related to magnetic reconnection, they are expected to be observed even in the impulsive phase, when magnetic reconnection occurs vigorously, and when nonthermal emissions are observed in HXRs and in microwaves. So far, almost all the downflows have been observed in long duration event (LDE) flares, and many of them (about 70% of all) were observed after the peak times of SXR light curves (McKenzie & Hudson 2001; Hudson & McKenzie 2001). In these events, therefore, HXR enhancements are not so strong to be compared with downflows. Moreover, although the *TRACE* downflows which Innes et al. (2003a,b) examined were observed to be accompanied by the impulsive HXR emission in the rise phase of a LDE flare, we could hardly identify the relationship between the downflows and the HXR emissions. This is because the size of the flare structure was huge, and too many downflows were observed at a time. On the other hand, in the 2002 July 23 solar flare we observed the *TRACE* downflows and the impulsive HXR and microwave bursts, simultaneously. Furthermore, we revealed, for the first time, that each downflow is correlated with HXR emission, since we could see few downflows at a time. In §5.2 we summarize the observational data and the features of the flare. In
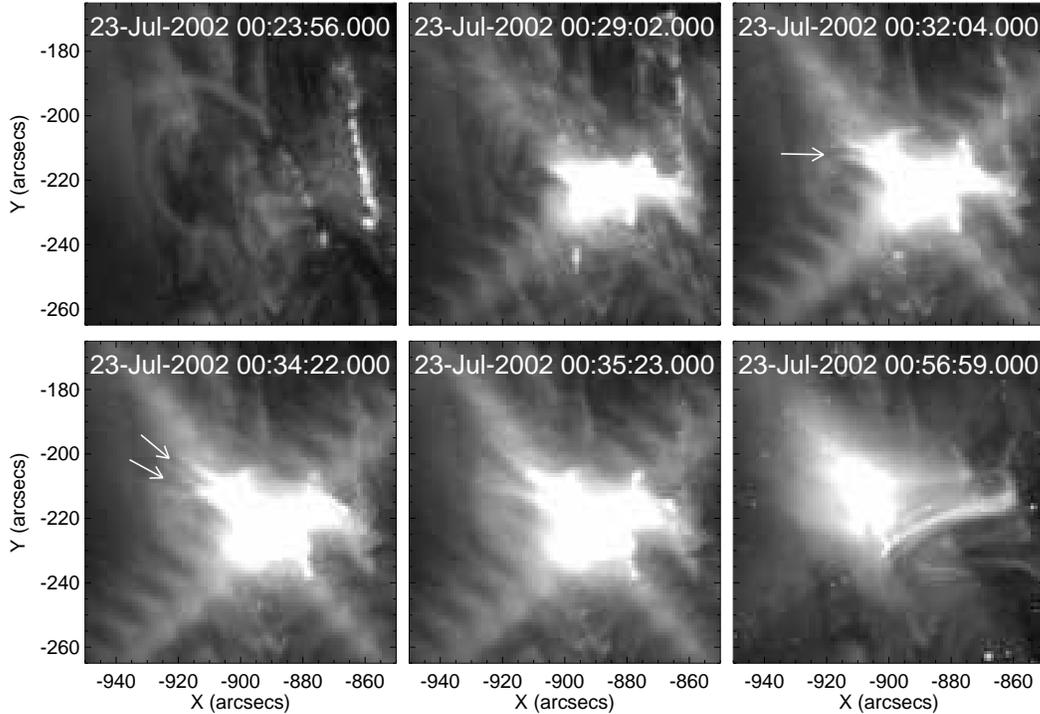
Figure 5.2: Temporal evolution of the 2002 July 23 flare in EUV 195 Å obtained with *TRACE*. Solar north is up, and west is to the right. The horizontal and vertical axes give the distance from the disk center in arcseconds. The *white* arrows indicate the downflows. The cross-shaped fringe structure is due to diffraction.

§5.3 we examine the downflows. We investigate the times when the downflows are seen, and compare them with the nonthermal radiation in HXRs and microwaves. In §5.4 a summary and discussion are given.

5.2 Observations

A large solar flare (X4.8 on the *GOES* scale) occurred in NOAA Active Region 10039 (S12°, E72°) at 00:18 UT, 2002 July 23. It showed a lot of spectacular features, which have been reported in a number of papers (e.g. Lin et al. 2003), and is famous as the first event in which γ-ray images were successfully obtained (Hurford et al. 2003) with the *Reuven Ramaty High Energy Solar Spectroscopic Imager* (*RHESSI*; Lin et al. 2002). Moreover, the
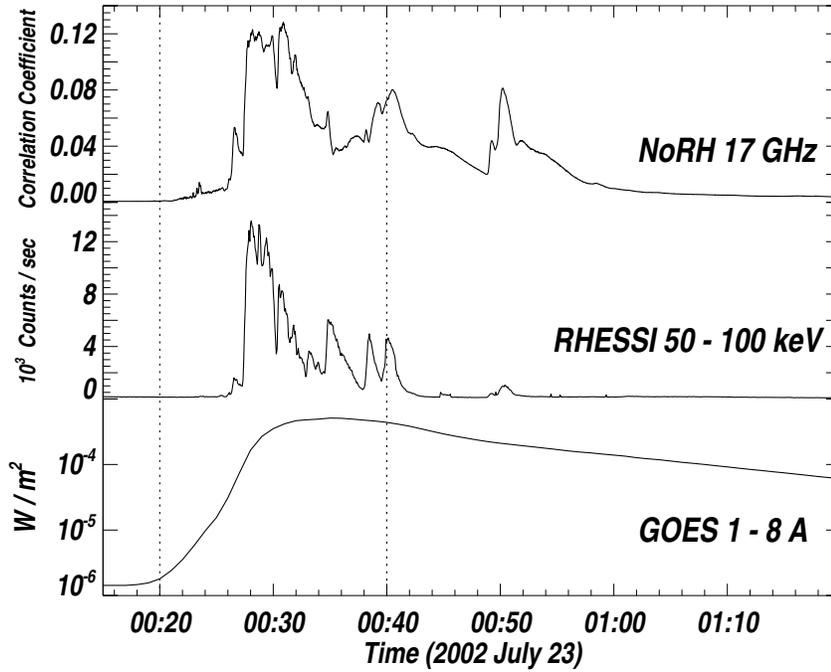
Figure 5.3: Light curves of the 2002 July 23 flare. *From top to bottom*: radio correlation plot observed at 17 GHz with NoRH; hard X-ray count rate measured with *RHESSI* (50 - 100 keV); soft X-ray flux in the *GOES* 1.0 - 8.0 Å channel. Two *dotted* vertical lines show the time range of the time slice images in Figure 5.4.

vertical evolution, such as ejections, formation of post-flare loops, downflows, and so on, are clearly seen, since the flare site is located near the southeast limb.

EUV images of the flare were obtained with *TRACE*. We used 195 Å images, in which the Fe XII line formed at ~ 1 MK is dominant. An emission line of Fe XXIV, formed at ~ 20 MK, is also contained but is usually much weaker (Handy et al. 1999). The pixel size of the CCD is 1''0, and the temporal resolution is about 9 s. Figure 5.2 shows the temporal evolution of the flare in the EUV. We cannot see clearly the post-flare loops owing to saturation of the images, but we can see a cross-shaped fringe pattern, like fish bones, due to diffraction. Although the super hot plasma region is much fainter than the post-flare loops, it is visibly spread above the loops. Krucker, Hurford, & Lin (2003) performed the co-alignment between the HXR data of the flare obtained with *RHESSI* and the EUV image with *TRACE*, and reported that the HXR coronal source is seen in the *RHESSI* low energy

range, 12 - 18 keV, and is located on the super hot plasma region seen in the *TRACE* 195 Å images. Emslie et al. (2003) performed imaging spectroscopy of the source, and reported that the region consists of thermal plasma which has a high temperature of up to 40 MK.

To examine nonthermal electrons, we also used the microwave total flux measured with the Nobeyama Radioheliograph (NoRH; Nakajima et al. 1994) and HXR data taken with *RHESSI*. Figure 5.3 shows the light curves of the flare in microwave, HXR, and SXR. The top line is that of NoRH 17 GHz, the middle one is that of *RHESSI*, 50 - 100 keV, the bottom one is that of the *GOES* 1.0 - 8.0 Å channel. As White et al. (2003) reported, the light curve in microwaves is quite similar to that in the HXR high energy range (greater than 50 keV).

5.3   TRACE Downflows

In the 2002 July 23 flare, we can see some dark downflows above the post-flare loops between about 00:26 and 01:20 UT. This time range corresponds not only to the decay phase but also to the impulsive and main phases of the flare (see the light curves of Fig. 5.3). Here, we concentrate on the vertical motion and the timing of the downflows. The top right and middle panels in Figure 5.4 show time slice images from 00:20 to 00:40 UT (negative images). This time range of the time slice images corresponds to the impulsive phase, and the chosen area is the sandwiched time with two vertical dotted lines in Figure 5.3. The bottom dark (bright in the real images) regions are post-flare loops. They are so bright in the *TRACE* images because of saturation that no fine structures is identified. Above this region, we can see a much fainter dark region, — the super hot region. Several downflows can be seen which are pointed out with arrows. The apparent speeds of the downflows are between 100 and 250 km s^{-1}. They are decelerated at the top of the post-flare loops. The bottom panel in Figure 5.4 shows the HXR and microwave light curves obtained with *RHESSI* (50 - 100 keV) and the NoRH (17 GHz), respectively. The arrows point out the same times shown in the upper panels. They correspond to the times when nonthermal bursts occur. The HXR and microwave intensities are thought to be proportional to the amount of the magnetic energy released per unit time (Neupert 1968; Wu et al. 1986; Hudson 1991). Therefore, the results imply that the downflows appear when strong magnetic energy release occurs, and that they are, or are correlated with, reconnection outflows.

To make the relation more clear, we plotted the correlation plot between the times of the nonthermal bursts in HXR/microwave and those of the down-
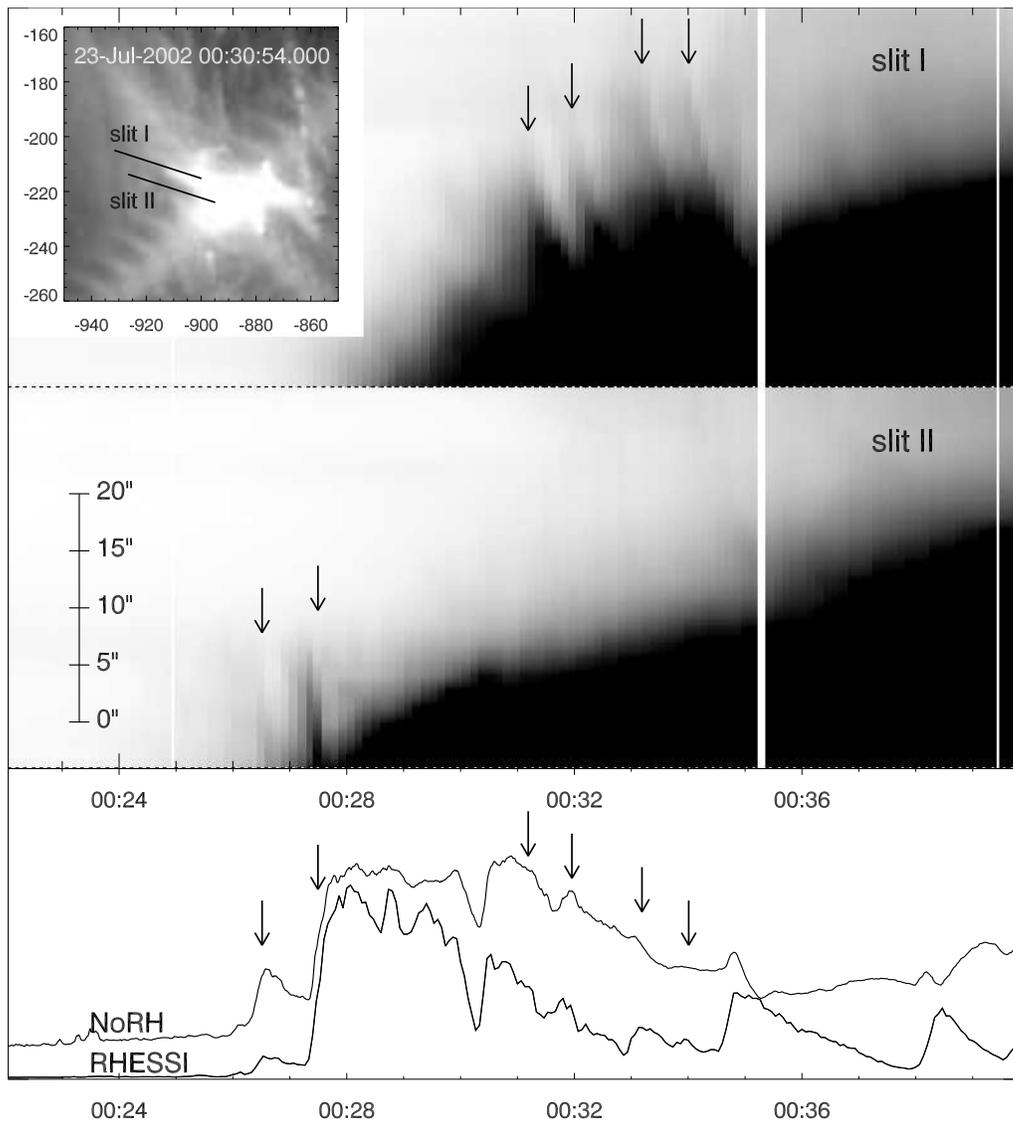
Figure 5.4: *Top left*: EUV image of the flare obtained with *TRACE*. The *black* solid lines illustrate the position of the slit lines I and II. *Top right and middle*: Time-sequenced EUV (195 Å) images obtained with *TRACE* along the slit lines I and II, respectively. The horizontal axis is time (UT), and the vertical axis is the space along the slits. *Bottom*: microwave (17 GHz) and HXR (50 - 100 keV) light curves obtained with NoRH and *RHESSI*, respectively.
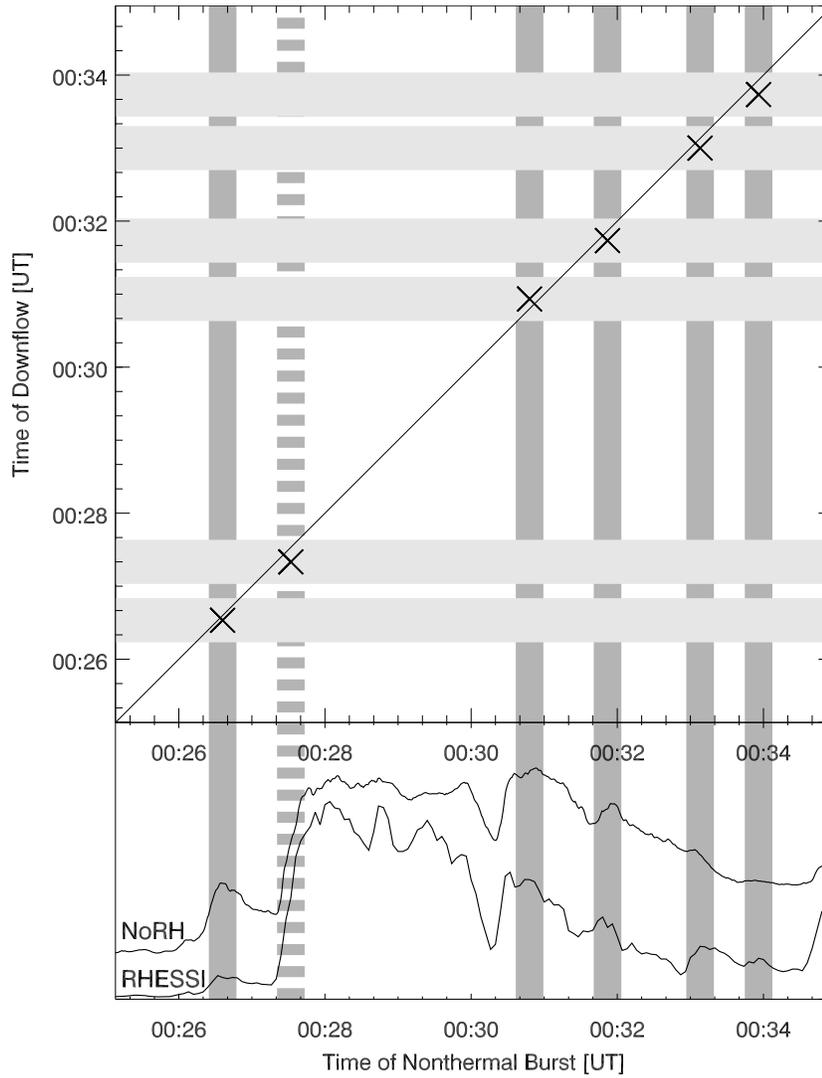
Figure 5.5: *Top* : Correlation plot between the times of the nonthermal bursts and those of the downflows. Both the horizontal and vertical axes show the times (UT). The horizontal (*light gray*) and the vertical (*dark gray*) thick lines illustrate the times of the downflows and those of the nonthermal bursts, respectively. The width of the thick lines shows the amount of error approximately. *Bottom* : Microwave (17 GHz) and HXR (50 - 100 keV) light curves obtained with NoRH and *RHESSI*, respectively.

flows in Figure 5.5. The horizontal (*light gray*) and the vertical (*dark gray*) thick lines illustrate the times of the downflows and those of the nonthermal bursts, respectively. The times of the nonthermal bursts are chosen to be the peak times the bursts, except for the second from the left (*dashed line*). The HXR burst, which starts at 00:27:30 UT, is the biggest, and seems to consist of some subbursts. Therefore, we chose the middle time from the start to the peak of the burst, instead of the peak time. In the bottom panel we showed the microwave (17 GHz) and HXR (50 - 100 keV) light curves as a comparison. The times of the downflows are selected to be the times when the downflows enter the superhot region. To determine the time, we drew a line to follow the top edge of the superhot region in the time slice images. Then, we extrapolated the path of each downflow, and chose the intersection of those two lines as the time of the downflow. Thin solid line shows the points where the times of the downflows correspond to those of the HXR bursts (*diagonal line*). Only the line indicates a relationship between the two light curves. These times have fairly large errors, but nevertheless, cross points ($\times$) of both the times lie along the diagonal line. Therefore, Figure 5.5 supports the suggestion that the times of the downflows correspond to the times when nonthermal bursts occur. To confirm this, we compared two time sequences of randomly occurring hypothetical features corresponding to HXR bursts and downflows and plotted them in the same way. Then, we confirmed the probability that the relationship such as indicated in Figure 5.5 could happen by chance is about 50% - 60%. In the present case, all the downflows, at least observable ones, have their HXR burst counterparts, and the occurrence of the correlation is significantly higher than that of the random case.

5.4 Summary and Discussion

We have examined in detail the evolution of a big two-ribbon flare which occurred on 2002 July 23. We found downflows above the post-flare loops, and that they are seen not only in the decay phase, but also in the impulsive and main phases. Furthermore, they appear to correspond to the times when nonthermal bursts in microwaves and HXRs occurred. This result implies that the downflow motions occurred when strong magnetic energy was released, and suggests that they are correlated with reconnection outflows. Thus, we have been able to add a new piece of observational evidence to the model that downflows are reconnection outflow (McKenzie and Hudson 1999; McKenzie 2000).

Another piece of observational evidence of reconnection outflows is the X-

Table 5.1: Comparison between the features of the plasmoid ejection and those of the downflow

	Plasmoid Ejection	Downflow
velocity [km s^{-1}]	30-500	45-500
size [km]	1-10 $\times 10^4$	2-10 $\times 10^3$
density [cm^{-3}]	1-10 $\times 10^9$	$\sim 10^{9a}$
impulsive phase	Yes	Yes
decay phase	No	Yes
HXR/μ-wave	Yes	Yes^b

^{a} The temperature of downflows is still uncertain.
^{b} New findings in this work.

ray plasmoid ejections which have been studied by several authors (Shibata et al. 1995; Tsuneta 1997; Ohyama & Shibata 1997, 1998). Kahler (1988) reported the similar relationship between filament eruptions and HXR emissions. These observations revealed a close relationship between plasmoid ejections and HXR emissions and showed that plasmoids/filaments are strongly accelerated during the impulsive phase (i.e. during HXR burst). A good review of the correlation between plasmoid ejections and HXR emission is presented by Aschwanden (2002). Recently, H. Takasaki (private communication) found multiple X-ray plasmoid ejections which were associated with the 2000 November 24 flare. He reported that each of the ejections appears at a time corresponding to each HXR peak in the impulsive HXR emission. Moreover, Sheeley & Wang (2002) reported that both the downflow-like features and the upward motion, are simultaneously observed, with the Large Angle Spectrometric Coronagraph aboard *SOHO*. From these results, we suppose that both the downflows and the plasmoid ejections are reconnection outflows. We present a cartoon of this model in Figure 5.6. Plasmoids are generated in the current sheet, and are ejected as downward (downflows) and upward (X-ray plasmoid ejections), when strong energy releases occur (Fig. 5.6a). Therefore, the correlations between plasmoid ejections, or downflow, and HXR bursts represent a plasmoid-induced, nonsteady reconnection (Shibata 1999; Shibata & Tanuma 2001). As summarized in Table 5.1, downflows show common features with X-ray plasmoid ejections.

What on earth (sun?) are the downflows? To answer this question, we have to examine the mechanism and the process of magnetic reconnection and the relationship between the reconnection outflow and the downflow in much more detail. A reconnection model and numerical simulation based
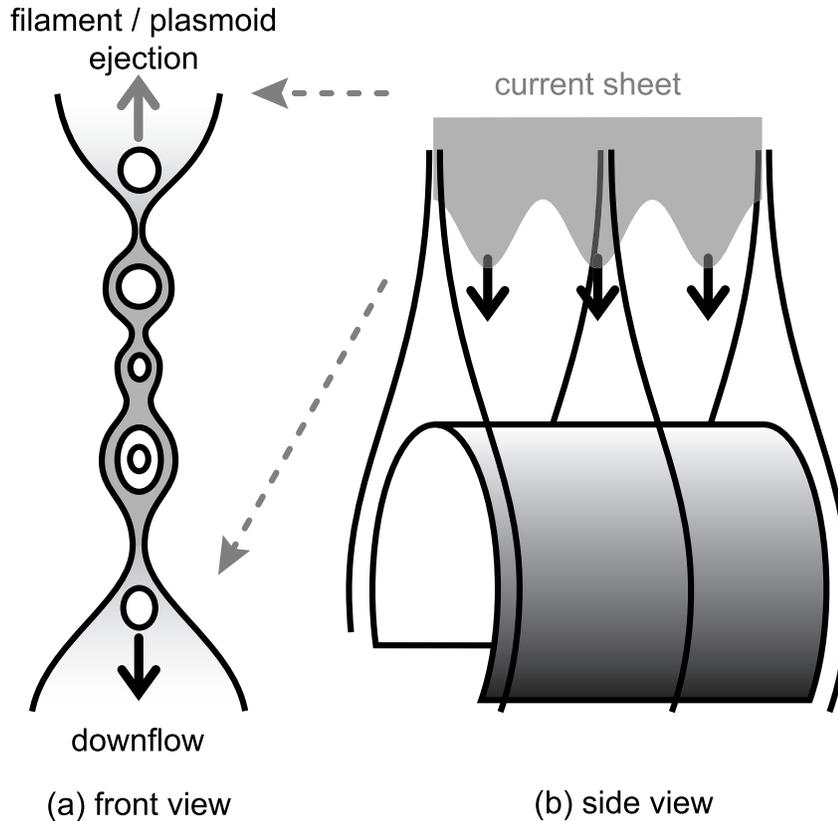
Figure 5.6: Model of the downflows and plasmoid ejections. (a) Front view of the structure. Many plasmoids are created inside current sheet (gray region). (b) Side view. The current sheet is modifiied owing to some instabilities.

on the model, which is consistent with all the features of the downflows, such as the low-density, high Doppler-shift, relationship with the bursts of nonthermal emission, is required. Some authors, such as Kliem, Karlický, & Benz (2000), Tanuma et al. (2001), and so on, have performed numerical simulations of magnetic reconnection, and have shown that fractal plasmoids are generated in the current sheet. Kliem et al. (2000) also applied their results to the observed features in microwave emission. Those plasmoids are ejected bidirectionally, associated with enhancement of reconnection rate. Forbes & Priest (1983), Cheng et al. (2003), and so on, have studied the relationship between plasmoid ejection and enhancement of energy release in their numerical simulations. Furthermore, TanDokoro & Fujimoto (2004) have examined the instability at the leading edge of a reconnection jet in their new 3D numerical simulation. The reconstructed leading edge is a narrow

and elongated structure (as shown in the rough cartoon of Fig. 5.6b), and is similar to the shape of the downflows. These works may help to explain what downflows are.

Bibliography

Akiyama, S. 2001, Ph.D. thesis (The Graduate University for Advanced Studies)

Aschwanden, M. J. 2002, Space, Sci., Rev., 101, 1

Cheng, C. Z., Ren, Y., Choe, G. S., Moon, Y.-J. 2003, ApJ, 596, 1341

Domingo, V., Fleck, B., Poland, A. I. 1995, Sol. Phys., 162, 1

Emslie, A. G., Kontar, E. P., Krucker, S., Lin, R. P. 2003, ApJ, 595, L107

Handy, B. N., et al. 1999, Sol. Phys., 187, 229

Hara H., Tsuneta, S., Lemen, J. R., Acton, L. W., McTiernan, J. M. 1992, PASJ, 44, 135

Hudson, H. S. 1991, Sol. Phys., 133, 357

Hudson, H. S. & McKenzie, D.E. 2001, Earth Planets Space, 53, 581

Hurford, G. J., Schwartz, R. A., Krucker, S., Lin, R. P., Smith, D. M., Vilmer, N. 2003, ApJ, 595, L77

Innes, D. E., McKenzie, D. E., Wang, T. 2003a, Sol. Phys., 217, 247

Innes, D. E., McKenzie, D. E., Wang, T. 2003b, Sol. Phys., 217, 267

Kahler, S. W., Moore, R. L., Kane, S. R., Zirin, H. 1988, ApJ, 824

Kliem, B., Karlický, M., Benz, A. O. 2000, A&A, 360, 715

Krucker, S., Hurford, G. J., Lin, R. P. 2003, ApJ, 595, L103

Lin, R. P., et al. 2002, Sol. Phys., 210, 3

Lin, R. P., et al. 2003, ApJ, 595, L69

McKenzie, D. E. & Hudson, H. S. 1999, ApJ, 519, L93

McKenzie, D. E. 2000, Sol. Phys., 195, 381

McKenzie, D. E. & Hudson, H. S. 2001, Earth Planets Space, 53, 577

Nakajima, H., et al. 1994, in Proc. of the IEEE, 82, 705

Neupert, W. M. 1968, ApJ, 153, L59

Ogawara, Y., Takano, T., Kato, T., Kosugi, T., Tsuneta, S., Watanabe, T., Kondo, I., and Uchida, U. 1991, Sol. Phys., 136, 10

Ohyama, M. & Shibata, K. 1997, PASJ, 49, 249

Ohyama, M. & Shibata, K. 1998, ApJ, 499, 934

Sheeley, N. R. Jr. & Wang Y.-M. 2002, ApJ, 579, 874

Schrijver, C. J., et al. 1999, Sol. Phys., 187, 261

Shibata, K., Masuda, S., Shimojo, M., Hara, H., Yokoyama, T., Tsuneta, S., Kosugi, T., Ogawara, Y. 1995, ApJ, 451, L83

Shibata, K. 1999, Ap&SS, 264, 129

Shibata, K. & Tanuma, S. 2001, Earth Planets Space, 53, 473

TanDokoro, R. & Fujimoto, M. 2004, Adv. Space Res, in press

Tanuma, S., Yokoyama, T., Kudoh, T., Shibata, K. 2001, ApJ, 551, 312

Tsuneta, S., et al. 1991, Sol. Phys., 136, 37

Tsuneta, S. 1996, ApJ, 456, 840

Tsuneta, S. 1997, ApJ, 483, 507

White, S. M., Krucker, S., Shibasaki, K., Yokoyama, T., Shimojo, M., Kundu, M. R. 2003, ApJ, 595, L111

Wilhelm, K., et al. 1995, Sol. Phys., 162, 189

Wu, S. T., et al. 1986, in Energetic Phenomena on the Sun, ed.s M. Kundu & B. Woodgate (NASA CP-2439), 5-i

Chapter 6

Periodic Acceleration of Electrons[††]

As we already mentioned in Chapter 1, nonthermal energetic particles are accelerated, which are associated with energy release processes such as magnetic reconnection in solar flare. To understand such unsolved question as particle acceleration mechanism, we investigate the relationship between the features of the nonthermal emissions and global magnetic field configuration during flares. In this chapter we present an examination of the multiwavelength observation of a C7.9 flare that occurred on 1998 November 10. This is the first imaging observation of the quasi-periodic pulsations (QPPs). Four bursts were observed with the hard X-ray telescope aboard *Yohkoh* and at the Nobeyama Radioheliograph during the impulsive phase of the flare. In the second burst, the hard X-ray and microwave time profiles clearly showed a QPP. We estimated the Alfvén transit time along the flare loop using the images of the soft X-ray telescope aboard *Yohkoh* and the photospheric magnetograms and found that the transit time was almost equal to the period of the QPP. We therefore suggest, based on a shock acceleration model, that variations of macroscopic magnetic structures, such as oscillations of coronal loops, affect the efficiency of particle injection/acceleration.

6.1   Background of This Work

Particle acceleration in solar flares is one of open questions which has been intensely discussed, and to understand the mechanism is itself very important topic not only for the solar physics but also for other fields such as plasma physics, geomagnetic physics, and so on. In solar flares we often examine the mechanism, investigating the relationship between the various features of nonthermal emissions associated with particle acceleration and the global magnetic filed structure of the flares, and we restrict the magnetic reconnection mechanisms and/or energy release mechanisms, if it is possible. Nonthermal electrons generated in the impulsive phase of a flare are observed in hard X-rays, γ-rays, and microwaves. The light curves in these wavelengths show short-lived bursts with durations between 10 s and 10 minutes (Dulk, McLean, & Nelson 1985). These bursts include smaller pulses with shorter duration, and they sometimes show periodicity.

A good example of such quasi-periodic pulsations (QPPs) was seen in a flare on 1980 June 7 (Kiplinger et al. 1983; Fig. 6.1). Nakajima et al. (1983) and Kane et al. (1983) examined the temporal evolution of the X-ray and radio spectra and the spatial structure of the flare. They suggest that the quasi-periodic pulses indicate a modulation of the particle injection/acceleration rate. Tajima, Brunel, & Sakai (1982) showed by numerical simulation that stored magnetic energy is explosively transformed to particle acceleration. They also suggest that the current loop coalescence instability induces the QPPs. Moreover, Tajima et al. (1987) showed that the period of the QPP is equal to the Alfvén transit time "across" the current loop. However, these works were mainly based on the total flux, and the detailed spatial configuration of the flare that shows QPP is still unknown, and the relationship between the QPP and the magnetic loop structure is still unclear.

On 1998 November 10 a solar flare (C7.9 on the *GOES* scale) occurred in NOAA Active Region (AR) 8375. The flare was observed by *Yohkoh* (Ogawara et al. 1991) and the Nobeyama Radio Observatory and clearly showed quasi-periodic behavior in the hard X-ray and microwave time profiles. In this chapter, we analyze the QPP using the high-resolution X-ray and microwave images. Then we compare the period of the QPP with typical timescales of flare loops. Finally, we discuss the effect of the magnetic structure on the particle injection/acceleration rate.
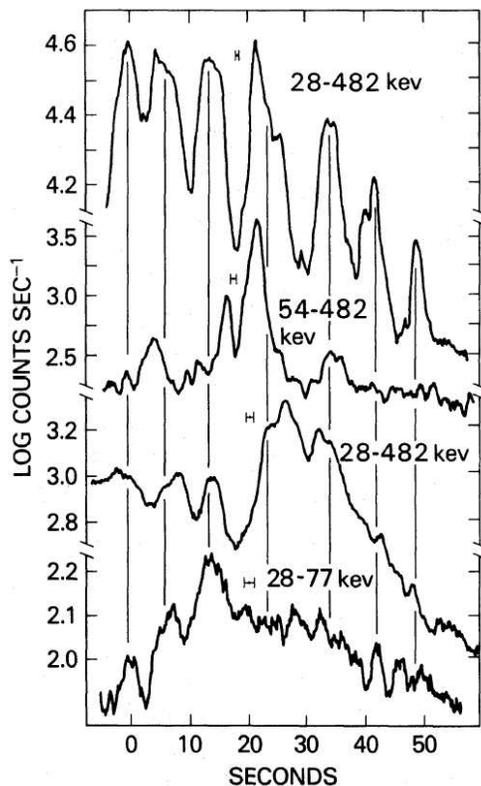
Figure 6.1: The four light curves of impulsive phases of the flare of 1980 June 7, which are arbitrary shifted in time to align features. Energy ranges have been selected to enhance impulsive features (Kiplinger et al. 1983).

6.2 Observations

The solar flare occurred in NOAA AR 8375 (N19°, W78°) at 00:10 UT, 1998 November 10. Microwave images of the flare were taken with the Nobeyama Radioheliograph (NoRH; Nakajima et al. 1994), which observed the sun at 17 and 34 GHz with a temporal resolution of 1.0 s. The spatial resolutions of NoRH data are 12″ for 17 GHz and 6″ for 34 GHz. The Nobeyama Radio Polarimeter (NoRP; Torii et al. 1979; Shibasaki et al. 1979; Nakajima et al. 1985) measured the total flux of the flare at 1, 2, 3.75, 9.4, 17, 34, and 80 GHz with a temporal resolution of 0.1 s. The hard X-ray images were obtained with the hard X-ray telescope (HXT; Kosugi et al. 1991) aboard *Yohkoh*, with a spatial and temporal resolution of about 5″ and 0.5 s, respectively. The soft X-ray images were also obtained with the *Yohkoh* soft X-ray telescope (SXT; Tsuneta et al. 1991). We used full-resolution images in the partial
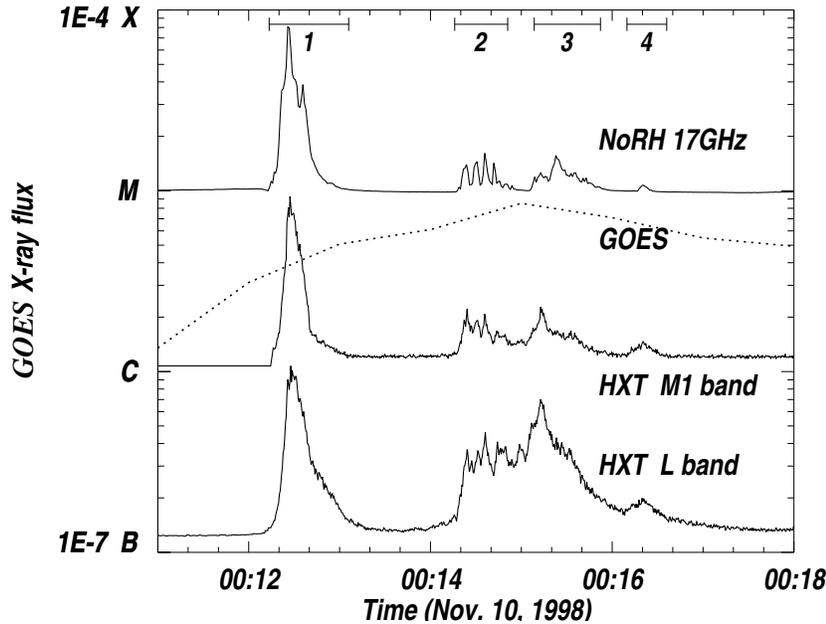
Figure 6.2: Temporal evolution of the 1998 November 10 flare. *From top to bottom*: Radio correlation plot observed at 17 GHz with NoRH (scaled arbitrarily); soft X-ray flux in the *GOES* 1.0 - 8.0 Å channel (*dotted line*); and hard X-ray count rate measured in the M1 band (23 - 33 keV) and L band (14 - 23 keV) of *Yohkoh*/HXT (scaled arbitrarily). Four bursts are identified by the numbered top bars.

frame image mode with a spatial resolution of about $2''.5$.

Figure 6.2 shows the microwave, soft X-ray, and hard X-ray time profiles. The top solid line is that of the NoRH 17 GHz, the dotted line is the *GOES* 1.0 - 8.0 Å channel, the middle solid line is the HXT M1 band (23 - 33 keV), and the bottom solid line is the HXT L band (14 - 23 keV). Four bursts with duration between 10 and 30 s are seen in the microwave and hard X-ray emission. The fine spikes in the second burst clearly show the QPPs in both microwaves and hard X-rays. In this chapter, we investigate the quasi-periodic nature of the second burst.

Figure 6.3 shows the images of NoRH/17 GHz, the HXT/M1 band, and the SXT at the second burst. The flare shows a double source in the microwave data (*gray contours*). We refer to the northern and brighter source as the "source A" and the other one as "source B". On the other hand, in the hard X-ray data (*black contours*) only one source is seen near source B.
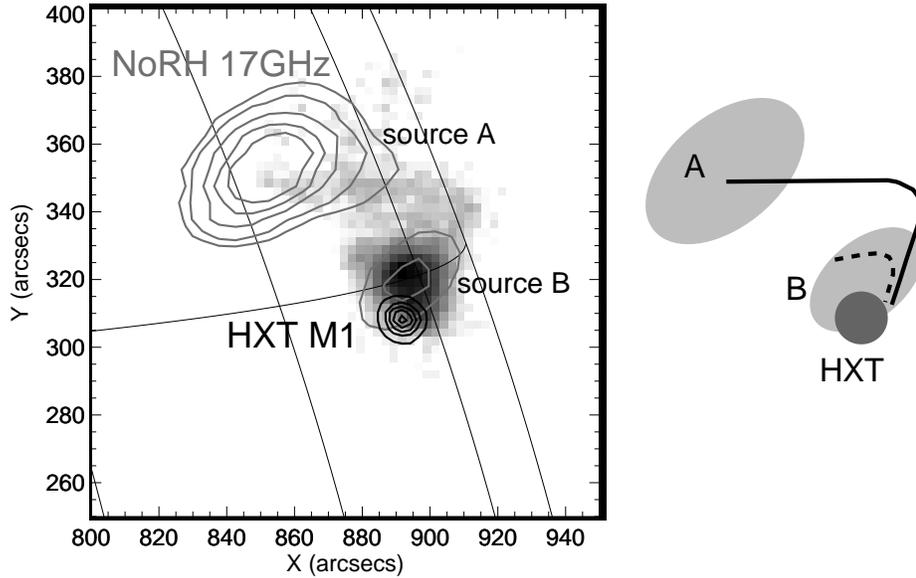
Figure 6.3: *Left*: Co-aligned images of the flare. SXT (Be filter) image at 00:14:32 UT is shown by the gray scale. NoRH (17 GHz; *gray contour*) image at 00:14:37 UT is plotted at brightness temperatures of 150,000, 200,000, 300,000, 400,000, and 500,000 K. HXT (M1 band, 23 - 33 keV) image at 00:14:33 UT is drawn as the black contour. Contour levels are 90%, 70%, 50%, 30%, and 10% of the peak intensity. *Right*: Simple sketch of this region. The NoRH sources, the HXT source, and SXT faint loop are displayed in light gray, dark gray, and a black solid line, respectively. There probably are flare loops (*dashed line*; see §6.3) in microwave source B.

This is common in the L and M1 bands of HXT, but it is unknown whether it is also common in the M2 (33 - 53 keV) and H (53 - 93 keV) bands. We could not synthesize the hard X-ray images in these bands at the time due to insufficient counts. The soft X-ray image (*gray scale*) shows a small bright kernel at the same region at source B. We can also see a faint loop that connects the bright kernel and the radio source A.
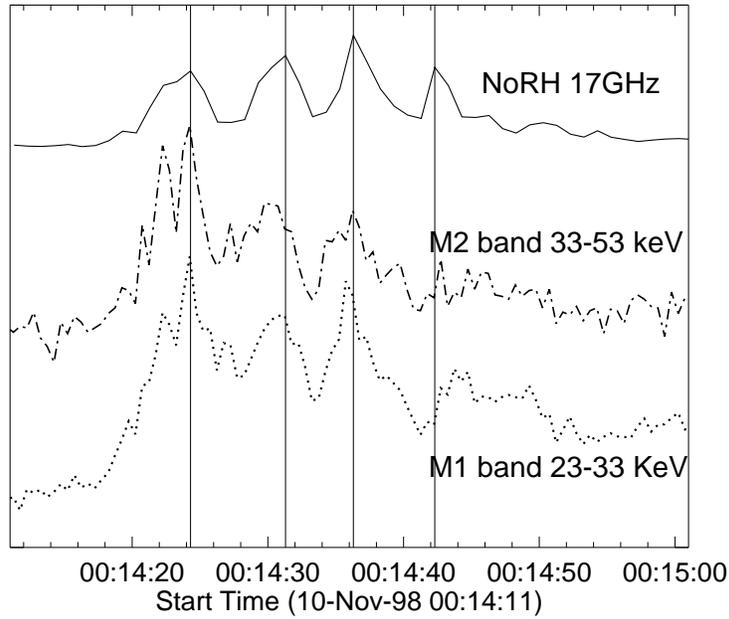
Figure 6.4: Light curves of the second burst (scaled arbitarily). From top to bottom: radio brightness temperature observed at 17 GHz by NoRH (*solid line*); hard X-ray count rate measured in the M2 band (33 - 53 keV) (*dash dot line*) and M1 band (23 - 33 keV) (*dotted line*) of *Yohkoh*/HXT. The vertical lines show the peak times of the microwave emission.

6.3   Periodic Pulsation

Figure 6.4 presents the hard X-ray and microwave time profiles for the second burst, from 00:14:20 UT to 00:14:40 UT. The QPPs are clearly seen. In the time profiles obtained with the NoRP data, the QPPs are seen in 9.4 and 17 GHz. The period calculated from the autocorrelation function of the time profiles was 6.6 s. We also calculated the period of the QPPs in hard X-rays (M1 and M2 bands) and found that the period (6 s) was almost the same as those in NoRP. We analyzed the microwave spectrum using the NoRP data and found that the power-law distribution index was about -2 to -1.5 and the turnover frequency was about 10 GHz. These results indicate that the emission of the QPP originated from gyrosynchrotron radiation from nonthermal electrons. Since both the time profiles of the M1 and M2 bands clearly showed the QPPs, the emission in hard X-rays was also produced by nonthermal electrons.

As described in §6.2, the flare has two microwave sources (see Fig. 6.3). We found that the time profile of source A showed the QPP, while that of source B did not. The pulsating source is different from the hard X-ray source that is located near source B. To clarify the relation between the microwave pulsation at source A and the hard X-ray pulsation, we calculated the correlation between the time profiles of 17 GHz and the M1 band as a function of the time lag between them. The maximum correlation was found for a delay of the microwave pulsation with a time of $0.6 - 1.0$ s.

We suggest that the acceleration site lies near the hard X-ray source and that the delay time between microwaves and hard X-rays is explained by the flight duration of nonthermal electrons from one source to the other. The length of the soft X-ray faint loop connecting the hard X-ray source and source A is about 5.0×10^4 km. If we assume that the velocity of the electrons is about 1.0×10^5 km s^{-1} (~ 30 % of the speed of light), the delay time between microwaves and hard X-rays is about 0.5 s, which is almost equal to the observed delay time. The soft X-ray images show two parts related to the flare: a bright kernel near source B and a faint large loop connecting the kernel and source A (see Fig. 6.3). We believe that the flare occurred at the contact region of the two parts via magnetic reconnection (Hanaoka 1997; Heyvaerts, Priest, & Rust 1977). In such a scenario, the acceleration site would be located near the reconnection site. Hence, it is reasonable to suggest that the acceleration site is located near source B and the hard X-ray source.

Here, another question occurs: Why did the time profile of the microwave source B not show the QPP? As an answer, we suggest that the emission mechanism of source B differs from that of source A. The emission mechanism of source A is optically thin gyrosynchrotron radiation from nonthermal electrons. On the other hand, the dominant emission mechanism of source B is optically thin thermal bremsstrahlung since the spectrum index of source B that is derived from the 17 and 34 GHz is about 0. Therefore, the time profiles of source B do not show the population of the accelerated/injected nonthermal electrons. To confirm the suggestion, we estimated the thermal radio flux from source B by using the temperature and the emission measure of the SXT bright kernel (see §6.4), and found that the flux was almost the same as the observed flux of source B. We also suggest that the thermal emission was radiated from the thermal plasma that was confined by the flare loops. The loops were formed at the first burst via magnetic reconnection. Therefore, although the fine structure of the kernel is not resolved in the SXT images, we think that it consists of the main flare loops (see Fig. 6.3).

6.4   Typical Timescales of the Flare Loop

In §6.3, we showed that the period of the pulsation was 6.6 s. What is the explanatin for the period? To answer the question, we derive some typical timescales of the flare loop and discuss them. Temperature, density, size, and magnetic field strength of the flare loop are needed for the estimation. The temperature T and the volume emission measure EM are derived from the soft X-ray images that were taken with the SXT thick aluminum (Al12) and beryllium (Be) filters. The region of flare loop B is defined as the region where the intensity of an SXT Be filter image is more than 2000 DN s^{-1} pix^{-1}. This leads to an area of 2.5×10^{18} cm^2. Using the filter ratio method (Hara et al. 1992), the average temperature and volume emission measure over the flare loop are calculated to be 9.4 MK and 8.1×10^{48} cm^{-3}, respectively.

Here, we assume that the kernel is a cube, and that the volume V of the flare kernel is the area to the power of three halves, i.e., $V = A^{3/2}$. Then, the number density n in the top of the flare loop becomes $n = (EM/V)^{1/2} = (EM/A)^{3/2} \approx 4.5 \times 10^{10}$ cm^{-3}. Also, the acoustic velocity c_s in the flare loop is given by $c_s \approx (\gamma k_B T/m_p)^{1/2} \approx 360$ km s^{-1}, where k_B is Boltzmann's constant, m_p is the proton mass, and γ is the ratio of specific heats and is here assumed to be $5/3$. Since the structure of the flare loop is not resolved in the SXT images, we can not measure the length l and width w of the flare loop correctly. Therefore, we use the square root of the area instead of the length of the flare loop ($l \sim A^{1/2} \sim 16{,}000$ km). Then, the acoustic transit time "along" the flare loop is $\tau_{s,l} = l/c_s \approx 44$ s. On the other hand, if we use the width of the faint loop instead of the width of the flare loop ($w \sim 6000$ km), the acoustic transit time "across" the flare loop becomes $\tau_{s,w} = w/c_s \approx 17$ s. Both the timescales are much longer than the observational period of the QPP (6.6 s).

In order to derive the Alfvén transit times of the flare loop, we have to estimate the magnetic field strength in the corona. However, this estimation is difficult in our case as (1) we cannot measure the magnetic field strength of the corona directly, and (2) we cannot obtain the actual magnetic field strength in the photosphere at the flare region since it is located near the north-west limb. Therefore, we calculate the potential field of the flare region based on a magnetogram on November 6. The magnetogram was obtained with the Michelson Doppler Interferometer (MDI; Scherrer et al. 1995) aboard the *Solar and Heliospheric Observatory* (*SOHO*; Domingo, Fleck, & Poland 1995). The field strength on the apex of the flare loop B is estimated to be about 300 G using the potential field extrapolation by the software package MAGPACK2 (Sakurai 1982). As a result, the Alfvén velocity c_A in the flare loop becomes $c_A \approx B/(4\pi n m_p)^{1/2} \approx 3100$ km s^{-1}.

Table 6.1: Physical Values of Flare Loop

Parameter	Value
Area (A)	2.5×10^{18} cm^2
Volume (V)	4.0×10^{27} cm^3
Length (l)	1.6×10^{9} cm
Width (w)	$\sim 6.0 \times 10^{8}$ cm
Temperature (T)	9.4×10^{6} K
Number density (n)	4.5×10^{10} cm^{-3}
Magnetic field (B)	~ 300 G
Acoustic velocity (c_s)	3.6×10^{2} km s^{-1}
Alfvén velocity (c_A)	3.1×10^{3} km s^{-1}
Acoustic transit time:	
along the loop $(\tau_{s,l})$	44 s
across the loop $(\tau_{s,w})$	17 s
Alfvén transit time:	
along the loop $(\tau_{A,l})$	5.1 s
across the loop $(\tau_{A,w})$	1.9 s

Then, the Alfvén transit time "along" the flare loop is $\tau_{A,l} = l/c_A \approx 5.1$ s and the Alfvén transit time "across" the flare loop is $\tau_{A,w} = w/c_A \approx 1.9$ s.

The values of our estimations are summarized in Table 6.1. Although the Alfvén transit time is sensitive to the magnetic field strength estimated above, the transit time along the flare loop $(\tau_{A,l})$ is the most reasonable to the observational period of the pulsation in microwaves and hard X-rays.

6.5 Discussion

We investigated the impulsive phase of the flare whose time evolution showed a clear QPP in microwaves and hard X-rays. We found that the periods of the QPP were 6.6 s and that the acceleration site of nonthermal electrons was located near source B using correlation analysis of the time profiles. Then, we estimated some typical timescales of the flare loop from the observational data and found that the Alfvén transit time along the flare loop was close to the period of the pulsation.

Tajima et al. (1987) suggest that the periods of QPP in microwaves and hard X-rays are equal to an Alfvén transit time across the flare loop $(\tau_{A,w})$. However, this transit time was much shorter than the observational period of the QPP. This implies that the origin of the periodic pulsation in our case

is not the coalescence instability in the reconnection site.

Recently, *Transition Region and Coronal Explorer* (Handy et al. 1999) observations have shown coronal loop oscillations that was induced by a flare (Nakariakov et al. 1999). Miyagoshi, Yokoyama, & Shimojo (2004) performed three-dimensional MHD simulations of the coronal loop oscillation and found that the period of the loop oscillation is equal to the Alfvén transit time along the oscillating loops ($\tau_{A,l}$). Does the oscillation of the coronal loop relate with the particle acceleration/injection? Tsuneta & Naito (1998) propose that nonthermal electrons can efficiently be accelerated by a first-order Fermi process at the fast shock located below the reconnection X-point. They suggest that the accelerated electrons are trapped between the two slow shocks and that the energy injection depends on the length of the fast shock which is pinched by these slow shocks. If the reconnected (flare) loop that is located under the fast shock is oscillating, then the length of the fast shock probably varies with the loop oscillation, synchronously. Hence, we propose, under the hypothesis of the acceleration model proposed by Tsuneta and Naito (1998), that the origin of the QPP in microwaves and hard X-rays is the modulation of the acceleration/injection of nonthermal electrons. Moreover, we propose that the modulation is produced by the variations of macroscopic magnetic structures, for example, oscillations of coronal loops.

Bibliography

Domingo, V., Fleck, B., and Poland, A. I. 1995, Sol. Phys., 162, 1

Dulk, G. A., McLean, D. J., & Nelson, G. J. 1985, Solar Radiophysics: Studies of emission from the sun at metre wavelengths, ed.s McLean D. J. & Labrum N. R. (Cambridge: Cambridge University Press), 53

Hanaoka, Y. 1997, Sol. Phys., 173, 319

Handy, B. N., et al. 1999, Sol. Phys., 187, 229

Hara, H., Tsuneta, S., Lemen, J. R., Acton, L. W., and McTiernan, J. M. 1992, PASJ, 44, 135

Heyvaerts, J., Priest, E. R., and Rust, D. M. 1977, ApJ, 216, 123

Kane, S. R., Kai, K., Kosugi, T., Enome, S., and Landecker, P. B., & McKenzie, D. L. 1983, ApJ, 271, 376

Kiplinger, A. L., Dennis, B. R., Frost, K. J., & Orwig, L. E. 1983, ApJ, 273, 783

Kosugi, T., et al. 1991, Sol. Phys., 136, 17

Miyagoshi, T., Yokoyama, T., Shimojo, M. 2004, PASJ, 56, in press

Nakajima, H., Kosugi, T., Kai, K., & Enome, S. 1983, Nature, 305, 292

Nakajima, H., et al. 1985, Publ. Astron. Soc. Japan, 37, 163

Nakajima, H., et al. 1994, in Proc. of the IEEE, 82, 705

Nakariakov, V. M., Ofman, L., DeLuca, E. E., Roberts, B., & Davila, J. M. 1999, Science, 285, 862

Ogawara, Y., Takano, T., Kato, T., Kosugi, T., Tsuneta, S., Watanabe, T., Kondo, I., & Uchida, Y. 1991, Sol. Phys., 136, 10

Sakurai, T. 1982, Solar phys., 76, 301

Scherrer, P. H., et al. 1995, Sol. Phys., 162, 129

Shibasaki, K., Ishiguro, & M., Enome, S. 1979, in Proc. of the Res. Inst. of
Atmospherics, Nagoya Univ., 26, 117

Tajima, T., Brunel, F., and Sakai, J. 1982, ApJ, 258, L45

Tajima, T., Sakai, J., Nakajima, H., Kosugi, T., Brunel, F., & Kundu, M.
R. 1987, ApJ, 321, 1031

Torii, C., Tsukiji, Y., Kobayashi, S., Yoshimi, N., Tanaka, H., Enome, S.,
1979, in Proc. of the Res. Inst. of Atmospherics, Nagoya Univ., 26, 129

Tsuneta, S., et al. 1991, Sol. Phys., 136, 37

Tsuneta, S., and Naito, T. 1998, ApJ, 495, L67

Chapter 7

Summaries and Discussions

We have analyzed, in the foregoing chapters, the dynamic features of solar flares by using various kinds of observational data and derived several new essential informations about energy release and particle acceleration during the flares, on the basis of a current magnetic reconnection model. In this chapter we present the summary of each previous chapter. Then, we discuss achievement and a new view, which this thesis brings, about energy release processes to answer the questions raised in §1.5 (Aim of This Thesis). Furthermore, we also discuss future directions.

7.1   Brief Summaries of Chapters

In this thesis we have discussed many topics about flares and flare-associated phenomena seen on the solar atmosphere. First, we again describe a summary of each chapter briefly, here.

Chapter 2 : Evolution of Conjugate Footpoints

We studied the temporal and spatial evolution of the fine structure inside the flare ribbons with a new method in a solar flare which occurred on 2001 April 10. We identified the conjugate footpoints in both the flare ribbons with different magnetic polarities by calculating cross-correlation functions of the light curves of each Hα kernel. Using the Hα images obtained with the Sartorius, we investigated the conjugate footpoints with higher spatial resolution than possible with hard X-ray (HXR) and microwave data. Second, we examined whether or not the pairs of Hα conjugate footpoints are really connected by the extreme ultraviolet (EUV) post-flare loops seen in the *TRACE* 171 Å images and found, for the first time, that almost all the Hα pairs are connected by the 171 Å loops.

Chapter 3 : Spatial Distribution in Solar Flare

We examined the difference between the spatial distributions of Hα kernels and HXR sources which were observed in the 2001 April 10 solar flare. The HXR sources indicate the sites where the large energy release which exceeds some threshold occurred, while the Hα kernels show most of precipitation sites of nonthermal electrons with higher spatial resolution. We measured the photospheric magnetic field strength at each Hα kernel, and found that the magnetic field strengths at the Hα kernels accompanied by HXR sources are about 3 times higher than those at the other Hα kernels which are not accompanied by any HXR sources.

Chapter 4 : Flare Ribbon Expansion and Energy Release

We examined the relation between the evolution of the Hα flare ribbons and the released magnetic energy during a solar flare which occurred on 2001 April 10, and quantitatively showed that the magnetic reconnection model is consistent with the observed variations of Hα, HXR, and microwave emissions. In addition to the photospheric magnetic field strength B_p of each Hα kernel, by measuring the separation speed of the Hα flare ribbons from the magnetic neutral line v_f, we estimated the energy release rate, based on the magnetic reconnection model. We calculated $B_p v_f$ and $(4\pi)^{-1}B_p^2 v_f$, as the reconnection rate ($\dot{\Phi}$) and the Poynting flux (S), respectively. Both $\dot{\Phi}$ and S of the HXR sources are much stronger than those of the Hα kernels without HXR sources. The estimated energy release rates of the Hα kernels associated with the HXR sources are locally large enough to explain the difference between the spatial distribution of the Hα kernels and the HXR sources. The temporal evolution of the energy release rates also shows peaks corresponding to the HXR bursts.

Chapter 5 : Downflow Motions Associated with Inpulsive Nonthermal Bursts

We examined the evolution of a big two-ribbon flare which occurred on 2002 July 23, and found downflows above the post-flare loops. Those downflows were seen not only in the decay phase, but also in the impulsive and main phases.Furthermore, they correspond to the times when nonthermal bursts in microwaves and HXRs occurred. This result implies that the downflow motions occurred when strong magnetic energy was released, and suggests that they are correlated with reconnection outflows. Thus, we have been able to add a new piece of observational evidence to the model that downflows are reconnection outflow (McKenzie and Hudson 1999; McKenzie 2000).

Chapter 6 : Periodic Acceleration of Electrons

We investigated the impulsive phase of the flare which occurred on 1998 November 10. We found that the time evolution showed a clear quasi-periodic pulsation (QPP) in microwaves and hard X-rays. We also found that the periods of the QPP were 6.6 s by using correlation analysis of the time profiles. The HXR and SXR data of the flare indicate that the acceleration site of nonthermal electrons was located near one of two microwave sources. Then, we estimated some typical timescales of the flare loop from the observational data and found that the Alfvén transit time along the flare loop was close to the period of the pulsation.

7.2 Discussions and Answers for Questions

In this thesis we have demonstrated new informations and new explanations found for the evolutional characteristics of flares, by analyzing various kinds of observational data. Those new findings are all consistent with the magnetic field reconnection model. Here, we discuss what are achieved in this thesis and how they should be developed more, and answer each question raised in §1.4.

7.2.1 Magnetic Reconnection and Energy Release

Question 1 : Can conjugate system be identified in a huge complex flare?

The idea that flares consist of Hα conjugate kernels which show correlated time profiles and that flare loops connect those conjugate footpoints is first proved in this thesis. The Hα kernels are brightened by the precipitation of high-energy electrons or by heat conduction caused by energy release which occurred at somewhere in the flare loop (near apex of the loop) with magnetic reconnection. The flare loops are filled with evaporated plasma from the Hα kernels and become visible in SXR and in EUV radiation.

We applied this idea to a large two-ribbon flare which occurred on 2001 April 10, and successfully identified such conjugate or highly correlated pairs of Hα kernels. Our result clearly confirmed the scenario of two-ribbon flare mentioned above, and suggests that each element of a two-ribbon flare is fairly simple, even though the flare has very complex structure as a whole. Moreover, we could study the magnetic field configuration in the energy release sites by examining evolution of Hα kernels. We could follow the formation of the flare loops and the evolution of energy release sites.

Question 2 : Can we estimate energy release rate quantitatively which explain observed variations of emission sources?

Next, we could first succeed to give a reasonable explanation to a puzzling question that the spatial distribution of the HXR emission sources is very different from that of Hα kernels in a flare. Although there are many pairs of the conjugate footpoints in the two-ribbon flare, we can identify only one pair of Hα kernels, which corresponds to the HXR sources. As is already described in Chapter 3 and 4, especially strong energy release occurred on the flare loop which connects the special Hα conjugate footpoints. In the HXR images, only the strongest sources are seen, and the other weaker sources are buried in the noise, due to the low dynamic range (~ 10). Therefore, if the released energy at the Hα kernels associated *with* the HXR sources is at least 10 times larger than that at the Hα kernels the *without* HXR sources, then the difference of appearance can be reasonably explained. If the amount of the released energy is comparable in all the pair, HXR emission sources do not appear point-like but ribbon-like as seen in Hα (Masuda, Kosugi, & Hudson 2002).

Moreover, in Chapter 4 we estimated the energy release rates at each Hα kernels by measuring observable physical parameters, such as separation speeds of the fronts of the Hα flare ribbons and the photospheric magnetic field strengths. We first succeeded in reconstructing the observed flux variations of HXR and microwave emissions in detail by using the estimated energy release rates. The estimated energy release rates in the Hα kernels associated with the HXR sources are locally large enough to explain the difference between the spatial distribution of the Hα kernels and the HXR sources. Those energy release rates are estimated on the basis of the magnetic reconnection model, and it means that the observational data also support the model.

Further questions

Although we successfully identified the Hα conjugate footpoints and derived the informations about energy release, there remain some problems.

In Chapter 2 we did not identify the pairs of the Hα conjugate regions, but those of highly correlated compact points (the boxes of the meshes). Elemental Hα kernels, which are considered to be about $1''$ or even smaller (Kurokawa 1986), are not resolved in our data. Although we could follow the essential characteristics of structures inside the flare ribbons even in our work, to identify conjugate footpoints accurately, it is needed to use data with higher spatial resolution, e.g., those that will be obtained with SMART which has been just equipped at Hida Observatory and the next-generation satellite, Solar-B. We hope that those new instruments will confirm our results in more

detail.

In Chapter 4 we estimated the energy release rate by assuming that B_c is proportional to B_p with a constant ratio. Despite these simple assumptions, we were able to reconstruct well the behavior of the impulsive energy release seen in the microwave and HXR light curves. These assumptions, however, are reasonable only within a narrow region, and more detailed analyses are needed to extend our discussion to the whole flare region in future works.

7.2.2 Downflows and Plasmoid Ejections

Question 3 : What is a characteristic of reconnection outflows?

In Chapter 5 we also found other flare-associated phenomena, "downflow", which are associated with non-steady energy release and also strongly support the magnetic reconnection model. Nonthermal emission which is detected in HXRs and in microwaves, shows some bursts in the light curves during the impulsive phase of a flare. The bursts sometimes appear intermittently or periodically. Since nonthermal emission is thought to be related with strong energy release, this feature implies that energy release occurs dynamically and non-steady in a flare.

Further developments

We found downflow motions and plasmoid ejections which are associated with each of the bursts of nonthermal emission. As Shibata et al. (1995) suggested, plasmoid plays an important role in magnetic reconnection, since it regulates the thickness of current sheet and then efficiency of magnetic reconnection. Recently, H. Takasaki (in private communication) found multiple X-ray plasmoid ejections which were associated with the 2000 November 24 flare as mentioned in Chapter 5. He reported that each of the ejections appears at a time corresponding to each HXR peak in the impulsive HXR emission. From these results, we supposed that both the downflows and the plasmoid ejections are reconnection outflows. Moreover, these results support the model that downflow/plasmoid ejection is strongly related with magnetic reconnection mechanism. Plasmoids are generated in the current sheet, and are ejected as downward (downflows) and upward (plasmoid ejections), when strong energy releases occur. Therefore, the correlations between plasmoid ejections, or downflows, and HXR bursts represent a plasmoid-induced, non-steady reconnection (Shibata 1999; Shibata & Tanuma 2001).

7.2.3   Energy Release and Particle Acceleration

Question 4 : How does a global flare structure affect periodic particle acceleration?

We found QPP in microwaves and HXRs in a flare (Chap. 6). We proposed, under the hypothesis of the acceleration model proposed by Tsuneta and Naito (1998), that the origin of the QPP in microwaves and HXRs is the modulation of the acceleration/injection of nonthermal electrons. Moreover, we proposed that the modulation is produced by the variations of macroscopic magnetic structures, for example, oscillations of coronal loops. This work is unique and important since we found the relationship between the efficiency of particle acceleration and the global structure of magnetic field.

Further developments

This result strongly contributes to a new field in the solar physics, called "coronal seismology". Coronal seismology is an efficient new tool that uses standing MHD waves and oscillations as a tool to explore the physical parameters of the solar corona. There are three basic branches of solutions of the dispersion relation for propagating and standing MHD waves: the slow mode branch (with acoustic phase speeds), the fast mode branch and the Alfvén branch (with Alfvénic phase speeds). Furthermore, each branch has a symmetric and asymmetric solution, termed the sausage and kink mode (Roberts et al. 1984). Nakariakov, Melnikov, & Reznikova (2003) and Aschwanden, Nakariakov, & Melnikov (2003) suggest that the QPP is possibly a fast sausage-mode oscillations. On the other hand, we suggest that transverse Alfvénic kink-mode oscillations like observed with *TRACE* (Aschwanden et al. 1999; Nakariakov et al. 1999) associated with Tsuneta and Naito (1998)'s model is better to explain particle acceleration mechanism. If we are able to fix which mode is dominant to generate the QPP, we can derive physical condition in the corona and set up some limits on the particle acceleration mechanism.

7.3   Future Directions

Although we have successfully derived new informations to solve the energy release mechanism of solar flares in this thesis, there still remain many problems to be clarified. Here, we discuss some of those problems and the prospects of the future works.

(a) Energy Release Mechanism

We estimated the released magnetic energy by using the photospheric and the chromospheric features. As a next stage of the work, we have to compare them with energy loss which is measured by SXR radiation. Isobe et al. (2002) examined energy budget by estimating thermal energy derived by SXR emission during a decay phase of a flare. We need apply this method to each flare loop. As we showed in Chapter 2, 3, and 4, each Hα kernel in flare ribbons shows different photospheric magnetic field strength and separation speed, and therefore, the structure is very complex. Therefore, the amount of the energy loss by radiative cooling in an ideal condition must be calculated for each loop separately. The derived energy loss rate is to be compared with the released energy rate at each Hα kernel. Numerical simulations on flare loop, as many solar theoretician performed (e.g., Hori, et al. 1997) are also a powerful tool to examine the evolution of physical conditions in flare loops. We should try to compare such numerical results with the observed values in details.

(b) Plasmoid-Induced Reconnection

Are downflows really plasmoids ejected downward as we suggest, or a feature caused by some waves as others suggest (e.g., V. M. Nakariakov, in private communication)? To answer this question, we have to examine the mechanism and the process of magnetic reconnection and the relationship between the reconnection outflow and the downflow in much more detail. More numerical simulations based on reconnection model are necessary. They must be consistent with all the features of the downflows, such as low density, high Doppler-shift, and relationship with the bursts of nonthermal emission. Recently, Tanuma et al. (2001) has performed numerical simulations of magnetic reconnection, and have shown that fractal plasmoids generated in the current sheet are ejected bidirectionally, which resembles the downflow motions. Furthermore, TanDokoro & Fujimoto (2004) have examined the instability at the leading edge of a reconnection jet in their new numerical simulations. The reconstructed leading edge of the jet is a narrow and elongated structure, and is similar to the shape of the downflows. These works may help to explain what downflows are.

On the observational point of view, the relationship between downflows and X-ray plasmoid ejection also must be examined to discuss the plasmoid-induced, non-steady features of magnetic reconnection. We need to investigate in detail the events with which both X-ray plasmoid ejection and downflows are associated.

(c) Particle Acceleration

Particle acceleration is one of the most important and difficult problems not only in the solar physics but also in the plasma physics. We challenge this topic by examining the relationship with the global structure of a flare. The solar physics has a great advantage in such a way of research as a natural laboratory of magnetized plasma. Problems about particle acceleration mechanisms in solar flares have mainly been discussed with HXR and microwave data. In addition to those data, we examine the non-steady nature of magnetic reconnection, such as downflow motions and plasmoid ejections. Then, we need to follow behavior of particles in such a non-steady situation, by using numerical simulations.

Moreover, the study of QPP tells us some hints to solve particle acceleration mechanism. QPP implies that the efficiency of particle acceleration depends on the global magnetic field structure. As mentioned in the previous section, there are some models for the explanation of QPP. We need to perform numerical simulations based on each model, and test those models by comparing with the observational data.

The energy transfer mechanism is closely related to the particle acceleration mechanism. We also have to learn from features of Hα radiation during flares more. Hα impact polarization (Vogt and Hénoux 1996) and spectroscopic studies of Hα kernels should our understanding the particle acceleration mechanism.

(d) Energy-Input Process and Trigger of Flare

In this thesis we have discussed the energy release mechanism associated with magnetic reconnection. However, we also have to examine the mechanism of energy storage and the flare-triggering process. Such an evolution of flare loops as examined in Chapter 2 indicates that the configuration of a height-dependent sheared magnetic field had been formed in the corona over the magnetic neutral lines before the flare. In other words, the large and less-sheared configuration of magnetic field lies over the inner sheared magnetic structure. It may be caused by the emergence of tightly twisted flux tubes and their relaxations (Ishii, Kurokawa, & Takeuchi 2000).

Although some theories argue that magnetic helicity plays an important role in the flare onset (e.g., Kusano, Suzuki, & Nishikawa 1995), it is difficult to directly measure the magnetic helicity of the coronal field, because the measurable field is restricted only to the photosphere and the chromosphere. Recently, Kusano et al. (2002) established the new method to measure the "magnetic helicity injection", which became a powerful tool to examine the

stored magnetic energy in the corona. With this method, Kusano et al. (2004) found that initial brightening appears on the helicity inversion layer in the pre-flare phase. They also reported that the formation of two-ribbon structure in the main phase is related with the helicity inversion layers. We need to apply this method to other cases, and examine, in more detail, the relationship between magnetic helicity injection and sign of flare initiation, such as filament eruption. If we know the storage process of magnetic energy and the mechanism of flare triggering, then we will be able to predict the occurrence of the events. The studies about the magnetic structures and their formations will bring us the basic understandings of the solar-terrestrial environment, which contributes to the new field, space whether research.

Bibliography

Aschwanden, M. J., Fletcher, L., Schrijver, C. J., and Alexander, D. 1999, ApJ, 520, 880

Aschwanden, M. J., Nakariakov, V. M., and Melnikov, V. F. 2004, ApJ, 600, 458

Hori, K., Yokoyama, T., Kosugi, T., Shibata, K. 1997, ApJ, 489, 426

Ishii, T. T., Kurokawa, H., Takeuchi, T. T. 2000, PASJ, 52, 337

Isobe, H., Yokoyama, T., Shimojo, M., Morimoto, T., Kozu, H., Eto, S., Narukage, N., Shibata, K. 2002, ApJ, 566, 528

Kurokawa, H. 1986, the Low Atmosphere of Solar Flares; Proc. of NSO/SMM Flare Symp., ed. D. Neidig, 51

Kusano, K., Suzuki, Y., Nishikawa, K. 1995, ApJ, 441, 942

Kusano, K., Maeshiro, T., Yokoyama, T., Sakurai, T. 2002, ApJ, 577, 501

Masuda, S., Kosugi, T., Hudson, H. S. 2001, Sol. Phys., 204, 57

McKenzie, D. E. & Hudson, H. S. 1999, ApJ, 519, L93

McKenzie, D. E., 2000, Sol. Phys., 195, 381

Nakariakov, V. M., Ofman, L., DeLuca, E. E., Roberts, B., & Davila, J. M. 1999, Science, 285, 862

Nakariakov, V. M., Malnikov, V. F., and Reznikova, V. E. 2003, A&A, 412, L7

Parker, E. N. 1957, J. Geophys. Res., 62, 509

Petschek, H. E. 1964, in AAS-NASA Symp. on Solar Flares, ed. W. N. Hess (NASA SP-50), 425

Roberts, B., Edwin, P. M., & Benz, A. O. 1984, ApJ, 279, 857

Shibata, K., Masuda, S., Shimojo, M., Hara, H., Yokoyama, T., Tsuneta, S.,
    Kosugi, T., Ogawara, Y. 1995, ApJ, 451, L83

Shibata, K. 1999, Ap&SS, 264, 129

Shibata, K., Tanuma, S. 2001, Earth Planets Space, 53, 473

Sweet, P. A. 1958, in IAU Symp. 6, Electromagnetic Phenomena in Cosmical
    Physics, ed. B. Lehnert (Cambridge: Cambridge University Press), 123

TanDokoro, R., Fujimoto, M. 2004, Adv. Space Res, in press

Tanuma, S., Yokoyama, T., Kudoh, T., Shibata, K. 2001, ApJ, 551, 312

Tsuneta, S., and Naito, T. 1998, ApJ, 495, L67

Vogt, E., Hénoux, J.-C. 1996, Sol. Phys., 164, 345

Appendix A

Summary of Instruments

In this thesis we used a lot of observational data, which were obtained at various wavelengths both with ground-based and with space-based instruments. By examining the appearances of active regions and flares in the photosphere, the chromosphere, and the corona, which are observed with these instruments, we derived information about the energy release during flares. Here, we summarize the instruments and their characteristics, which we mainly used in the thesis, and/or which are related to our studies.

A.1 Ground-Based Instruments

With ground-based observations, we can observe the sun with high time cadence and high spatial resolution. We mainly used the Hα images which are obtained in the Kwasan and Hida Observatories, Kyoto University.

A.1.1 Kwasan and Hida Observatories, Kyoto University

Sartorius Telescope; Sartorius

The Sartorius 18 cm Refractor (Sartorius; Fig. A.1) at Kwasan Observatory is the oldest telescope among those which are actively working at Kyoto University. It was first installed at the campus of Kyoto University in 1910, and settled at Kwasan Observatory in 1929.

Hα monochromatic images of flares are obtained with a Halle Lyot filter of 0.5 Å bandwidth in the Hα line center. A Kodak 1.6i Megaplus CCD Camera was equipped in 1994. The pixel size of the CCD is 9 μm and corresponds
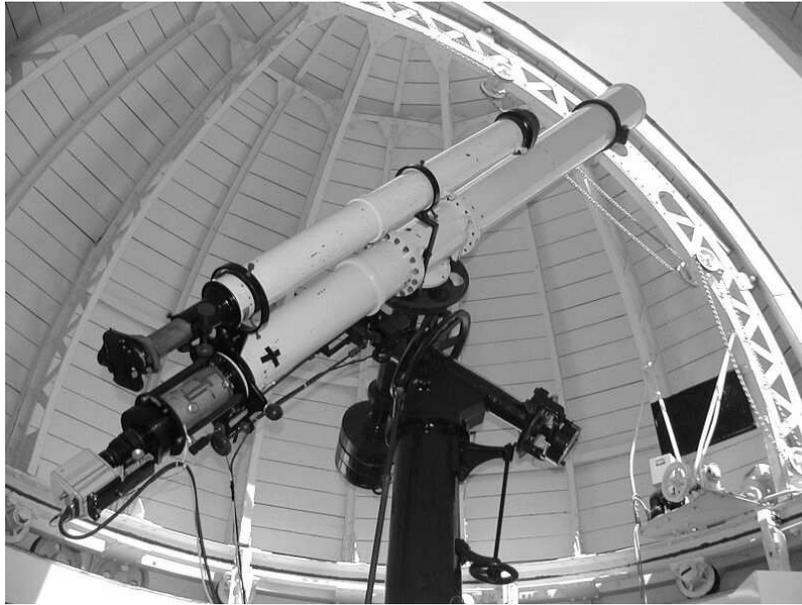
Figure A.1: The Sartorius 18 cm Refractor (Sartorius) in Kwasan Observatory, Kyoto University.
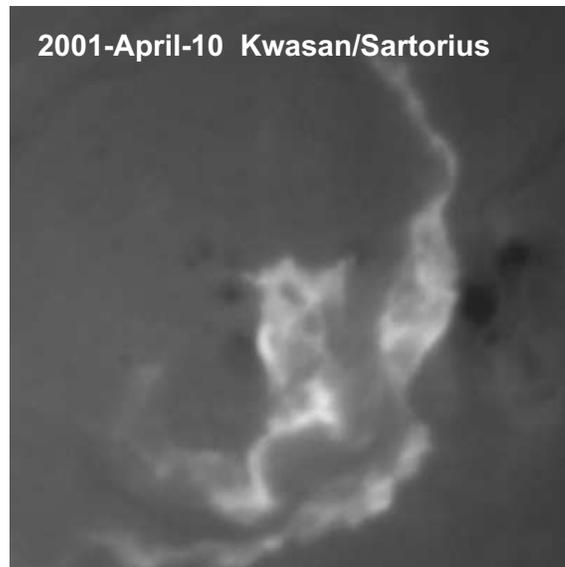

Figure A.2: An image obtained with Sartorius.

to about $0''\!.6$, and partial images of the sun (FOV[1] $\sim 850'' \times 570''$, which covers one-third of the diameter of the sun on each side) were taken. From 2002, with a new Kodak $4.2i$ Megaplus CCD with a pixel size of about $1''\!.1$, full-solar images (FOV $\sim 2200'' \times 2200''$) are taken. The spatial resolution is about $2''$. The temporal resolution of the Sartorius data is 1 minute in routine observations, and in the case of a flare it is about 1 s at the highest cadence. Figure A.2 shows an Hα image taken with Sartorius.

Sartorius can obtain Hα images with a relatively wide FOV and high time cadence. Moreover, the data coverage is fairly high. We used the Sartorius Hα data for some studies in this thesis; the study about evolution of conjugate footpoints (Chap. 2; Asai et al. 2003), the study about spatial distribution in solar flare (Chap. 3; Asai et al. 2002) the study about flare ribbon expansion and energy release rate (Chap. 4).

Domeless Solar Telescope; DST

The Domeless Solar Telescope (DST; Fig. A.3) was built at Hida Observatory, Kyoto University in 1979. It is a Grégorian-Coudé vacuum telescope with a 60 cm main mirror installed at the top of an 18 m tower. It has two spectrographs, namely the vertical and horizontal spectrographs. Hα monochromatic images of high spatial resolution are obtained with a Zeiss Lyot filter of 0.25 Å passband which is equipped at the focal plane of the vertical spectrograph.

Until 2000, the DST Hα data were obtained with a SONY laservideo disc recorder sequentially in 3 wavelengths: H$\alpha \pm 0.0$ Å, $+0.6$ Å, and -0.6 Å. The successive wavelength-change and recording were controlled with a personal computer, and the time cadence for each wavelength was about 12 s. In 2000 a new Kodak $4.2i$ Megaplus CCD with a pixel size of about $0''\!.14$ was equipped. The FOV is about $280'' \times 280''$. The successive wavelength-change and recording are controlled by a personal computer. The temporal resolution depends on the number of wavelengths used for the observation, and is about 20 s for 5 wavelengths. Figure A.4 shows Hα images of a solar flare which occurred on 2001 April 10 obtained with DST in 6 wavelengths: H$\alpha \pm 0.0$ Å, -0.4 Å, -0.8 Å, $+0.4$ Å, $+0.8$ Å, and $+5.0$ Å.

The most remarkable characteristic of the DST data is its high spatial resolution. We can examine fine chromospheric structure with sub-arcsecond sizes. We examined small jet-like plasma motions (called "Hα surge"; see Chap. 1. and 2.), ejected from a light bridge of a stable and mature sunspot (Asai et al. 2001a).

---

[1]Field Of View

Figure A.3: The 60 cm Domeless Solar Telescope (DST) at Hida Observatory, Kyoto University.
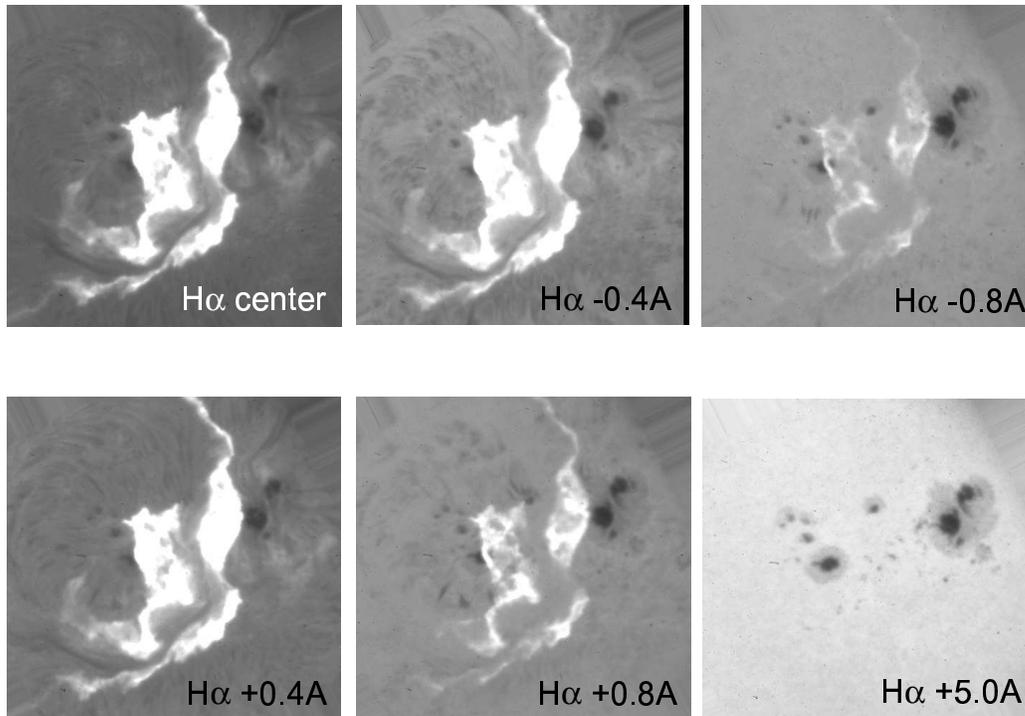
Figure A.4: Hα images of a solar flare which occurred on 2001 April 10 obtained with DST. These images are taken in different 6 wavelengths: Hα ± 0.0 Å, −0.4 Å, −0.8 Å, +0.4 Å, +0.8 Å, and +5.0 Å.

Flare Monitoring Telescope; FMT

The Flare Monitoring Telescope (FMT; Kurokawa et al. 1995) was built in 1992 at Hida Observatory of Kyoto University. Figure A.5 shows outside- and inside-views of the FMT. The FMT observes four full disk images in Hα center, Hα +0.8 Å, Hα -0.8 Å, and continuum, and one solar limb image in Hα center. These FMT images are successively stored in a hard disc on a personal computer with a time resolution of 1 min, while they are also captured every 2 seconds with five video recorders, simultaneously.

FMT monitors the whole sun, and the data coverage is quite high. The full-disk and multi-wavelength observations provide a great advantage for examining plasma motions such as filament eruptions (Morimoto & Kurokawa 2003a, 2003b). Furthermore, FMT observes a lot of Moreton waves (Moreton 1960; 1961) associated with solar flares (Eto et al. 2002; Narukage et al. 2002). Examples of the images taken with FMT are shown in Figure 1.7.
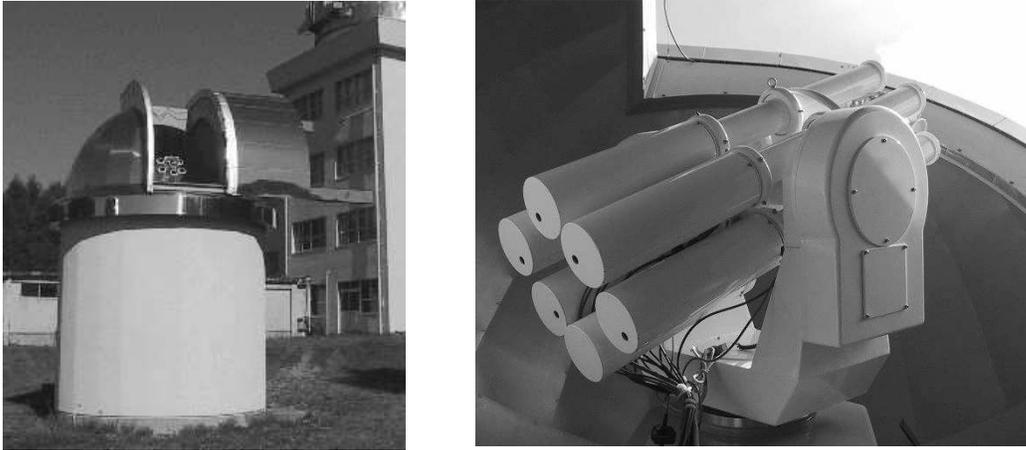
Figure A.5: Flare Monitoring Telescope (FMT) at Hida Observatory, Kyoto University. *Left*: Outside view. *Right*: Inside view.

Solar Magnetic Activity Research Telescope; SMART

The Solar Magnetic Activity Research Telescope (SMART) was newly installed at Hida Observatory, Kyoto University in 2003 (Fig. A.6). This telescope consists of 4 refractors; two with 25 cm and two 20 cm diameter.

SMART aims to monitor the full-disk sun, such as FMT does, with much higher spatial resolution than FMT. Furthermore, SMART takes full-disk Hα images and vector magnetograms simultaneously. This may allow us to follow the development of magnetic fields, such as evolution of sunspots, distortion of magnetic field before flares, and we can derive important information about the storage and release of magnetic energy in active regions. We present an Hα image taken with SMART in Figure 1.4.

Figure A.6: Solar Magnetic Activity Research Telescope (SMART) at Hida Observatory, Kyoto University.

A.1.2 Other Ground-Based Instruments in Japan

Nobeyama Radioheliograph; NoRH

Nobeyama Radioheliograph [2] (NoRH; Nakajima et al. 1994) is a radio interferometer built in 1992 at Nobeyama Solar Observatory, National Astronomical Observatory of Japan (NAOJ). As shown in Figure A.7, the telescope consists of 84 parabolic antennas with 80 cm diameter. NoRH observes the sun at 17 GHz (right and left circular polarization) and 34 GHz (only intensity) with a temporal resolution of 1.0 s during event mode. The spatial resolutions of NoRH data are $12''$ for 17 GHz and $6''$ for 34 GHz.

Since NoRH is less affected by weather, it has quite good data coverage. Furthermore, it observes the sun with quite high spatial resolution in the microwave range. In Chapter 6 (Asai et al. 2001b) we used the microwave data obtained with NoRH, and examined features of quasi-periodic emission at each spatially resolved microwave source in the 1998 November 10 solar flare.

Nobeyama Radio Polarimeter; NoRP

The Nobeyama Radio Polarimeter[3] (NoRP; Fig. A.8) is a multiple frequency telescope in Nobeyama Solar Observatory, NAOJ (Torii et al. 1979; Shibasaki et al. 1979; Nakajima et al. 1985). It measures the total flux of the flare at 1, 2, 3.75, 9.4, 17, 34, and 80 GHz with a temporal resolution of 0.1 s. In the study of microwave quasi-periodic emission (Chap. 6) we also used the NoRP data with high time cadence.

Solar Flare Telescope

The Solar Flare Telescope [4] (SFT; Fig A.9) was built at the Mitaka, National Astronomical Observatory of Japan (Sakurai et al. 1995), in order to observe the distortion and subsequent relaxation of magnetic fields. SFT is equipped with four telescopes (two with 15cm and two with 20cm aperture). These telescopes observe magnetic fields, velocity fields, sunspot structures, and flares in Hα light. Since SFT monitors the sun, and takes vector magnetograms and Hα images constantly, it provides a great advantage for following the development of magnetic distortion which may lead to flares.

We used vector magnetograms to measure the magnetic helicity injection into active region NOAA 9415 before the 2001 April 10 flare occurred.

---

[2]URL: http://solar.nro.nao.ac.jp/norh/
[3]URL: http://solar.nro.nao.ac.jp/norp/
[4]URL: http://solarwww.mtk.nao.ac.jp/en/flaretel.html

Figure A.7: Nobeyama Radioheliograph (NoRH) at Nobeyama Radio Observatory, NAOJ.
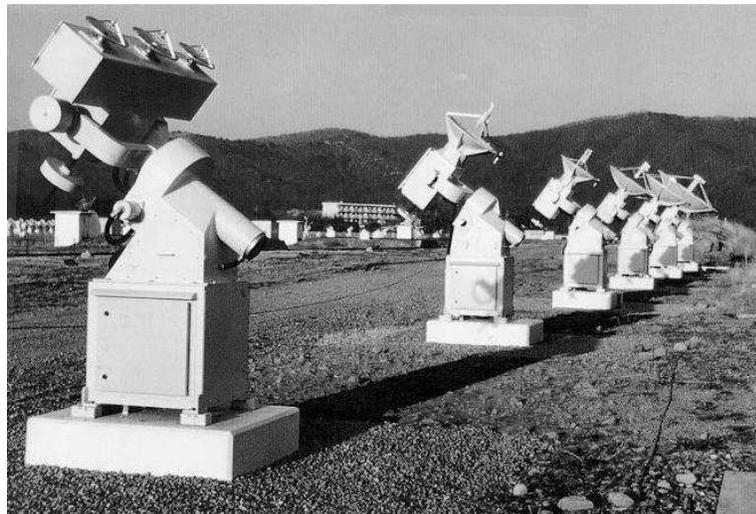
Figure A.8: Nobeyama Radio Polarimeter (NoRP) at Nobeyama Radio Observatory, NAOJ.

Figure A.9: Solar Flare Telescope (SFT) in Mitaka, National Astronomical Observatory of Japan.

A.2   Space-Based Instruments

With ground-based observation, we mainly observed the optical light in which emissions from the photosphere and the chromosphere dominate. On the other hand, the solar corona is filled with higher temperature plasma. This plasma is usually about 2 MK but sometimes reaches 50 MK during flares. Such plasma radiates in soft and hard X-ray, and γ-ray ranges, which are blocked by the earth's atmosphere and cannot arrive at the ground. Furthermore, observations from space can avoid the effects of the earth's atmosphere, and can obtain seeing-free images.

A.2.1   *Yohkoh*

The *Yohkoh* satellite[5] (Fig. A.10; Ogawara et al. 1991), an observatory for studying X-rays and γ-rays from the Sun, was launched in August 1991, and operated for over 10 years until December 2001. *Yohkoh* is a project of the Institute for Space and Astronautical Sciences, Japan (ISAS[6]). *Yohkoh*

---

[5]URL: http://isass1.solar.isas.ac.jp/
[6]Now, Japan Aerospace Exploration Agency; JAXA
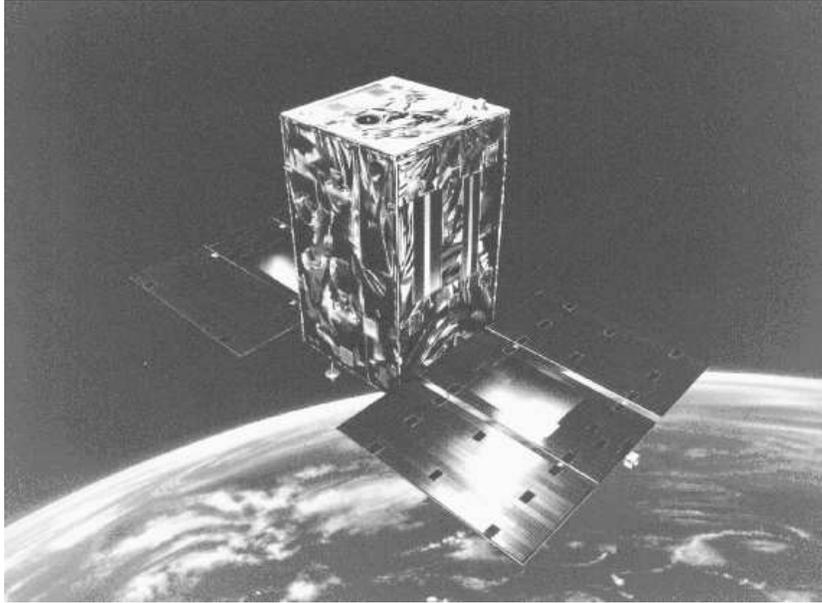
Figure A.10: *Yohkoh* satellite.

was built in Japan, and it was completed as an international collaboration with the US and UK. The *Yohkoh* spacecraft has four instruments: a Bragg Crystal Spectrometer (BCS), a Hard X-ray Telescope (HXT), a Soft X-ray Telescope (SXT), and a Wide Band Spectrometer (WBS). This combination of simultaneous hard and soft X-ray imaging from the SXT and the HXT with spectroscopy from the BCS and WBS, made *Yohkoh* a unique and powerful tool for studying the Sun in X-rays and γ-rays.

Yohkoh found a lot of interesting phenomena on the solar corona, and revealed that the solar corona is really dynamic. These findings provided us with hints to solve problems such as magnetic reconnection in solar flares, particle acceleration associated with flares, and coronal heating.

Soft X-ray Telescope (SXT)

The Soft X-ray Telescope (SXT; Tsuneta et al. 1991) observed the sun in the 0.25 to 4.0 keV range by using glancing incidence mirrors to form soft X-ray images of the sun on a CCD detector.

The highest spatial resolution is about $2''.5$ in full-resolution images in the partial frame image mode, and the temporal resolution is about 10 s. A selection of thin metallic filters located near the focal plane provides the capability to separate the different X-ray energies for plasma temperature di-

agnostics. Therefore, we used SXT data to examine high temperature plasma inside post-flare loops and to measure the thermal energy quantitatively in the 1998 November 10 flare (Chap. 6, Asai et al. 2001b).

Hard X-ray Telescope (HXT)

The hard X-ray telescope (HXT; Kosugi et al. 1991) is a Fourier synthesis type imager consisting of 64 bi-grid modulation subcollimators (SC's). Each SC has a different pitch and/or a position angle of collimator grids. Count rate data obtained by each detector equipped behind each SC can be regarded as a spatial Fourier component of a hard X-ray image. Hard X-ray images can be synthesized by using image restoration procedures such as the Maximum Entropy Method (MEM).

When a flare-mode is triggered, a set of 64 hard X-ray count rate data are recorded every 0.5 s (= the highest temporal resolution) in four energy bands between 14 and 93 keV (L, M1, M2, and H bands, respectively). The FOV of HXT is about $35'$ by $35'$. The basic image synthesis FOV of HXT is $2'.1$ by $2'.1$ with the angular resolution as high as approximately $5''$. We used the HXT data to examine where and when large energy release occurred in the 2001 April 10 flare (Chap. 3 and 4, Asai et al. 2002).

A.2.2 *TRACE*

The *Transition Region and Coronal Explorer* [7] (*TRACE*; Fig. A.11a; Handy et al. 1999; Schrijver et al. 1999) is a NASA [8] mission to image the solar corona and transition region with high spatial and temporal resolution. *TRACE* was launched in April 1998. *TRACE* observes the sun in the extreme ultraviolet (EUV) range, mainly in Fe IX/X 171 Å and Fe XII 195 Å, and in the ultraviolet (UV) range, e.g., around 1600 Å, with a highest spatial resolution of $0''.5$ and a temporal resolution of about 10 s.

TRACE enables us to study the connections between fine-scale magnetic fields and the associated plasma structures on the Sun in a quantitative way by observing the photosphere, the transition region, and the corona. As we showed in Figure 2.2 and 2.5, we can examine post-flare loops which connect conjugate footpoints with high spatial resolution (see Chap. 2).

---

[7]URL: http://vestige.lmsal.com/TRACE/
[8]National Aeronautics and Space Administration

A.2.3 *SOHO*

The *Solar and Heliospheric Observatory*[9] (*SOHO*; Fig. A.11b; Scherrer et al. 1995) is a continuing mission which is being carried out by ESA[10] and NASA as a cooperative effort between the two agencies. *SOHO* was launched in December 1995. NASA was responsible for the launch and is now responsible for mission operations. Mission control is based at Goddard Space Flight Center in Maryland. 12 main instruments are equipped on *SOHO*, and 6 of them are for the observation of the solar atmosphere; Coronal Diagnostic Spectrometer (CDS), Extreme ultraviolet Imaging Telescope (EIT), Large Angle and Spectrometric Coronagraph (LASCO), Michelson Doppler Imager (MDI), Solar Ultraviolet Measurements of Emitted Radiation (SUMER), and Ultraviolet Coronagraph Spectrometer (UVCS).

MDI

With the Michelson Doppler Imager (MDI; Domingo, Fleck, and Poland 1995) we can obtain the line-of-sight component of the magnetic field. The temporal resolution is 96 min in routine observation, but 1 min in campaign observations. In full-disk mode each magnetogram consists of 1024×1024 pixels with a pixel size of about $2''$, while in high-resolution mode each magnetogram consists of 1024×1024 pixels with a pixel size of about $0''6$. In Figure 3.2 we show a magnetogram obtained with MDI. The white region shows the positive magnetic polarity, and the black one shows the negative magnetic polarity.

A.2.4 *RHESSI*

The *Reuven Ramaty High Energy Solar Spectroscopic Imager* [11] (*RHESSI*; Lin et al. 2002) was launched in February 2002 to observe the sun in the hard X-ray and γ-ray ranges (Fig. A.11c). *RHESSI* is a NASA mission, and its primary aim is to explore the basic physics of particle acceleration and explosive energy release in solar flares.

We used the *RHESSI* data in the study about the relationship between downflow motions and energy release (see Chap. 5). An example of the image taken with *RHESSI* is shown in Figure 1.12.

---

[9]URL: http://sohowww.nascom.nasa.gov/
[10]European Space Agency
[11]URL: http://hesperia.gsfc.nasa.gov/hessi/
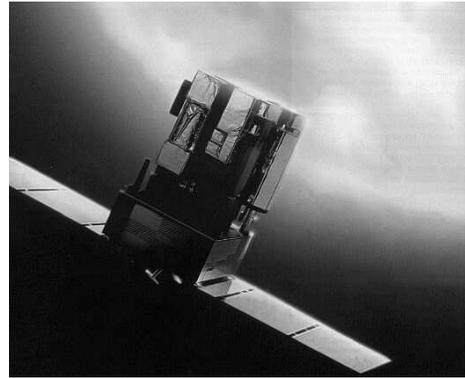
(a) TRACE

(b) SOHO

(c) RHESSI

(d) Solar-B

Figure A.11: Space crafts for solar observations. (a). *Transition Region and Coronal Explorer* (*TRACE*). (b). *Solar and Heliospheric Observatory* (*SOHO*). (c). *Reuven Ramaty High Energy Solar Spectroscopic Imager* (*RHESSI*). (d). Solar-B.

A.2.5 Solar-B

Solar-B[12] is an ISAS (now, JAXA) mission proposed as a follow-on to the highly successful Japan/US/UK *Yohkoh* (Solar-A) collaboration. Figure A.11d shows an image of the spacecraft. The mission consists of a coordinated set of optical, EUV and X-ray instruments to investigate the interaction between the Sun's magnetic field and its corona. The result will be an improved understanding of the mechanisms which give rise to solar magnetic variability and how this variability modulates the total solar output and creates the driving force behind space weather.

The spacecraft will be equipped with three major instruments: a 0.5m solar optical telescope (SOT), an X-ray telescope (XRT), and an EUV Imaging Spectrometer (EIS). The Solar-B spacecraft is scheduled for launch in August 2006. It will be placed in a sun-synchronous orbit around the Earth. This will keep the instruments in nearly continuous sunlight, with no day/night cycling for nine months each year.

---

[12]URL: http://solarwww.mtk.nao.ac.jp/solar-b/index_e.html

Bibliography

Asai, A., Ishii, T. T., Kurokawa, H. 2001a, ApJ, 555, L65

Asai, A., Shimojo, M., Isobe, H., Morimoto, T., Yokoyama, T., Shibasaki, K., Nakajima, H. 2001b, ApJ, 562, L103

Asai, A., Ishii, T. T., Kurokawa, H., Yokoyama, T., and Shimojo, M. 2002, ApJ, 578, L91

Asai, A., Ishii, T. T., Kurokawa, H., Yokoyama, T., and Shimojo, M. 2003, ApJ, 586, 624

Domingo, V., Fleck, B., and Poland, A. I. 1995, Sol. Phys., 162, 1

Eto, S., et al. 2002, PASJ, 54, 481

Handy, B. N., et al. 1999, Sol. Phys., 187, 229

Kosugi, T., et al. 1991, Sol. Phys., 136, 17

Kurokawa, H., Ishiura, K., Kimura, G., Nakai, Y., Kitai, R., Funakoshi, Y., and Shinkawa, T. 1995, J.Geomag.Geoelectr., 47, 1043

Lin, R. P., et al. 2002, Sol. Phys., 210, 3

Moreton, G. E. 1960, AJ, 65, 494

Moreton, G. E. 1961, Sky and Telescope, 21, 145

Morimoto, H. & Kurokawa, H. 2003a, PASJ, 55, 505

Morimoto, H. & Kurokawa, H. 2003b, PASJ, 55, 1141

Nakajima, H., et al. 1985, PASJ, 37, 163

Nakajima, H., et al. 1994, in Proc. of the IEEE, 82, 705

Narukage, N., Hudson, H. S., Morimoto, T., Akiyama, S., Kitai, R., Kurokawa, H., Shibata, K. 2002, ApJ, 572, L109

Ogawara, Y., Takano, T., Kato, T., Kosugi, T., Tsuneta, S., Watanabe, T., Kondo, I., & Uchida, Y. 1991, Sol. Phys., 136, 10

Sakurai, T., et al. 1995, PASJ, 47, 81

Scherrer, P. H., et al. 1995, Sol. Phys., 162, 129

Schrijver, C. J., et al. 1999, Sol. Phys., 187, 261

Shibasaki, K., Ishiguro, M., & Enome, S. 1979, in Proc. of the Res. Inst. of Atmospherics, Nagoya Univ., 26, 117

Torii, C., Tsukiji, Y., Kobayashi, S., Yoshimi, N., Tanaka, H., Enome, S. 1979, in Proc. of the Res. Inst. of Atmospherics, Nagoya Univ., 26, 129

Tsuneta, S., et al. 1991, Sol. Phys., 136, 37

Acknowledgements

My sincere appreciation goes to Ms. Kimata R., and all of my friends and colleagues. I really enjoyed chattering and discussing with them, and they have mentally supported me continuously. I thank all the members of Kwasan and Hida Observatories for wouderful discussions, which have made my Kwasan-life enjoyable very much. I would like to thank Takasaki H. for reminding me how difficult and important studying and teaching are.

I would like to thank my parents and sisters for their understandings and supports. Finally, I express my most sincere gratitude to Mr. Ichiki K. for his continuous encouragements and supports.

Publication

- Asai, A., Ishii, T.T., Kurokawa, H. 2001, *The Astrophysical Journal*, 555, L65
  "Plasma Ejections from a Light Bridge in a Sunspot Umbra"

- Asai, A., Shimojo, M., Isobe, H., Morimoto, T., Yokoyama, T., Shibasaki, K., Nakajima, H. 2001, *The Astrophysical Journal*, 562, L103
  "Periodic Acceleration of Electrons in the 1998 November 10 Solar Flare"

- Eto, S., Isobe, H., Narukage, N., Asai, A., Morimoto, T., Thompson, B.,
  Yashiro, S., Wang, T., Kitai, R., Kurokawa, H., Shibata, K. 2002, *Publications of the Astronomical Society of Japan*, 54, 481
  "Relation between a Moreton Wave and an EIT Wave Observed on 1997 November 4"

- Asai, A., Masuda, S., Yokoyama, T., Shimojo, M., Isobe, H., Kurokawa, H., Shibata, K. 2002, *The Astrophysical Journal*, 578, L91
  "Difference between Spatial Distribution of the Hα Kernels and Hard X-ray Sources in a Solar Flare"

- Asai, A., Masuda, S., Yokoyama, T., Shimojo, M., Kurokawa, H., Shibata, K., Ishii, T.T., Kitai R., Isobe, H., and Yaji, K. 2002, *in Multi-Wavelength Observations of Coronal Structure and Dynamics (COSPAR Colloquia Ser. 13)*, p.221
  "Fine Structure inside Flare Ribbons and its Temporal Evolution"

- Shibata, K., Eto, S., Narukage, N., Isobe, H., Morimoto, T., Kozu, H., Asai, A., Ishii, T.T., Akiyama, S., Ueno, S., Kitai, R., Kurokawa, H., Yashiro, S., Thompson, B., Wang, T., and Hudson, H.S. 2002, *in Multi-Wavelength Observations of Coronal Structure and Dynamics (COSPAR Colloquia Ser. 13)*, p.279
  "Observations of Moreton Waves and EIT Waves"

- Narukage, N., Shibata, K., Hudson, H.S., Eto, S., Isobe, H., <u>Asai, A.</u>, Morimoto, T., Kozu, H., Ishii, T.T., Akiyama, S., Kitai, R., and Kurokawa, H. 2002, *in Multi-Wavelength Observations of Coronal Structure and Dynamics (COSPAR Colloquia Ser. 13)*, p.295
  "Multi-Wavelength Observation of Moreton Wave on November 3, 1997"

- <u>Asai, A.</u>, Ishii, T.T., Kurokawa, H., Yokoyama, T., Shimojo, M. 2003, *The Astrophysical Journal*, 586, 624
  "Evolution of Conjugate Footpoints inside Flare Ribbons during a Great Two-Ribbon Flare on 2001 April 10"

- <u>Asai, A.</u>, Masuda, S., Yokoyama, T., Shimojo, M., Ishii, T.T., Isobe, H., Shibata, K., Kurokawa, H. 2003, *in The IAU 8th Asian-Pacific Regional Meeting* PS 5-1, p.415
  "Evolution of Flare Ribbons and Energy Release"

- <u>Asai, A.</u>, Masuda, S., Yokoyama, T., Shimojo, M., Kurokawa, H., Ishii, T.T., Shibata, K. 2003, *in The 34th COSPAR Scientific Assembly*, Adv. Space Res., vol.32, p.2561
  "Evolution of Flare Ribbons and Energy Release"

- <u>Asai, A.</u>, Yokoyama, T., Shimojo, M., Masuda, S., Kurokawa, H., Shibata, K. 2003, *in The 28th International Cosmic Ray Conference (ICRC2003)*, vol.6, p.3367
  "Evolution of Flare Ribbons and Energy Release"

- Ishii, T.T., <u>Asai, A.</u>, Kurokawa, H., Takeuchi, T.T. 2003, *in The 25th meeting of the IAU*, in press
  "Magnetic Neutral Line Rotations in Flare-Productive Regions"

- <u>Asai, A.</u>, Yokoyama, T., Shimojo, M., Shibata, K. 2004, *The Astrophysical Journal*, 605, L77
  "Downflow Motions Associated with Impulsive Nonthermal Emissions Observed in the 2002 July 23 Solar Flare"

- <u>Asai, A.</u>, Yokoyama, T., Shimojo, M., TanDokoro, R., Fujimoto, M., Shibata, K. 2003, *in The SOHO13: Waves, oscillations and small scale transient events in the solar atmosphere*, SP-547, p.163
  "TRACE Downflows and Energy Release"

- Asai, A., Yokoyama, T., Shimojo, M., Masuda, S., Kurokawa, H., Shibata, K. 2004, *The Astrophysical Journal*, 611, in press
  "Flare Ribbon Expansion and Energy Release Rate"

- Asai, A., Yokoyama, T., Shimojo, M., Shibata, K. 2004, *The 5th Solar-B Science Meeting*, in press
  "Downflow as a Reconnection Outflow"

- Day, C. (著), 浅井 歩, 柴田 一成 (訳)
  パリティ(丸善), 2004 年 5 月号, 41 頁
  「レッシ衛星による、太陽フレアのガンマ線撮像」